SANDIA REPORT
SAND2023-05305
Printed June 2023

Sandia National Laboratories

# Expanded Verification and Validation Studies of Hypersonic Aerodynamics with Multiple Physics-Fidelity Models

Jared R. Kirsch, Aaron M. Krueger, Brian A. Freno, Blake W. Lance

Prepared by
Sandia National Laboratories
Albuquerque, New Mexico 87185
Livermore, California 94550

Issued by Sandia National Laboratories, operated for the United States Department of Energy by National Technology & Engineering Solutions of Sandia, LLC.

Available to DOE and DOE contractors from

U.S. Department of Energy
Office of Scientific and Technical Information
P.O. Box 62
Oak Ridge, TN 37831

Telephone: (865) 576-8401
Facsimile: (865) 576-5728
E-Mail: reports@osti.gov
Online ordering: http://www.osti.gov/scitech

Available to the public from

U.S. Department of Commerce
National Technical Information Service
5301 Shawnee Road
Alexandria, VA 22312

Telephone: (800) 553-6847
Facsimile: (703) 605-6900
E-Mail: orders@ntis.gov
Online order: https://classic.ntis.gov/help/order-methods

## ABSTRACT

Hypersonic aerothermodynamics is an important domain of modern multiphysics simulation. The Multi-Fidelity Toolkit is a simulation tool being developed at Sandia National Laboratories to predict aerodynamic properties for compressible flows from a range of physics fidelities and computational speeds. These models include the Reynolds-averaged Navier–Stokes (RANS) equations, the Euler equations with momentum-energy integral technique (MEIT), and modified Newtonian aerodynamics with flat-plate boundary layer (MNA+FPBL) equations, and they can be invoked independently or coupled with hierarchical Kriging to interpolate between high-fidelity simulations using lower-fidelity data. However, as with any new simulation capability, verification and validation are necessary to gather credibility evidence. This work describes formal code- and solution-verification activities, as well as model validation with uncertainty considerations. Code verification activities on the MNA+FPBL model build on previous work by focusing on the viscous portion of the model. Viscous quantities of interest are compared against those from an analytical solution for flat-plate, inclined-plate, and cone geometries. The code verification methodology for the MEIT model is also presented. Test setup and results of code verification tests on the laminar and turbulent models within MEIT are shown. Solution-verification activities include grid-refinement studies on simulations that model the HIFiRE-1 wind tunnel experiments. These experiments are used for validation of all model fidelities. A thorough validation comparison with prediction error and uncertainty is also presented. Three additional HIFiRE-1 experimental runs are simulated in this study, and the solution verification and validation work examines the effects of the associated parameter changes on model performance. Finally, a study is presented that compares the computational costs and fidelities from each of the different models.

# ACKNOWLEDGMENT

The authors wish to thank Greg Weirs, Derek Dinzl, Ross Wagnild, and Jaideep Ray for their insights into the HIFiRE-1 experiments as well as previous simulations performed at Sandia National Laboratories. The authors also wish to thank Matthew Bopp, Brian Carnes, Paul Delgado, and Bryan Morreale for their help in setting up the code-verification cases and insight into the MEIT methodology.

# CONTENTS

# LIST OF FIGURES

# LIST OF TABLES

# 1. INTRODUCTION

The Multi-Fidelity Toolkit (MFTK) is a workflow in the Sandia National Laboratories Sandia Parallel Aerodynamics and Reentry Code (SPARC) code suite, which enables rapid aerothermal modeling for use in hypersonic trajectory generation. To increase the speed of such aerothermal modeling over a traditional approach, MFTK contains three aerothermal model fidelities that can be used together. A Reynolds-Averaged Navier-Stokes solver with multiple turbulence models comprises the highest level of fidelity. An inviscid (Euler equations) solver is coupled to a momentum-energy integral technique (MEIT) solver for the mid-fidelity level. The lowest fidelity level consists of a modified Newtonian aerodynamics (MNA) solver coupled with a boundary layer correlations solver. Simulation results from multiple fidelity levels can be combined to optimally balance the efficiency–accuracy trade-off using hierarchical Kriging to interpolate. Additional details regarding the toolkit may be found in [1] and [2].

MFTK is currently under development, and its capabilities are being expanded in several important ways. To ensure the credibility of aerothermal predictions produced with MFTK, verification and validation activities are necessary for all models in the toolkit and the hierarchical Kriging implementation. Such activities include code verification, which seeks to ensure that a code is an accurate representation of the original mathematical model [3]. They also include solution verification, which seeks to ensure that a given simulation of a mathematical model is sufficiently accurate for the intended use [3]. Additionally, validation, which seeks to ensure that a model is an accurate representation of the real world from the perspective of the intended uses of the model [4, 5], is necessary. These activities strengthen the credibility of the model and potentially identify improvements. Further details on definitions and the viewpoint and goals associated with this project may be found in [1].

To date, significant verification and validation work has been performed on MFTK. Code verification has been performed on the Euler solver [6], and code and solution verification have been performed on the laminar portion of the RANS solver [7]. In a previous study [1], code verification was partially completed on the MNA+FPBL model. This involved verification of inviscid quantities on flat-plate and inclined-plate cases. In addition, solution verification and model validation were performed on all models, referencing one Hypersonic International Flight Research and Experimentation (HIFiRE) experimental run [8] from the HIFiRE-1 experiments. In this study, the scope is expanded to include additional code verification on the MNA+FPBL model, concluding that effort. Code verification activities are documented for a recently updated MEIT model. As part of the code verification effort on the MEIT model, the model theory and implementation are documented in a separate theory guide [9]. Solution verification and model validation are also performed using three additional experimental runs from the HIFiRE-1 experiments. As mentioned in [7], the primary parameters that characterize hypersonic flows are the Mach number, Reynolds number, and freestream enthalpy. Another parameter that may impact model performance is the vehicle's angle of attack. The additional HIFiRE-1 runs enable the model performance to be investigated for various Reynolds numbers and angles of attack. Finally, a study is presented that compares the computational costs and fidelities from the different models to investigate the efficiency–accuracy trade-off for two representative cases.

# 2. CODE VERIFICATION

Code verification is the first credibility activity to be completed for MFTK. This is done to ensure that coding errors are removed before impacting solution-verification or validation activities. The code-verification activities for this report focus on verifying the MNA+FPBL and MEIT models within MFTK. MFTK computes surface quantities for hypersonic flow calculations by combining an inviscid solution with a viscous solution. The MNA model is the inviscid component of the low-fidelity model within MFTK, whereas FPBL is the viscous component of the low-fidelity model within MFTK. MNA code verification was partially completed for a set of simple two-dimensional problems [1]. This work extends the testing to include the viscous QoIs on the same two-dimensional problems, as well as a three-dimensional problem, which stress-tests the streamline distance calculation. For all three problems, three separate viscous models are tested: laminar, White (turbulent), and van Driest (turbulent).

Additionally, MEIT code verification is included in this study. The MEIT method computes surface quantities by reading in an inviscid solution and solving governing equations for momentum and energy thicknesses along streamlines, before calculating values for quantities of interest such as wall heat flux. The first step of the MEIT code verification effort involved analyzing the implementation of the MEIT model in SPARC, and setting up the analytical foundation for a method of manufactured solutions (MMS) code verification test. This involved identifying analytical forms of all equations, correlations, and quantities in the method, and comparing the analytical model to MEIT's predecessor, hypersonic integral boundary-layer analysis of reentry geometries (HIBLARG) code. The MEIT theory guide [9] provides the model derivation, as well as a discussion of the code implementation for the laminar and turbulent flow and ideal gas models. Two MMS tests were developed and deployed on the MEIT code, with one implementing the laminar flow model and the other implementing the turbulent flow model. Both tests used the ideal gas model. These tests targeted the most complex relations in the code given their scope, and showed expected order-of-accuracy trends for all quantities examined. Though these tests did not accomplish complete code verification of the MEIT code, they did cover both laminar and turbulent flow models and provided significant evidence that the models were implemented correctly in the code.

## 2.1. Code Verification for Algebraic Models

Typically, code-verification activities involve verifying the discretization of differential or integral equations that introduces discretization error into the solution. Because of the simplification of the MNA+FPBL equations, initial code-verification test cases do not introduce discretization error because the streamline distance is simplified from the aligned grid. Therefore, the maximum relative difference between an exact solution from a separate code and the computed solution from

MFTK should be approximately round-off error, such that, if the maximum relative difference for the $i^{\text{th}}$ mesh

$$\varepsilon_i = \max_i \left| \frac{\mathrm{QoI}_{i_{\text{Exact}}} - \mathrm{QoI}_{i_{\text{MFTK}}}}{\mathrm{QoI}_{i_{\text{Exact}}}} \right|, \tag{2.1}$$

where QoI is the quantity of interest, is less than $10^{-10}$, the test passes.

### 2.2. Order-of-Accuracy Verification

For the verification problem with discretization error, order-of-accuracy testing is performed. This involves using an exact solution and at least two solutions on different meshes (characterized by the number of elements $n_x$) to compute the exact errors $e_1$ and $e_2$. When the refinement ratio is constant ($r =$ constant), the observed order of accuracy, $p_{\text{obs}}$, is computed as

$$p_{\text{obs}} = \frac{\ln\left(\frac{|e_1|}{|e_2|}\right)}{\ln(r)}. \tag{2.2}$$

When $p_{\text{obs}}$ is within 10% of the theoretical order of accuracy, this test passes.

### 2.3. MNA+FPBL Verification Cases

For this analysis, three code-verification cases are studied to identify implementation (also know as constant errors) and meshing errors. Case 1 is a flat-plate case, Case 2 is an inclined-plate case, and Case 3 is a cone case. The flat-plate case is the most simple of all of the tests due to the regularity of the mesh. The inclined-plate case is almost identical to the flat-plate case, except that the mesh for the inclined-plate case can introduce mesh tolerance errors when inclining the plate. The cone case is introduced to test mesh curvature, which introduces discretization error in the streamline calculation and all downstream QoIs. For the flat-plate and inclined-plate cases, the following FPBL model QoIs are tested for the laminar, White, and van Driest viscous models using the analytical solutions method: coefficient of friction $C_f$, shear stress $\tau$, and wall heat flux $q_w$. For the cone case, the inviscid QoIs with the exception of the streamline distance $L$, pressure coefficient $C_p$, edge pressure $P_e$, edge velocity $\mathbf{V}_e$, edge Mach number $M_e$, edge temperature $T_e$, edge density $\rho_e$, and element normals $\hat{\mathbf{n}}$, are tested using code verification for algebraic models method, whereas the streamline distance and viscous QoIs, $C_f$, $\tau$, and $q_w$, are tested using the order-of-accuracy method.

#### *2.3.1. Case 1: Flat Plate*

The flat-plate case models flow over a flat plate, where the angle of attack is $-7°$. The computational domain of the flat-plate case is a 1-m × 1-m square on the $XZ$-plane, which is shown in Figure 2-1. Since the mesh shown in Figure 2-2 perfectly represents the geometry and is aligned with the streamlines, this case uses an analytical solution to test the correct implementation.

This case provides the most simplistic FPBL model test case to ensure all variables computed by SPARC match the exact solution.

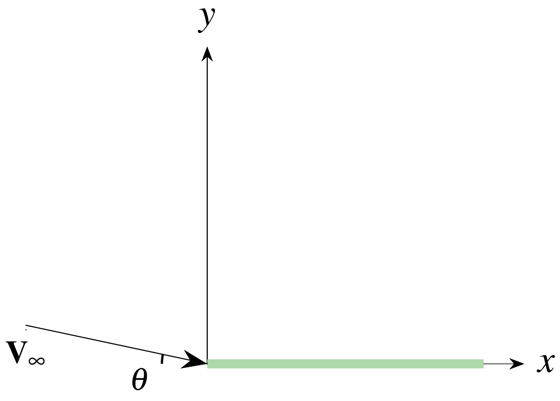

**Figure 2-1.** Computational domain for the flat-plate case (side view).

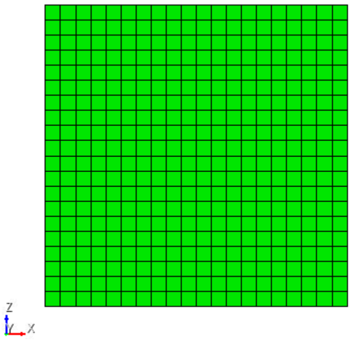

**Figure 2-2.** Coarsest mesh for the flat-plate case (top view).

The exact solution uses input from Table A-1 [1] in conjunction with Equations (A.11) through (A.18) in [1] and the velocity direction specified in Figure 2-1. Using Equation (2.1), the relative error is computed. The results of the code-verification analysis are shown in Table 2-1.

All of the errors in the FPBL variables are below the test criterion of $10^{-10}$, which means the FPBL model equations do not have constant errors when the staggered mesh is aligned, which simplifies the streamline calculation. We note that all van Driest errors are a few magnitudes higher. This is due to the iteration tolerance when solving Eq. A.46 from [1] in SPARC, but the error level is low enough to show that implementation errors are not present. If an implementation error were present, the maximum relative error would be much higher than $10^{-10}$, making this verification test quite sensitive to constant errors. One note in completing this verification testing is that precision tolerances are much more important for these tests than realistic problems. This makes setting up the test cases difficult since hidden or rarely used settings might expose hidden

**Table 2-1.** Code-verification results for the flat-plate case.

| Variable | Fine Mesh Error | Medium Mesh Error | Coarse Mesh Error |
|---|---|---|---|
| $C_{f_{\text{Laminar}}}$ $[\times 10^{-13}]$ | 4.08 | 4.38 | 2.72 |
| $C_{f_{\text{White}}}$ $[\times 10^{-13}]$ | 2.80 | 1.27 | 1.19 |
| $C_{f_{\text{van Driest}}}$ $[\times 10^{-11}]$ | 8.99 | 8.11 | 7.15 |
| $\tau_{x_{\text{Laminar}}}$ $[\times 10^{-13}]$ | 4.29 | 1.49 | 3.77 |
| $\tau_{x_{\text{White}}}$ $[\times 10^{-13}]$ | 2.47 | 2.35 | 2.46 |
| $\tau_{x_{\text{van Driest}}}$ $[\times 10^{-11}]$ | 8.98 | 8.10 | 7.17 |
| $\tau_{y_{\text{Laminar}}}$ | 0.00 | 0.00 | 0.00 |
| $\tau_{y_{\text{White}}}$ | 0.00 | 0.00 | 0.00 |
| $\tau_{y_{\text{van Driest}}}$ | 0.00 | 0.00 | 0.00 |
| $\tau_{z_{\text{Laminar}}}$ | 0.00 | 0.00 | 0.00 |
| $\tau_{z_{\text{White}}}$ | 0.00 | 0.00 | 0.00 |
| $\tau_{z_{\text{van Driest}}}$ | 0.00 | 0.00 | 0.00 |
| $q_{w_{\text{Laminar}}}$ $[\times 10^{-13}]$ | 4.55 | 3.55 | 2.99 |
| $q_{w_{\text{White}}}$ $[\times 10^{-13}]$ | 1.59 | 1.66 | 1.38 |
| $q_{w_{\text{van Driest}}}$ $[\times 10^{-11}]$ | 8.98 | 8.10 | 7.16 |

coding errors. An increased error is expected since round-off error generally increases with the number of calculations being performed.

### 2.3.2. Case 2: Inclined Plate

The inclined-plate case is identical to the flat-plate case, but the implementation is slightly different. For this case, the velocity is along the $x$-axis and the plate is inclined by 7°, as shown in Figure 2-3. Since the mesh perfectly represents the geometry and the mesh is aligned with the streamlines, this case uses an analytical solution to test the correct implementation. This case provides the second most simplistic FPBL model test case to ensure all variables computed by SPARC match the exact solution.

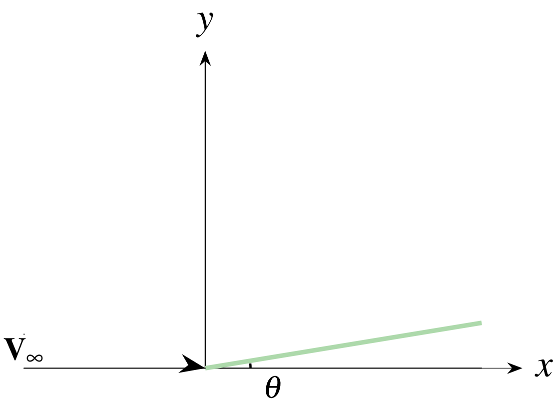

**Figure 2-3.** Computational domain for the inclined-plate case.

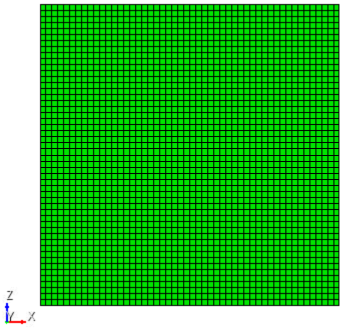

**Figure 2-4.** Coarsest Mesh for the inclined-plate case.

The exact solution uses input from Table A-1 [1] in conjunction with Equations (A.11) through (A.18) in [1] and the velocity direction specified in Figure 2-3. Using Equation (2.1), the relative error is computed. The results of the code-verification analysis are shown in Table 2-2.

All of the errors in the FPBL variables are below the test criterion of $10^{-10}$, except for $\tau_{z_{\text{van Driest}}}$, which has a maximum relative error of $6.21 \times 10^{-8}$. Even with the larger relative error, this is significantly lower than expected ordered or constant errors, which means the FPBL model equations do not have constant errors when the staggered mesh is aligned, which simplifies the streamline calculation. This component of the shear stress in particular is near zero and has absolute error on the order of $10^{-23}$, so its impact on the solution is negligible. However, it was included in the analysis for completeness. One note on this particular problem is that initial results were impacted by the precision of the mesh. This problem requires the maximum precision available from the meshing software to ensure mesh precision does not impact the exact verification results. When applications need more than three or four digits of accuracy, additional studies should be performed to ensure the errors in the van Driest model are not impacting the solution.

**Table 2-2.** Code verification results for the inclined-plate case

| Variable | Fine Mesh Error | Medium Mesh Error | Coarse Mesh Error |
|---|---|---|---|
| $C_{f_{\text{Laminar}}}$ $[\times 10^{-13}]$ | 4.39 | 4.21 | 4.65 |
| $C_{f_{\text{White}}}$ $[\times 10^{-13}]$ | 2.60 | 2.78 | 1.13 |
| $C_{f_{\text{van Driest}}}$ $[\times 10^{-11}]$ | 8.93 | 8.90 | 8.63 |
| $\tau_{x_{\text{Laminar}}}$ $[\times 10^{-13}]$ | 4.30 | 4.67 | 3.65 |
| $\tau_{x_{\text{White}}}$ $[\times 10^{-13}]$ | 2.67 | 2.63 | 2.44 |
| $\tau_{x_{\text{van Driest}}}$ $[\times 10^{-11}]$ | 8.96 | 8.88 | 8.61 |
| $\tau_{y_{\text{Laminar}}}$ $[\times 10^{-13}]$ | 4.46 | 4.66 | 2.88 |
| $\tau_{y_{\text{White}}}$ $[\times 10^{-13}]$ | 2.27 | 2.11 | 2.07 |
| $\tau_{y_{\text{van Driest}}}$ $[\times 10^{-11}]$ | 8.96 | 8.91 | 8.60 |
| $\tau_{z_{\text{Laminar}}}$ $[\times 10^{-11}]$ | 1.63 | 2.95 | 8.13 |
| $\tau_{z_{\text{White}}}$ $[\times 10^{-11}]$ | 12.75 | 3.41 | 4.29 |
| $\tau_{z_{\text{van Driest}}}$ $[\times 10^{-8}]$ | 1.75 | 6.21 | 3.83 |
| $q_{w_{\text{Laminar}}}$ $[\times 10^{-13}]$ | 4.69 | 4.11 | 4.66 |
| $q_{w_{\text{White}}}$ $[\times 10^{-13}]$ | 1.96 | 1.72 | 1.66 |
| $q_{w_{\text{van Driest}}}$ $[\times 10^{-11}]$ | 8.94 | 8.88 | 8.64 |

### 2.3.3. *Case 3: Nose-Cone*

Now that code verification testing has been completed on simple geometries, additional testing is completed on realistic, curved geometries. For the nose-cone problem, the geometry description is shown in Figure 2-5 with the coarsely meshed geometry shown in Figure 2-6.

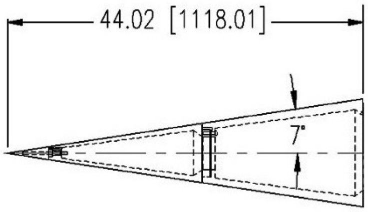

**Figure 2-5.** This geometry is based on the forecone of the HIFiRE-1 wind tunnel test geometry from [10]. The text states that the final nosetip was changed from sharp to a radius of 2.5 mm.

Since this test introduces discretization error in the streamline distance calculation, all upstream (inviscid) QoIs are tested using the algebraic model code verification method, whereas all downstream QoIs ($C_f$, $\tau$, $q_w$) are tested using the order-of-accuracy code verification method. The exact solution used by both code verification methods uses input from Table 2-3 in conjunction with Equations (A.11) through (A.18) in [1]. Note that while the velocity is significantly larger than typical SPARC problems, it is set this large to avoid a singularity in the White model. Further discussion on this is presented at the end of Section 2.3.3.2.

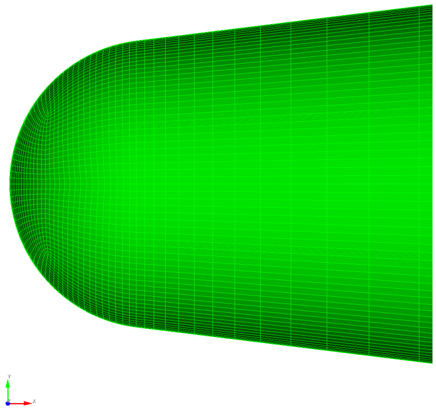

**Figure 2-6.** Coarse mesh for the MNA+FPBL nose-cone problem.

**Table 2-3.** Table of values used in code-verification analysis.

| Constant Name | Notation | Value | Units |
|---|---|---|---|
| Gas constant for air | $R$ | 287.05 | J/kg/K |
| Ratio of specific heats | $\gamma$ | 1.4 | – |
| Prandtl number | Pr | 0.73684 | – |
| Freestream density | $\rho_\infty$ | 0.066958 | kg/m$^3$ |
| Freestream velocity | $\mathbf{V}_\infty$ | [217000, 0, 0] | m/s |
| Freestream temperature | $T_\infty$ | 226.46 | K |
| Wall temperature | $T_w$ | 300 | K |
| Sutherland constant | $C_{\text{visc}}$ | $1.458 \times 10^{-6}$ | – |
| Sutherland constant | $S_{\text{visc}}$ | 110.3 | – |

#### 2.3.3.1. Algebraic Model Results

Using Equation (2.1), the relative error is computed for all inviscid QoIs. The results of the code-verification analysis are shown in Table 2-4.

**Table 2-4.** Code-verification inviscid results for the cone case.

| Variable | Fine Mesh Error | Medium Mesh Error | Coarse Mesh Error |
|---|---|---|---|
| $n_x$ $[\times 10^{-13}]$ | 4.11 | 4.11 | 4.11 |
| $n_y$ $[\times 10^{-13}]$ | 4.89 | 4.96 | 4.49 |
| $n_z$ $[\times 10^{-13}]$ | 4.84 | 4.96 | 4.53 |
| $C_p$ $[\times 10^{-13}]$ | 4.94 | 4.82 | 4.67 |
| $P$ $[\times 10^{-13}]$ | 4.85 | 4.77 | 4.55 |
| $u$ $[\times 10^{-13}]$ | 60.52 | 16.76 | 4.65 |
| $v$ $[\times 10^{-13}]$ | 60.87 | 13.41 | 4.83 |
| $w$ $[\times 10^{-13}]$ | 60.93 | 18.73 | 4.83 |
| $M$ $[\times 10^{-13}]$ | 60.90 | 14.98 | 4.75 |
| $T$ $[\times 10^{-13}]$ | 4.75 | 4.89 | 4.77 |
| $\rho$ $[\times 10^{-13}]$ | 4.92 | 4.88 | 4.73 |

All of the relative errors in the MNA variables are below the test criterion of $10^{-10}$, which means the FPBL model equations do not have constant errors, even when the mesh is not aligned. If an implementation error were present, the relative error would be much higher than $10^{-10}$, making this verification test quite sensitive to constant errors. One note in completing this verification testing is that precision tolerances are much more important for these tests than realistic problems. This makes setting up the test cases difficult since hidden or rarely used settings can cause issues to the results. An increased error is expected since round-off error generally increases with the number of calculations being performed.

#### 2.3.3.2. Order-of-Accuracy Results

This test introduces discretization error in the streamline distance calculation. To ensure the streamline distance calculation is implemented correctly, a mesh refinement study is completed to measure the observed order of accuracy. When the observed order of accuracy matches the theoretical order of accuracy to within 10%, the test passes. Additionally, since $C_f$, $\tau$, and $q_w$ are functions of the streamline distance, the observed order of accuracy for these QoIs are also measured. The theoretical order of accuracy is based on approximating the curvature of the geometry with a linear element. The linear element introduces a second-order error, which means the theoretical order of accuracy for MNA+FPBL when the geometry has curvature is two ($\mathscr{O}(h^2)$). The exact solution uses input from Table 2-3 in conjunction with Equations (A.11) through (A.18) in [1]. Using Equation (2.1), the observed order of accuracy for all FPBL variables are computed using the relative error for two sets of meshes. These error values are substituted into Equation (2.2) to compute the observed order of accuracy. The results of the code-verification analysis are shown in Figures 2-7 through 2-9.

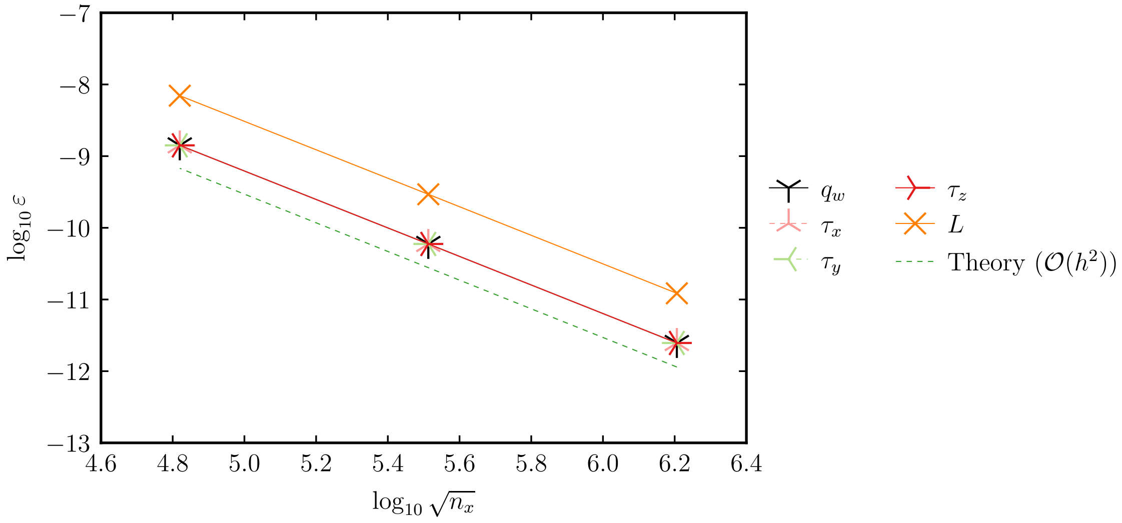

**Figure 2-7.** Code verification results for the viscous QoIs in the laminar model.

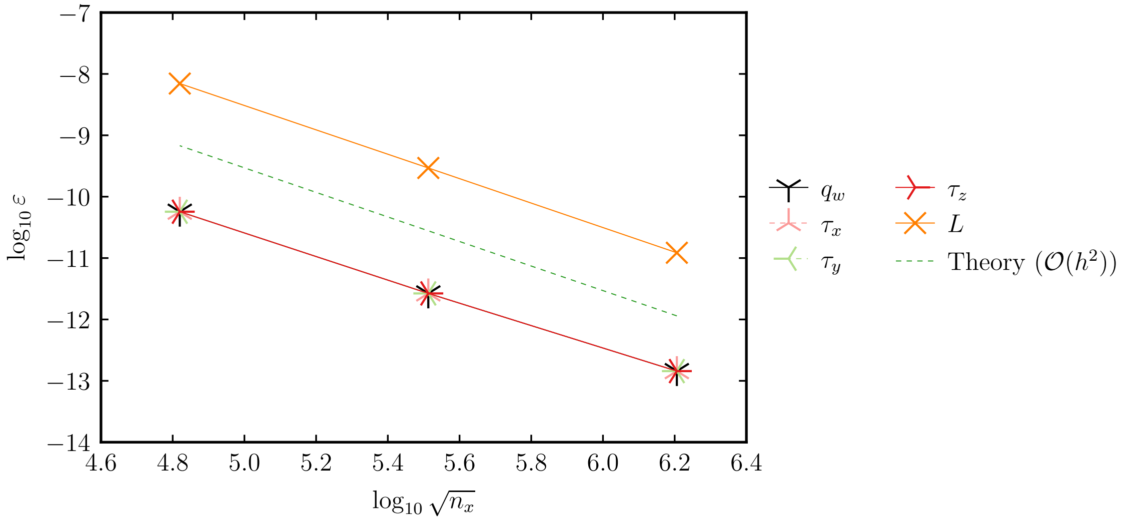

**Figure 2-8.** Code verification results for the viscous QoIs in the White model.

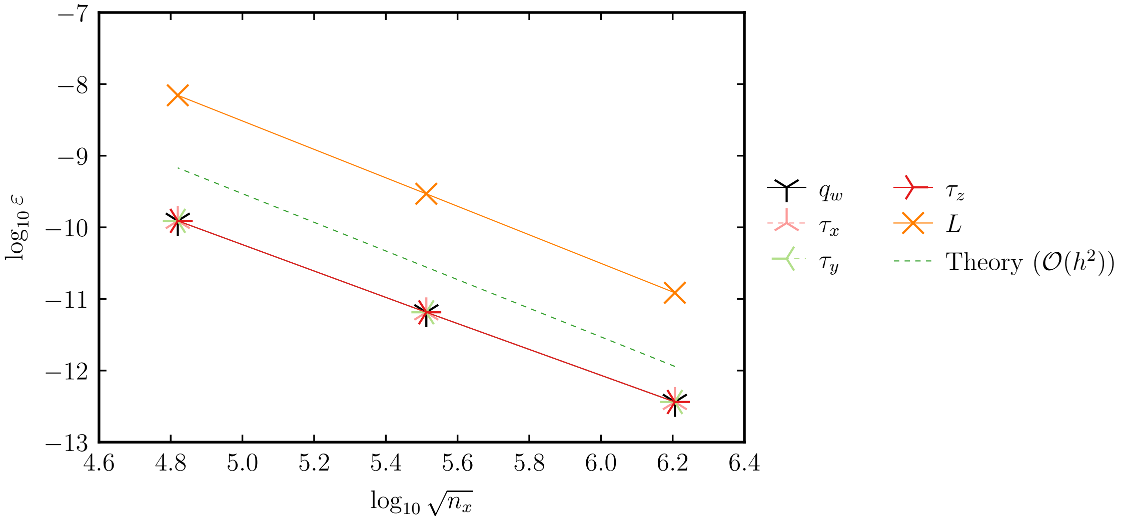

**Figure 2-9.** Code verification results for the viscous QoIs in the van Driest model.

The observed order of accuracy for all FPBL variables and the streamline distance are within 10% of the theoretical order of accuracy, which suggests the implementation of the FPBL model and streamline distance equations is correct. If a significant implementation error were present, the difference between the observed order of accuracy and the theoretical order of accuracy would be larger than 10%. One note in completing this verification testing is that a singularity in the White model causes degradation in the observed order of accuracy when it was applied to the whole domain. As the mesh is refined, the Reynolds number becomes small and the natural log of the Reynolds number is increased towards negative infinity. To avoid this, the freestream velocity is increased to ensure the Reynolds number is larger than Euler's number at every element centroid to avoid issues with the natural log. Whereas the observed order of accuracy degrades slightly with refinement, it is still within 10% of the theoretical order of accuracy. Since a realistic problem would not apply the White model in areas where the flow is laminar (i.e., small Reynolds number), this singularity will not be present in realistic problems.

### 2.3.4. Coding Errors Identified

While completing code verification testing, two coding errors were identified, which impacted all FPBL models. The first coding error was identified in the non-dimensional viscosity calculation. The calculation incorrectly used the wall temperature, $T_w$, instead of the non-dimensional temperature, $T^*$. The second coding error was identified in the $S$ and $b$ constants in coefficient of friction calculation. The $S$ calculation incorrectly used the wall temperature, $T_w$, instead of the edge temperature, $T_e$, whereas the $b$ calculation left out subtracting the equation by 1.0. To show the impact of these coding errors, the relative error for each QoI is shown for the flat plate (Figure 2-10) and inclined plate (Figure 2-11) cases.

These differences are significant and would have impacted future simulations if the coding errors were not caught. To show the impact on a real problem, Figure 2-12 is an example of how the

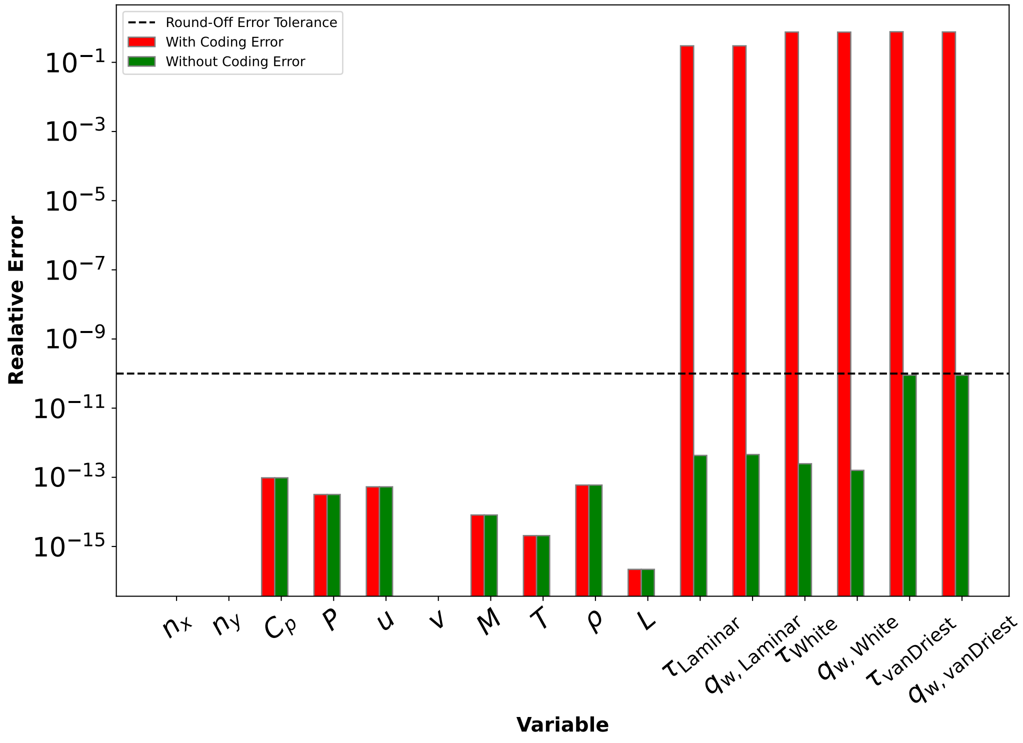

**Figure 2-10.** Coding error identified in the FPBL model on the flat plate case.

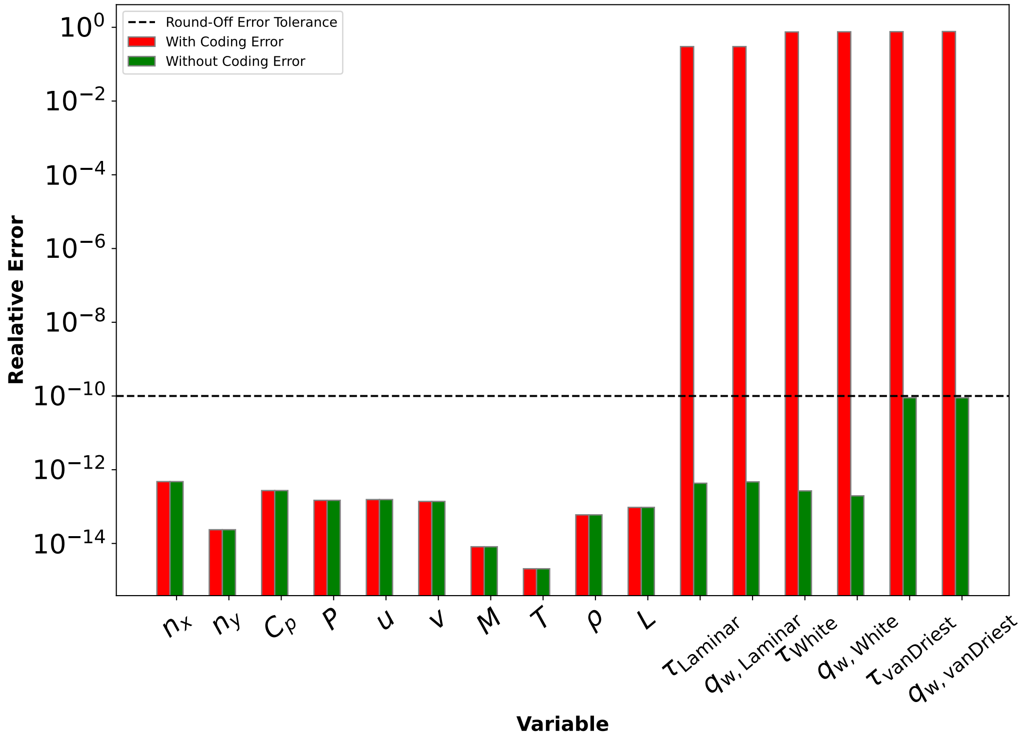

**Figure 2-11.** Coding error identified in the FPBL model on the inclined plate case.

coding errors would have impacted the White model validation assessment for the HIFiRE-1 test series (see Section 3 for more details about the test series).

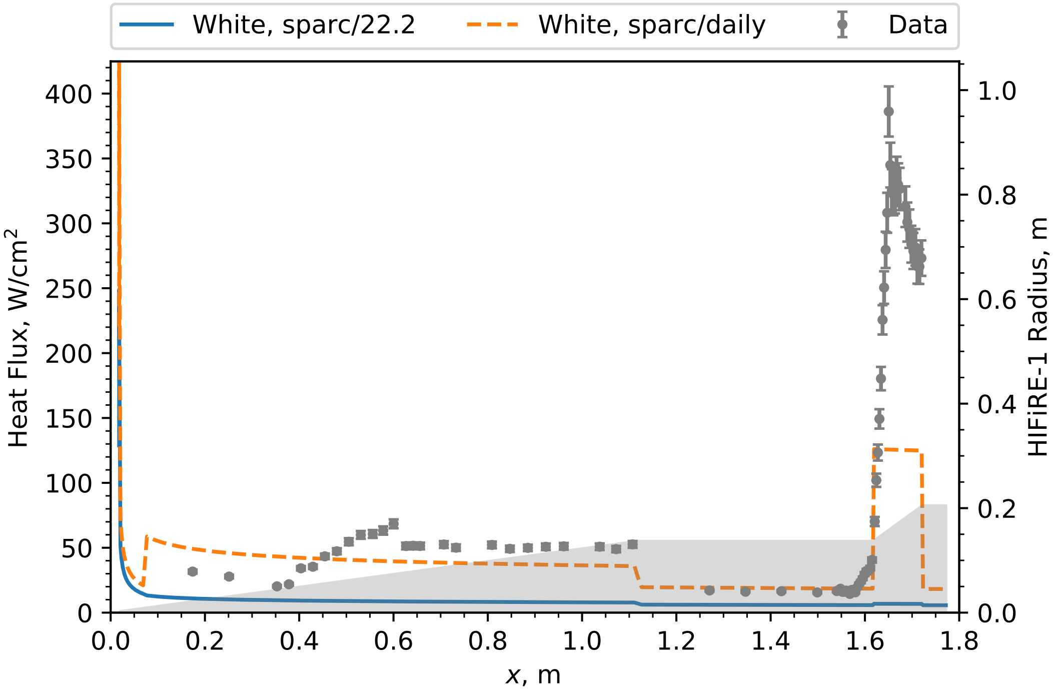

**Figure 2-12.** Impact of coding error on a cone case validation problem.

The error-free version of the model (`sparc/daily`) matches significantly better to the experimental data than the version of the model with coding errors (`sparc/22.2`). This shows how important code verification is when doing a validation assessment because the model performance can be significantly degraded by coding errors.

## 2.4. MEIT

This section outlines the completed code verification on the MEIT model using MMS (see [11] for more information on this method). The code verification performed on the MEIT model includes both a laminar and turbulent unit test. The process of building and running these tests uncovered several real and potential issues with the code. Before this occurred, the code had to be understood in sufficient depth for rigorous code verification to succeed. Thus, a literature survey was done and the present implementation of the MEIT model was studied. Derivations of the governing equations and streamline metric from Paul Delgado and Lawrence DeChant were also pulled together, and all of the resulting material was used to create new documentation for the model. This documentation [9] contains a detailed discussion of the code's theory and implementation for the model space examined in this test.

### *2.4.1. General Test Description*

The MEIT model has reduced complexity in comparison with models which incorporate the Navier–Stokes equations to obtain full solutions of viscous flow fields. However, the MEIT model is moderately complex. It contains integro-differential equations, a gas model, several correlations for model closure and parameter description, and multiple flow regimes with separate models (laminar and turbulent). The MEIT solution process involves reading in an inviscid flowfield solution from a volume mesh and interpolating quantities onto a surface mesh. Then, streamlines are calculated on the surface of the vehicle and the MEIT algorithm runs the solution procedure along each of the streamlines. The resulting quantities computed on the streamlines are then interpolated back onto a surface mesh and the end product is a scalar or vector field of values for each output quantity on the vehicle surface. When performing code verification, the primary focus is on ensuring that the mathematical model is correctly implemented in the code. This focus is balanced by the fact that code verification should be broad in scope in order to cover all parts of the solution process which may produce errors. In the present study, the scope is limited to solution along a single streamline, thus focusing on the mathematical implementation of the model for the streamline calculation. The scope of the code verification effort in the present study is further narrowed to a specific subset of options in the MEIT model. Specifically, the ideal gas model was analyzed, since the real gas model involved a table lookup in the calculation of thermodynamic quantities. Tables are difficult to implement in an MMS test, since an analytical description of them is not necessarily attainable. Additionally, influence coefficients use different formulas depending on the value of the Levy–Lees parameter $\beta$. In the present study, the tests are designed to exercise the more complex relations (a function of $\beta$ raised to a power and multiplied by a constant versus simply a constant). The applicable equations and correlations, as well as the solution procedure, are given in [9]. The following sections give the values which determined the set of expressions used for each test.

The geometry chosen for this test is a 2D representation of a sharp half cone and is shown in Figure 2-13. This geometry is selected specifically to allow for analytical evaluation of the source terms arising from the model in the code verification process. Geometry defined with trigonometric or higher-order polynomial functions was not used because it resulted in integrals which could not be evaluated in the manufactured solution, or discontinuities in quantities.

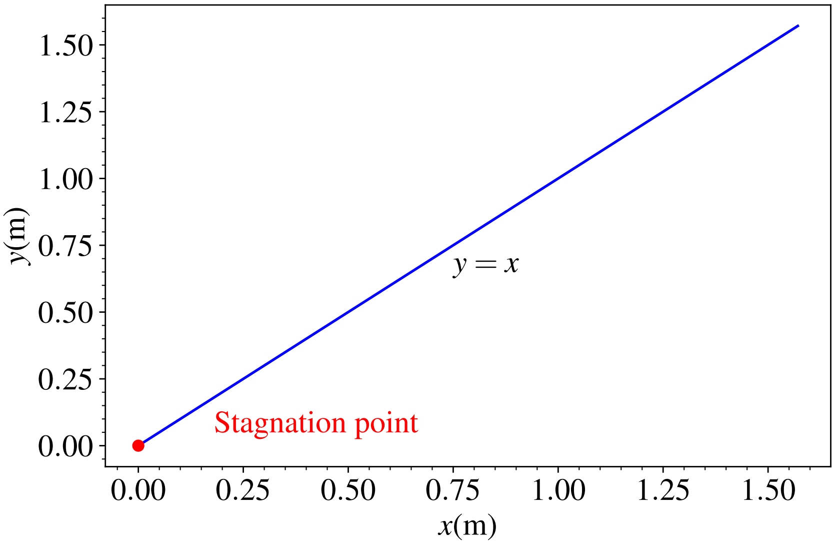

**Figure 2-13.** Geometry of MEIT code verification test.

The primary equations solved along streamlines in the MEIT model are differential equations for momentum and energy thickness, given in Equations (2.3) and (2.4), respectively [12]. In these equations, $h_\beta$ is the streamline metric, $\rho_e$ is the edge density, $U_e$ is the ege velocity, $p$ is pressure, $C_f$ is the skin friction coefficient, $C_h$ is the Stanton number, $h_{stag}$ is the stagnation enthalpy, $h_w$ is the wall enthalpy, $h_{rl}$ is the recovery enthalpy, and $s$ is the streamline distance. The MMS approach involves manufacturing solutions to the dependent variables of the governing equations. Here, this means manufacturing solutions for momentum thickness ($\theta$) and energy thickness ($\phi$), which are shown in Equations (2.5) and (2.6) [12]. In this test, these equations are solved along a single streamline, and the equations specify the value of the two thicknesses along its length. In these equations, $\nu_1$ is the kinematic viscosity at the stagnation point, $H$ is the boundary layer shape factor, Pr is the Prandtl number, and $(dU_e/ds)_1$ is the edge velocity gradient at the stagnation point. The manufactured solutions used in the present study are equivalent to the limiting form for $\theta$ and $\phi$ at the stagnation point, and thus match the code output there. In addition, with sufficient refinement along the streamline ($s \rightarrow 0$), the code output matches the manufactured solutions at the next 4 points on each streamline.

$$\frac{d\left(\theta h_\beta \rho_e {U_e}^2\right)}{ds} = h_\beta \rho_e {U_e}^2 \left(\theta \frac{H}{\rho_e {U_e}^2}\frac{dp}{ds} + \frac{C_f}{2}\right) \tag{2.3}$$

$$\frac{d\left(\phi h_\beta \rho_e U_e \left(h_{\mathrm{stag}} - h_w\right)\right)}{ds} = C_h \frac{h_{\mathrm{stag}} - h_w}{h_{\mathrm{rl}} - h_w} h_\beta \rho_e U_e \left(h_{\mathrm{stag}} - h_w\right) \tag{2.4}$$

$$\theta_1 = \sqrt{\frac{0.245\nu_1}{(3+H)\left(\frac{dU_e}{ds}\right)_1}} \tag{2.5}$$

$$\phi_1 = \sqrt{\frac{0.220\nu_1}{2\mathrm{Pr}^{4/3}\left(\frac{dU_e}{ds}\right)_1}} \tag{2.6}$$

Additionally, the inviscid pressure, temperature, and velocity along the streamline are specified in simple functional form, as Equations (2.7)–(2.9). These forms are not ideal in comparison with sinusoidal functions for two primary reasons. First, they lack the continuity under differentiation that sinusoidal functions exhibit. Second, they do not provide the opportunity to test the behavior of the model with fluctuations in quantities along the streamline length. However, they are realistic in the sense that pressure decreases from the stagnation point whereas velocity increases. Temperature was chosen to be constant due to the Levy–Lees parameter $\xi$, which involves an integral, and cannot be evaluated as an analytical expression in Wolfram Mathematica for more complex forms. In the current implementation of MEIT, the edge quantities are taken as equal to the inviscid quantities, so that in this test, Equations (2.7)–(2.9) specify functional forms for edge quantities along the streamline.

$$p = p_{\text{ref}}\left(2 - s\right) \tag{2.7}$$

$$T = T_{\text{ref}} \tag{2.8}$$

$$U = U_{\text{ref}}\left(1 + s\right) \tag{2.9}$$

A full analytical model was built in Mathematica with the MEIT equations, manufactured forms, and specified quantities. In MMS, the solutions to the governing equations are specified, and the governing equations are then applied to the specified solutions to obtain source terms. With these source terms added to the governing equations, the new governing equations are theoretically satisfied by the manufactured solutions. The code is then tested to see whether the MEIT and manufactured values of the quantities solved for in the governing equations are consistent. The Mathematica scripts are used to generate these source terms, which are added to the governing equations in the MEIT solve. In reality, the process of creating the source terms was iterative, with the functional form of prescribed and manufactured quantities being updated until the source terms were analytical functions which could be evaluated in the test code. With the test set up as described above, it is run and code values were compared to analytical values. The entire process is summarized in Figure 2-14.

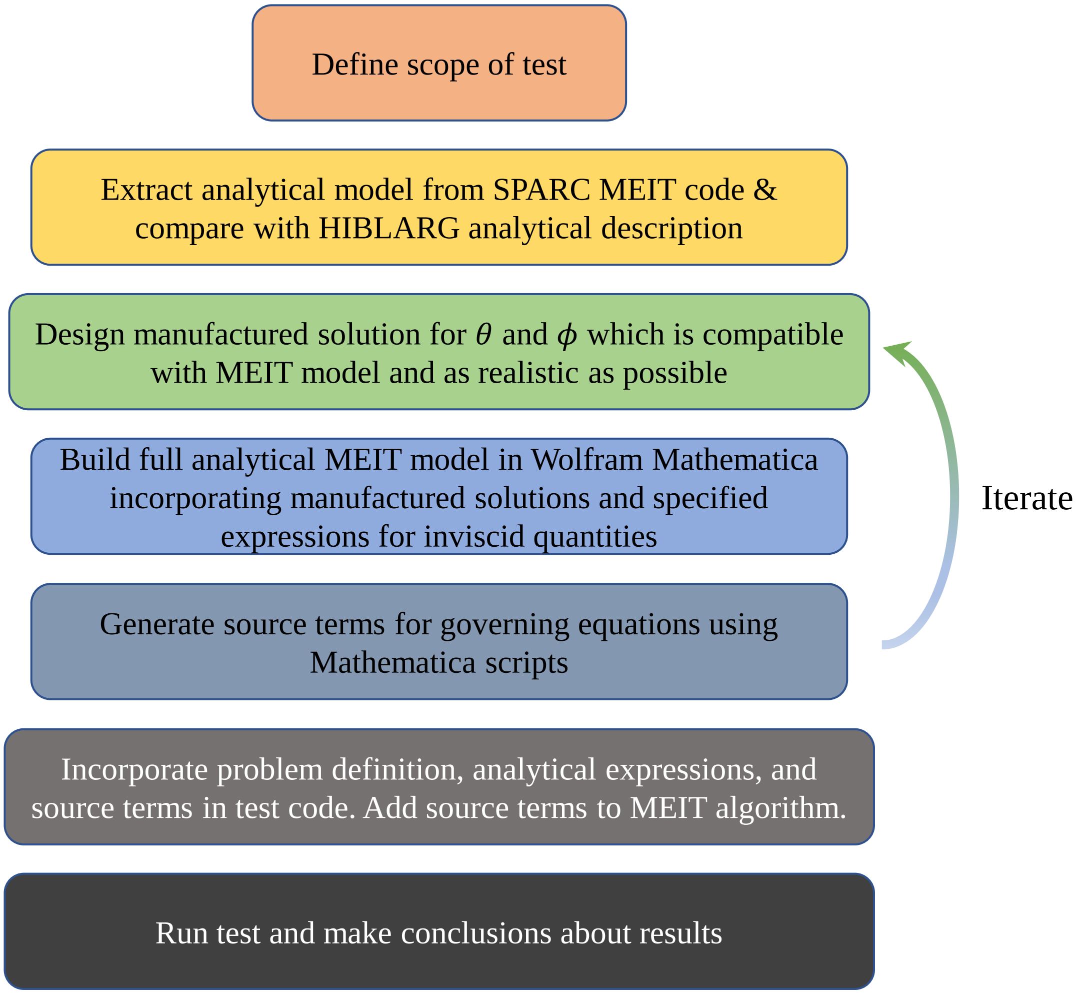

**Figure 2-14.** Flowchart for MEIT code verification test process.

### 2.4.2. Laminar Test

The first test used on the MEIT code is a test of the model using the simpler laminar relations (see [9]). The model is set to use laminar relations along the entire streamline, and the modified governing equations use source terms based purely on these laminar relations. Expressions used for the Stanton number and skin friction coefficient correspond to a $\beta$-value larger than zero (see Equations 3.61, 3.62, 3.67 in [9]). The process followed for evaluating errors in quantities in the code is to start with the first quantities set or computed and move to the quantities which are further downstream in the solution process, ultimately analyzing the QoIs such as wall heat flux. First, constant and thermodynamic quantities are analyzed with a series of checks expecting equivalence or agreement within a small tolerance. Thermodynamic quantities are expected to have a relative difference with magnitude less than $10^{-12}$ (the difference is scaled by the code value). The results are shown in Tables 2-5 and 2-6. For the quantities in Table 2-5, exact or close agreement is obtained, and absolute error is used. For the quantities in Table 2-6, the magnitude of the quantities varies significantly, with some having several digits before the decimal place and some having none. Thus, relative error is used to normalize the error for these quantities such that they can be held to the same relative standard. This measure provides an indication of how many digits are in agreement rather than how many digits after the decimal place are in agreement. With a target error threshold of $10^{-12}$, all quantities in both tables pass the error check. The process used to compute the thermodynamic quantities in the Table 2-6 is modified as part of the code verification effort to make the calculations purely SI except for the calculation of $\mu$, which has a standard form assuming english units for temperature. This change removes the dependency of these quantities on the precision of conversion factors, and reduces the complexity of the analytical expressions in the test. This can be noted as a code improvement for thermodynamic property calculations. With these checks passed, the discretization-dependent quantities are then analyzed using order-of-accuracy testing over several levels of refinement.

**Table 2-5.** Absolute errors in quantities tested first.

| Variable | Absolute Error |
|---|---|
| Transition | 0 |
| Roughness | 0 |
| Blowing | 0 |
| $p_e$ | 0 |
| $T_e$ | 0 |
| $\rho_e$ | 0 |
| $u_e$ | 0 |
| $h_\beta$ | 0 |
| $T_w$ | 0 |
| $M_e$ $[\times 10^{-15}]$ | 0.89 |
| Recovery factor $[\times 10^{-15}]$ | 0 |
| $\xi$ $[\times 10^{-15}]$ | 0.15 |

For the order-of-accuracy testing, the streamline is discretized using 6 refinement levels with each having a factor of 10 more points than the previous level. At each level, 1 is added to the number

**Table 2-6.** Relative errors in thermodynamic quantities.

| Variable | Relative Error |
|---|---|
| $s_e$ $[\times 10^{-15}]$ | 1.11 |
| $h_e$ $[\times 10^{-15}]$ | 1.55 |
| $\mu_e$ $[\times 10^{-15}]$ | 1.33 |
| $s_w$ $[\times 10^{-15}]$ | 1.11 |
| $h_w$ $[\times 10^{-15}]$ | 0 |
| $\mu_w$ $[\times 10^{-15}]$ | 0.22 |
| $\rho_w$ $[\times 10^{-15}]$ | 0 |
| $h_r$ $[\times 10^{-15}]$ | 0.22 |

of points such that there is an even number of segments along the streamline. Thus, the coarsest level has 11 points and the finest has 1,000,001 points. Relative error is used for all quantities except $\xi$ and $\beta$, which have significantly amplified relative errors near the stagnation point due to their small value when $s \approxeq 0$. For these two quantities, absolute error is used. The resulting plots are shown in Figures 2-15–2-16b. The theoretical order of accuracy for $\xi$ is 2 due to the trapezoidal rule used in its calculation. Figure 2-15 thus shows that the numerical integration method used for calculation of $\xi$ operated with the correct order. First-order differentiation is used in the calculation of $\beta$ and thus the theoretical order of accuracy is 1 for $\beta$ and all subsequent quantities. The convergence trend for $\beta$ is shown in Figure 2-15, and exhibits good agreement with the theoretical order. Figure 2-16 shows that the other quantities follow the expected order of accuracy closely for most of the study's domain. Agreement is within 15% along the entire trend for all quantities except for $\theta$ and $\mathrm{Re}_\theta$, which shows ∼27% difference from the expected order of accuracy between the 3rd and 4th points. However, agreement is much better in the other intervals, reaching less than 5% difference by the last interval. Overall then, agreement with the expected orders of accuracy is sufficient for all quantities to strongly suggest the absence of code bugs. The overall theoretical order of accuracy of the code is 1, and the test showed strong evidence that convergence in QoIs and intermediate quantities agree with this fact, for the scope of the test. It is worth noting that if the scope of the test weas expanded to include stagnation point detection, this operation would also limit the theoretical order of accuracy of the code to 1. Any further tests should take scope into careful consideration when determining the theoretical order of accuracy.

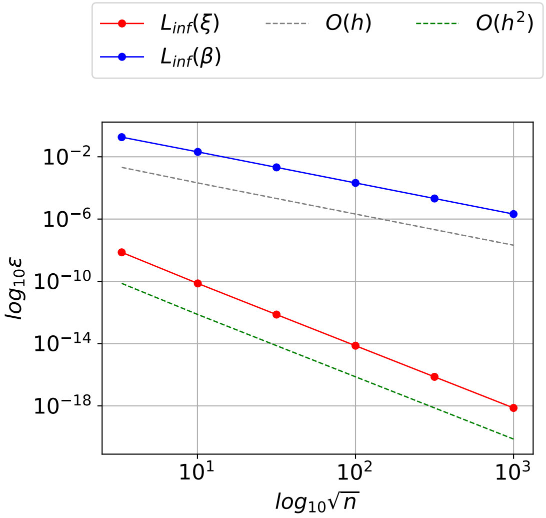

**Figure 2-15.** Order of accuracy for $\xi$ and $\beta$ from laminar test.

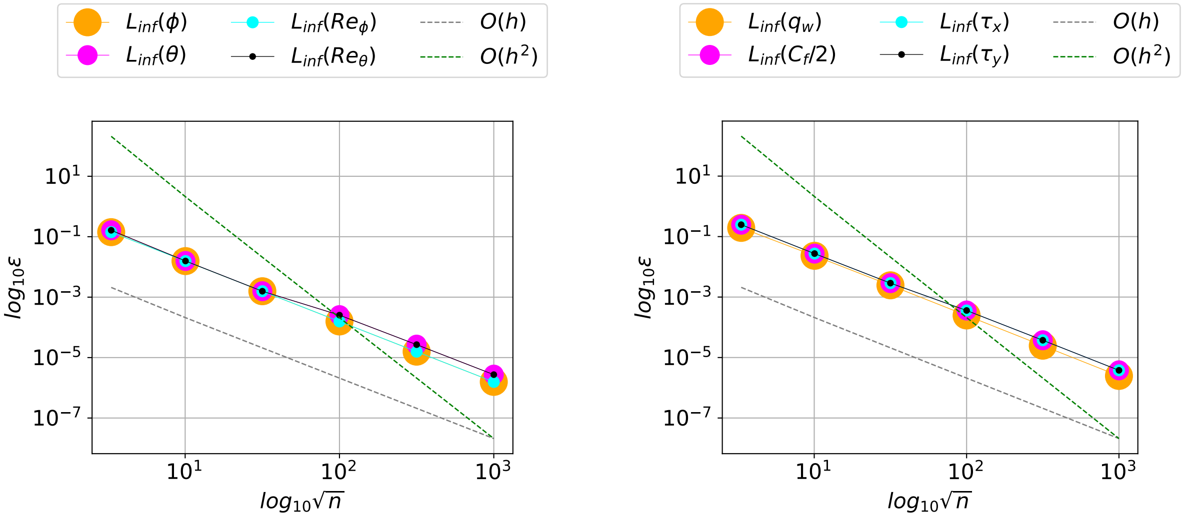

**(a)** Thicknesses and Re from laminar test.

**(b)** Additional quantities from laminar test.

**Figure 2-16.** Order of accuracy plots for test QoIs from laminar test.

### 2.4.3. *Turbulent Test*

The turbulent test exercises the Abres Shape Change Code 1980 (ASCC 80) turbulent correlations on the same geometry with the same manufactured solutions and specified inviscid quantities as in laminar test. A second set of Mathematica scripts incorporating the ASCC 80 correlations is used to generated new source terms, and the test is updated to include an option to run with the turbulent formulation. This test is run on the same six refinement levels as in the laminar test. More complex expressions are once again targeted by choosing $\beta = 0$. In addition, the Prandtl number is 0.7 (greater than 0.6) and the Mach number is greater than 1.5. The last two conditions generally target the more complex set of relations in the ASCC 80 turbulent correlations (Equations 3.81–3.100 in [9]). The resulting errors on the constant and thermodynamic quantities all pass the $1 \times 10^{-12}$ criterion as in Tables 2-5 and 2-6. The order of accuracy plots are shown in Figures 2-17–2-18b. Again, $\theta$ and $Re_\theta$ show $\sim$27% difference from the expected order of accuracy between the 3rd and 4th points but much lower percent difference by the finest interval. All other quantities show agreement in order of accuracy to within 15% over the entire trend, with agreement in the finest intervals being significantly better than the maximum discrepancy. It should be noted that this is only achieved after modifying the formula for the Stanton number to remove a factor of $\mathrm{Pr}^{1/2}$ that was included in the HIBLARG manual. The overall first-order nature of the code was clearly seen and test results clearly matched the theoretical order of accuracy. Thus, the test conditionally passed and the code is considered verified within the scope of the test.

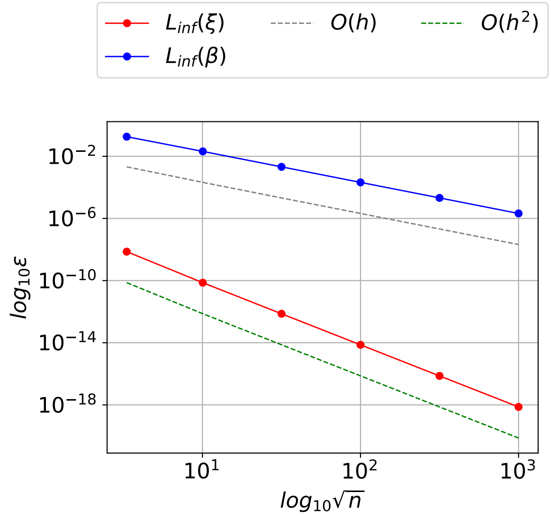

**Figure 2-17.** Order of accuracy for $\xi$ and $\beta$ from turbulent test.

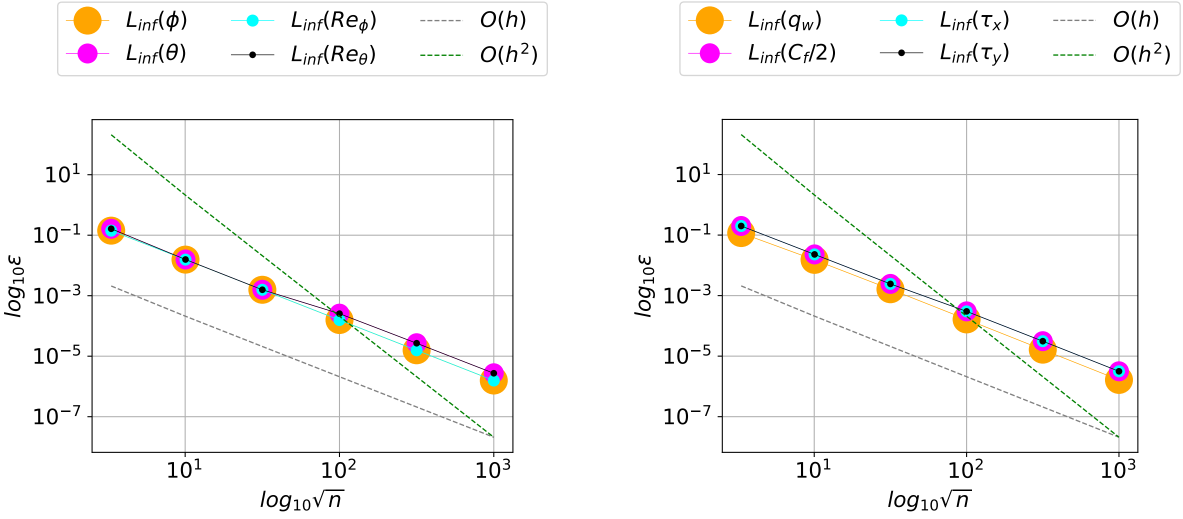

**(a)** Thicknesses and Re.

**(b)** Additional quantities.

**Figure 2-18.** Order of accuracy plots for test QoIs from turbulent test.

## 2.5. Future Work

Significant progress has been made in verifying the MNA+FPBL and MEIT models. The MNA+FPBL model has undergone significant testing with increasing complexity, with the cone case exercising all parts of the MNA+FPBL code. The MEIT model has had both the laminar and turbulent models tested, but with a subset of conditions limiting the scope of the tests.

The MEIT model has thus been partially verified by the testing described above. The extent of testing completed to date is related to the heavy investment that has been made with regards to understanding and describing the moderately complex MEIT model, and setting up high-quality initial tests. Several coding errors have been found and could be further explored given sufficient motivation. One error that was fixed in this effort was an incorrect `if` condition in the calculation of viscosity. Another problem which was fixed was the thermodynamic module taking in quantities in SI units, converting to English units, computing thermodynamic quantities, and then converting back to SI units. This code was updated to include only SI units to streamline the process and remove the potential for unit conversion coding errors which could reduce solution accuracy or produce incorrect results. Related efforts fixed a coding error related to interpolation from the streamlines back to the surface mesh. Another of these errors was an influence coefficient formulation which was incorrect at the stagnation point.

Several potential issues were also identified for possible improvement. One of these issues is the significant deviation of the order of accuracy trend in $\theta$ and $Re_\theta$ from the expected value of 1 at intermediate refinement levels. Another is the fact that the algorithm defines the stagnation region as the four points following the stagnation point regardless of spatial refinement along the streamline. This means that the stagnation region essentially collapses to zero with high refinement. An improvement would be to define the stagnation region based on a physical length scale. Another potential issue found was in the finite difference expression for the velocity gradient at the stagnation point, where the velocity was assumed to be exactly zero. This assumption may not be consistent with the actual velocity computed in a simulation and should be examined in more detail or the formula replaced with a standard finite difference. A potentially significant improvement—but one which should be weighed against the increased cost associated with it—would be to change the MEIT discretization to 2nd order. The turbulent test also uncovered some potential issues, with one being a missing factor of $\mathrm{Pr}^{1/2}$ in the Stanton number formula as compared with the formula in the HIBLARG manual [12]. This formula is part of the ASCC 80 set of correlations. References containing these correlations are difficult to acquire, but finding the correct formula should be pursued. Finally, the turbulent formula for wall heat flux at the stagnation point used the laminar Stanton number. An undocumented assumption was used here and should be further investigated.

Besides the potential follow-on work described above, the completed code verification should provide value to the SPARC code development team. The tests developed and used in the present study have been shared with the code development team along with documentation of both models, allowing for more informed and efficient testing of future implementations.

# 3. HIFIRE-1 WIND TUNNEL TESTS

Experimental data are critical to validation studies, but there are few presented in the public literature for hypersonic aerodynamic vehicles, possibly due to the challenges of measurements under these extreme conditions or the sensitivities of the applications. There are a handful of tests that include a mix of flight and ground tests. These two types have benefits and drawbacks. Flights tests are closer to the intended uses of MFTK, but measurement quantity and quality for aero-only quantities are challenging. Most flight tests of hypersonic vehicles require a thermal protection system that complicates the direct measurement of aerodynamic quantities such as surface pressure, temperature, and heat flux. Also, flight test conditions are only loosely controlled and measured. Conversely, ground tests are farther from the intended uses of MFTK, but enable greater instrumentation and control of conditions. Many ground test facilities are shock tunnels that induce hypersonic conditions for a fraction of a second, eliminating the need for thermal protection systems.

Many potential validation data sources were surveyed for this work. One source of hypersonic aerodynamic validation data is the Hypersonic International Flight Research and Experimentation (HIFiRE) program that sought to develop hypersonic technologies. The program included atmospheric flight tests and ground tests in the shock tunnel facilities at the Calspan–University at Buffalo Research Center (CUBRC). Their Large Energy National Shock (LENS) facilities include LENS I, LENS II, and LENS XX [10]. Of particular interest are the HIFiRE-1 wind tunnel tests that have been used for validation data in a number of subsequent publications that were conducted in the LENS I shock tunnel [8].

The HIFiRE-1 wind tunnel tests were selected for a validation application due to hypersonic flow conditions, challenging flow characteristics, turbulence, testing with air, and a wealth of high-quality data that spans a range of angles of attack and Reynolds numbers [8]. One down-side is the low enthalpy conditions in the flow that will not exercise the reacting gas models in the MFTK RANS implementation. The HIFiRE-1 flight test was not selected due to the coning motion during reentry that makes it less ideal for validation [13].

The geometry of the test article used in the HIFiRE-1 wind tunnel tests is shown in Figure 3-1. The test article has a complex shape with a slender 7° half-angle fore-cone, a cylindrical section in the center, then a blunt flare at the rear. The figure shows most features of the test article well, but does not show the short cylindrical extension after the flare, which was present in the experiments and is modeled. Depending on the run configuration, turbulent transition occurs naturally or is tripped on the fore-cone. The flare causes a separation bubble in the cylindrical section that is a challenge for many RANS models [10]. The test series had a total of over 50 runs in two phases and the model contains a total of 106 heat flux sensors and 60 pressure sensors that are located at four different meridional angles. Phase I of the experimental study was conducted to determine optimal nose radius and flare angle, which were then used in Phase II. All experimental data used in the present study are from Phase II runs. It may be noted that the 0° meridional angle is the most heavily instrumented, and that this angle is located on the windward side of the body when the angle of attack ($\alpha$) is nonzero.

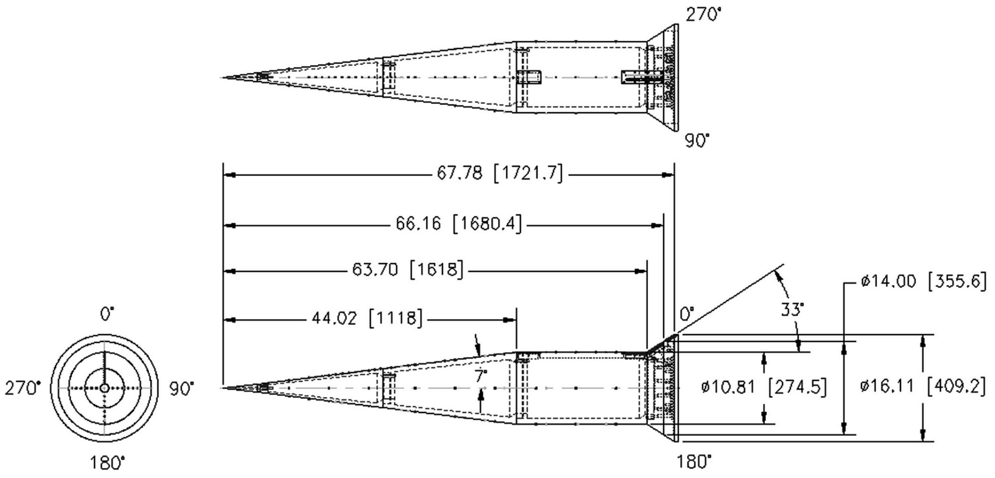

| NUMBER OF INSTRUMENTS PER SECTION | | | | | | | | |
|---|---|---|---|---|---|---|---|---|
| | CONE | | CYLINDER | | FLARE | | EXTENSION | |
| | HEAT | PRES | HEAT | PRES | HEAT | PRES | HEAT | PRES |
| PHASE I | 32 | 6 | 17 | 4 | 0 | 0 | 0 | 0 |
| PHASE II | 47 | 11 | 33 | 28 | 17 | 17 | 9 | 4 |

**Figure 3-1.** The HIFiRE-1 wind tunnel test geometry, showing the fore-cone on the left, the cylindrical section in the center, and the flare on the right, from [10]. Note that the nose radius is 2.5 mm.

For this study, the number of runs was expanded from one (Run 30, in [1]) to four. The runs analyzed span most of the Reynolds number – angle of attack space shown in Figure 3-2, with symmetry for positive and negative angles of attack being exploited to reduce the number of runs analyzed. The runs with positive angle of attack have the windward side on the 0° meridional angle, so as to utilize the much higher number of sensors on the side which experiences earlier transition and more extreme physics. The runs analyzed in this study were chosen such that laminar and turbulent flow was present in each, and two sets of runs were similar in Reynolds number (Runs 30 and 34 around 1e7 $m^{-1}$, Runs 38 and 42 around 3.5e6 $m^{-1}$), while two sets of runs were also similar in angle of attack (Runs 30 and 38 at 0°, Runs 34 and 42 at 2°). The flow was manually tripped to initiate transition to turbulence in Runs 38 and 42. At a given angle of attack, the Reynolds number was varied primarily by changing the freestream density (roughly 100 percent difference in density versus less than 5 percent difference in freestream velocity). Not only did these runs provide an opportunity to perform a more thorough validation comparison, they also allowed for examination of model performance under varying conditions. Two questions that were examined in this study were the performance of each of the MFTK models at lower Reynolds numbers (are the models more accurate for lower Reynolds number?) and at nonzero angle of attack (are models less accurate for nonzero angle of attack?).

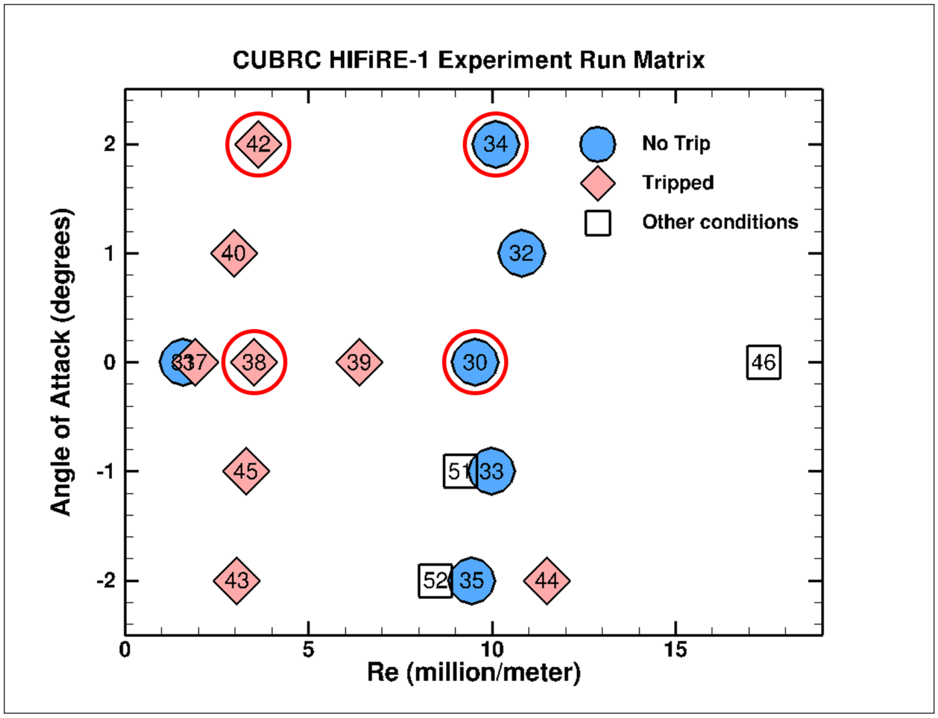

**Figure 3-2.** Map of HIFiRE-1 runs showing parameter space analyzed in this study.

To provide a sense of the flow field, the Mach number predictions in a two-dimensional, axisymmetric, wall-normal plane for two RANS models are shown in Figure 3-3. The flow is left to right. The solid wind tunnel model is the white region in the lower right and includes the cone, the cylinder, and the flare. The white region in the upper left is outside of the simulation domain. The RANS Spalart–Allmaras (SA) and RANS Shear Stress Transport (SST) models predict similar flow fields with the exception of the separated region near the cylinder-flare intersection that is only observed for RANS-SST.

In Figure 3-4, contour plots are shown for the center plane of RANS-SST simulations of Run 30 and Run 34. This figure highlights the major flowfield differences between results for runs at 0° angle of attack (Run 30) and those for runs at 2° angle of attack (Run 34). The main oblique shock eminating from the nosetip is thinner than that on the leeward side of the Run 34 results, but thicker than that on the windward side. Additionally, the separation region in the Run 30 results is smaller than that on the leeward side of the Run 34 results, and similar in size to that of the windward size. Comparing the leeward and windward sides of the Run 34 results directly, it can be seen that the main oblique shock from the nosetip is significantly thicker and the separation region is larger on the leeward side. The thin strip of green denoting a relatively low Mach number is also thicker on the leeward side, reflecting a thicker boundary layer due to lower bulk flow speed and reduced pressure. Finally, among other things, the surface heat flux and pressure are higher on the windward side. All of these differences are expected due to the nonzero angle of attack, and highlight the need for CFD models which accurately solve nonaxisymmetric flowfields, especially as angles of attack may be higher for the intended use of these models.

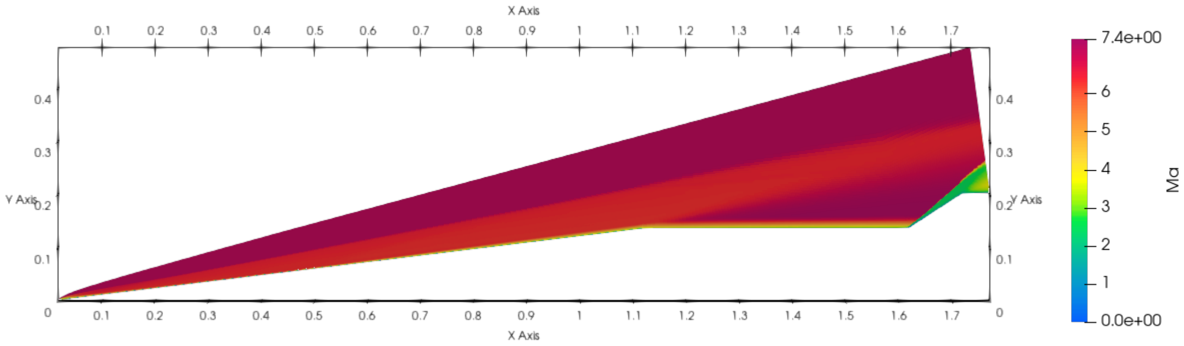

**(a)** RANS-SA

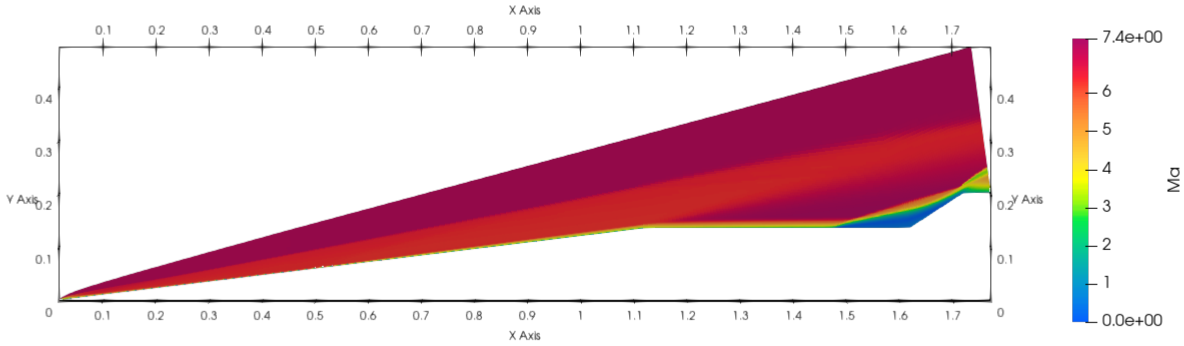

**(b)** RANS-SST

**Figure 3-3.** HIFiRE-1 wind tunnel simulation Mach number predictions for RANS-SA and RANS-SST models.

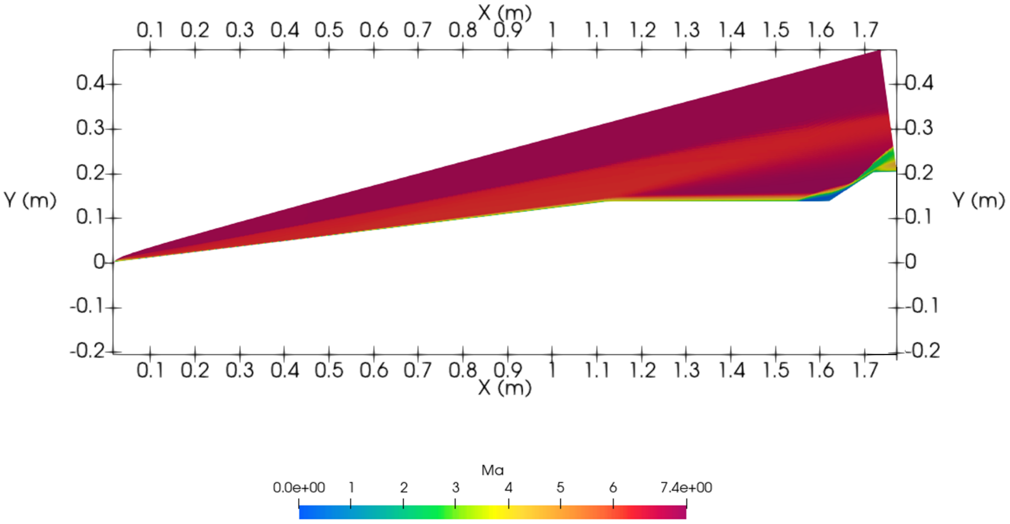

**(a)** RANS-SST, Run 30

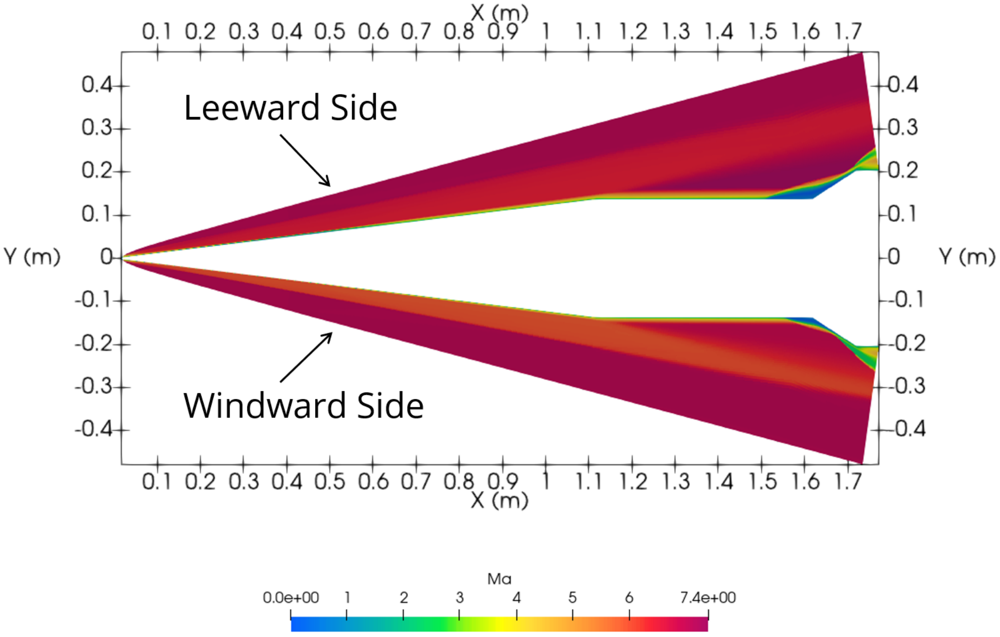

**(b)** RANS-SST, Run 34

**Figure 3-4.** HIFiRE-1 wind tunnel simulation Mach number predictions for Runs 30 and 34 using RANS-SST model.

# 4. SOLUTION VERIFICATION

Solution verification seeks to ensure that a discrete solution is sufficiently accurate for its intended use. This is crucial to complete before validation activities start because numerical errors have the potential to contaminate predictions and bias accuracy assessments in validation. Since the different models in MFTK (MNA+FPBL, Euler+MEIT, and RANS) use discrete equations to represent the continuous mathematical model, an assessment of the numerical uncertainty needs to be completed for each validation case. The grid convergence index (GCI) metric is used to assess numerical uncertainty in this study.

## 4.1. GCI Equations

The GCI metric is the most simple and popular method to assess numerical uncertainty [3]. This metric is a tailored approach for estimating numerical uncertainty, which is based on Richardson extrapolation. For a detailed description of the mathematics behind numerical uncertainty estimation using Richardson extrapolation, see [3]. The GCI method requires solutions on at least three mesh sets ($f_1$, $f_2$, and $f_3$) to compute the observed order of accuracy. Previously [1], the base case developed for the validation study produced a solution on a medium mesh, and a finer and coarser mesh were used to generate additional solutions. The numerical uncertainty previously observed tended to be higher than desired for some models and regions on the vehicle. Thus, for this study, the base (nominal) case was taken to be the fine mesh case, and solutions on two coarser meshes were obtained. These meshes were coarsened by a factor of two (refinement ratio $r = 2$) each with respect to the next finest mesh. Since the MNA+FPBL model is a panel method, whereas Euler and both RANS models are control-volume methods, two separate mesh triplets were previously generated. Another improvement in this study was the generation of a third mesh triplet specifically for the Euler model, as it does not require a refined near-wall region to resolve the viscous boundary layer (BL). Figure 4-1 shows the coarsest 3D surface mesh used for the MNA+FPBL model, whereas Figure 4-2 shows the coarsest 2D axisymmetric volume mesh used for the Euler model, and Figure 4-3 shows the coarsest 2D axisymmetric volume mesh used for both RANS models. These are volume meshes in the sense that the domain which they represent is the volume around the vehicle, under an axisymmetric assumption. For both the MNA+FPBL and Euler meshes, the only significant mesh refinement is near the nose-cone region since large gradients are expected in this region, whereas the RANS meshes also have significant wall-normal mesh refinement for viscous boundary layer resolution. Each figure focuses on the mesh resolution details in the nose-cone region. The medium and fine cell sizes can resolve length scales approximately two- and four-times smaller than the coarse cell sizes, respectively.

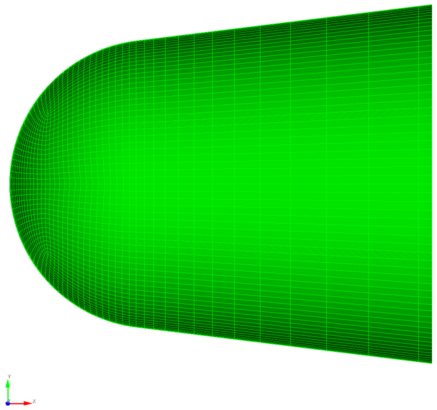

**Figure 4-1.** MNA+FPBL coarse surface mesh example in nose-cone region.

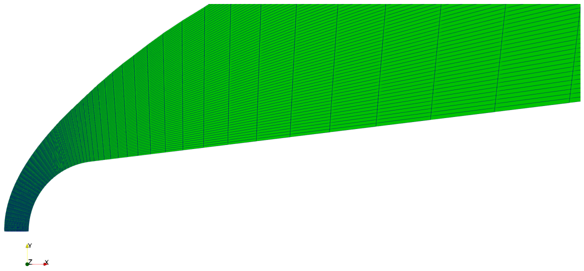

**Figure 4-2.** Euler coarse mesh example in nose-cone region.

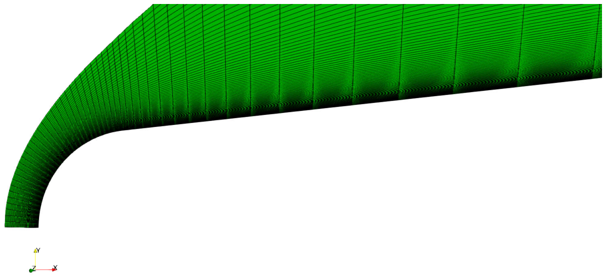

**Figure 4-3.** RANS coarse mesh example in nose-cone region.

This provides enough information to compute the observed order of accuracy, $p_{\mathrm{obs}}$, which is

$$p_{\mathrm{obs}} = \frac{\ln\left(\frac{f_3 - f_2}{f_2 - f_1}\right)}{\ln r}. \tag{4.1}$$

Once we compute the $p_{\mathrm{obs}}$, a factor of safety, $F_s$, is chosen. This factor of safety turns the discretization error estimate into a 95% confidence interval. When the difference between $p_{\mathrm{obs}}$ and the theoretical order of accuracy, $p_{\mathrm{th}}$, is smaller than 10%, $F_s = 1.25$. For all other cases, $F_s = 3.0$ [3]. While multiplying the estimated discretization error significantly inflates the reported error, being close to or outside the asymptotic range can negatively impact the quality of the Richardson extrapolation. Additionally, when $p_{\mathrm{obs}}$ is positive, but larger in magnitude than $p_{\mathrm{th}}$, it is conservative to use $p_{\mathrm{th}}$ in the GCI metric, which will be seen in the order-of-accuracy plots below as a ceiling. When $p_{\mathrm{obs}}$ is smaller in magnitude than $p_{\mathrm{th}}$, it is conservative to use $p_{\mathrm{obs}}$ in the GCI metric. For the case when $p_{\mathrm{obs}}$ is positive, but less than 0.5, the order of accuracy is set to 0.5, which will be seen in the order-of-accuracy plots below as a floor. Allowing the order of accuracy used in the metric to be significantly larger than the formal order produces unreasonably small uncertainty estimates, while allowing the order of accuracy to go to zero produces unreasonably large uncertainty estimates. Moreover, scientific computing codes are typically of order 1 or higher, and an order of less than 0.5 thus falls significantly below the expected range. For the case when $p_{\mathrm{obs}}$ is negative, this suggests that the simulation is non-convergent and numerical uncertainty cannot be estimated. With these limitations on the order of accuracy, very large or small uncertainty values are avoided, while an appropriate level of conservatism is retained. Now that $F_s$ and $p$ are known, the GCI metric is computed using Equation (4.2).

$$\mathrm{GCI} = F_s \frac{|f_2 - f_1|}{(r^p - 1)} \tag{4.2}$$

## 4.2. Solution Verification Assessment

For the solution verification assessment, the numerical uncertainty is quantified for all model combinations used in the validation study of the HIFiRE-1 wind tunnel test in Chapter 5. To assess the numerical uncertainty for each simulation case, the GCI is computed in the streamwise direction along the vehicle surface at three unique meridional angles (0°, 90°, 180°). The model fidelities assessed are MNA+FPBL, Euler+MEIT, and RANS. Since the validation assessment is performed on the pressure ($P$) and wall heat flux ($q_w$), the solution-verification assessment needs to quantify the numerical uncertainty for those QoIs. In addition to the normalized GCI values, we report simulation results for each level of refinement to quickly assess the mesh sensitivity. Lastly, we also report the observed order of accuracy to show how well the numerical method is performing. For all simulation results, the theoretical order of accuracy is assumed to be two, due to second-order discretization methods for each model.

### *4.2.1. MNA+FPBL*

The MNA+FPBL model has the option of three different viscous models: flat-plate laminar and flat-plate turbulent using either the van Driest or White models. Both the laminar and van Driest models are used in each simulation case, and ultimately laminar and turbulent solutions are stitched together at the transition location for the validation analysis. In the solution-verification effort, each model is analyzed separately over the entire geometry for each simulation case. The results are shown in Figures 4-4 through 4-12 for a series of experimental runs from the HIFiRE-1 wind tunnel tests. The series of runs used is described further in Section 3. For the heat flux order of accuracy, a moving mean with a window of 10,000 data points is plotted in black to more clearly show the average trend. Note that the HIFiRE-1 geometry is shown as a shaded figure in the background of each plot to show the increase in uncertainty due to changes in geometry. Additionally, inset plots are added to the GCI plots, which show a magnified view of the QoI trends on the flare. Inset plots are also shown for sections of the cylinder and cone in Figure 4-5. These inset plots show that, in general, the simulation results converge to the fine grid results, with the medium grid solution being closer to the fine grid solution than the coarse grid solution is. This trend is checked along the entire vehicle for all cases by computing the absolute value of the difference between the medium and fine, and coarse and fine grid solutions. This check yielded the result that, in general, the medium grid solution is closer to the fine grid solution than the coarse grid solution was. This in turn pointed to the fact that the simulation results are convergent to a solution best approximated by the fine grid solution. Exceptions to this trend are the heat flux results from the MNA+FPBL simulations of Runs 34 and 42, with both the laminar and van Driest turbulence models (0° meridional angle). All simulation results are close together for these cases, but the fine grid solution shows spikes in the flare region that the other solutions do not show. This could contribute to the coarse solution being closer on average to the fine solution. These cases are noted as an anomaly, and will be further investigated. In Figure 4-5b, the trends for all three refinement levels are identical (same pressure predicted regardless of refinement level). This is the result of the MNA model's insensitivity when the angle of the geometry is 0° (see Appendix A of [1]).

For pressure, both the GCI and order of accuracy perform quite well for the laminar and van Driest cases, except near the discontinuity at the front of the nose cone, which is to be expected. This is true for all runs. We note that there is a drop in order of accuracy when the angle of the HIFiRE-1 geometry is zero, in the cylindrical portion, since the model is designed to be insensitive when the angle is 0°. The runs at 2° angle of attack (Runs 34 and 42) have higher GCI in the cone region than runs at 0° angle of attack (Runs 30 and 38). For Runs 34 and 42, the order of accuracy is two along the entire body, excluding the nosetip. This is likely due to the fact that for these cases, there is no section of the body which is at 0° with respect to the flow, since the angle of attack is nonzero. For heat flux, the results are less desirable because of the larger sensitivity to the mesh and due to the large variation in order of accuracy, although the numerical uncertainty is still quite small (approximately 4% maximum difference, excluding the nosetip). In the present study, the GCI and order of accuracy are computed at each axial mesh node on the finest mesh, which results in very detailed trends. For heat flux, the GCI fluctuates substantially, but generally decreases along the body. The order of accuracy also fluctuates, with higher magnitude fluctuations near the nosetip, on the turbulent cone, and near the flare. The fluctuations are also larger for the van

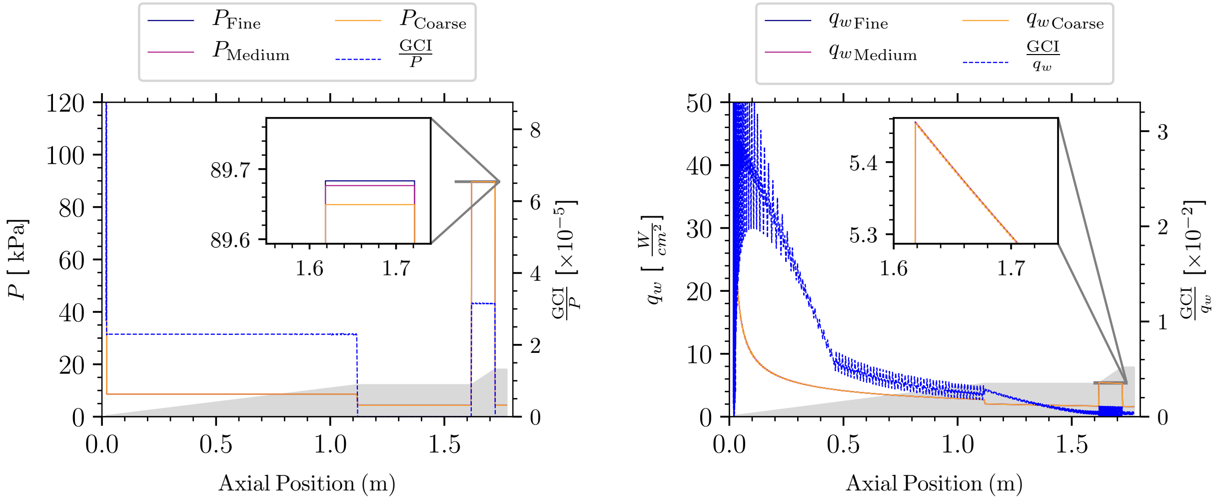

**(a)** Pressure

**(b)** Heat flux

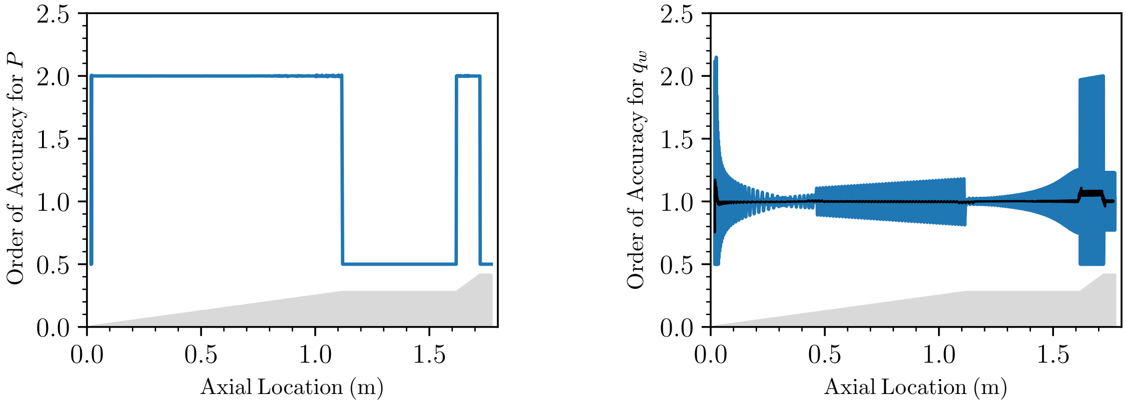

**(c)** Order of accuracy for pressure

**(d)** Order of accuracy for heat flux

**Figure 4-4.** GCI calculation for Run 30 using laminar model.

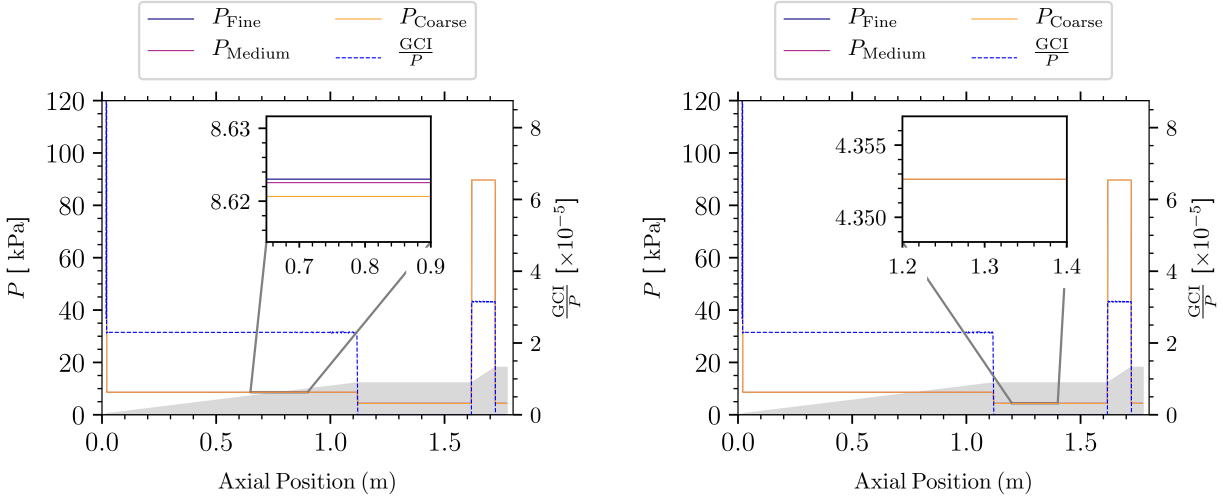

**(a)** Pressure, cone inset.

**(b)** Pressure, cylinder inset.

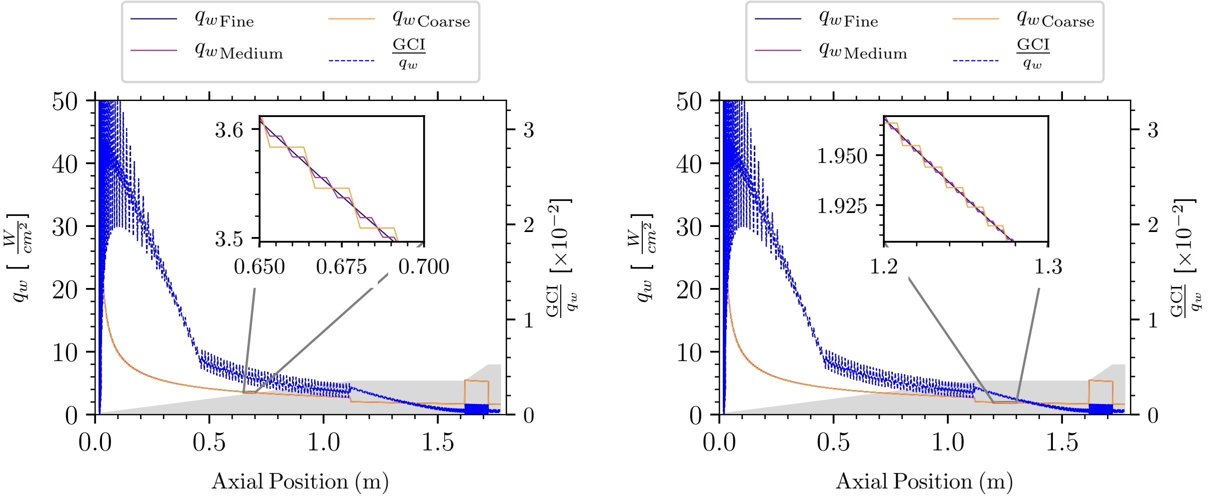

**(c)** Heat flux, cone inset.

**(d)** Heat flux, cylinder inset.

**Figure 4-5.** Pressure and heat flux plots from Run 30 with insets for cone and cylinder.

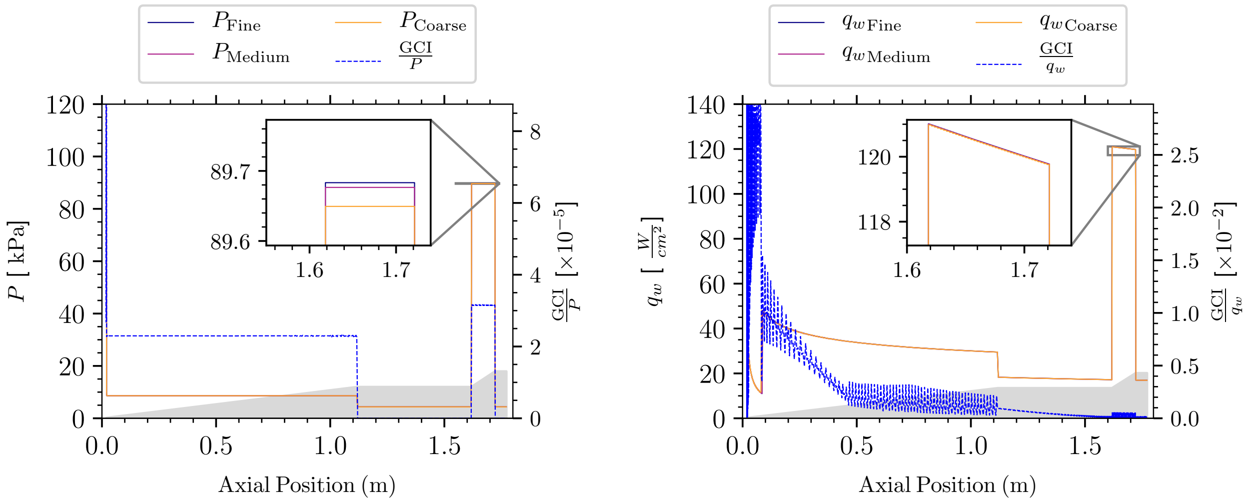

**(a)** Pressure

**(b)** Heat flux

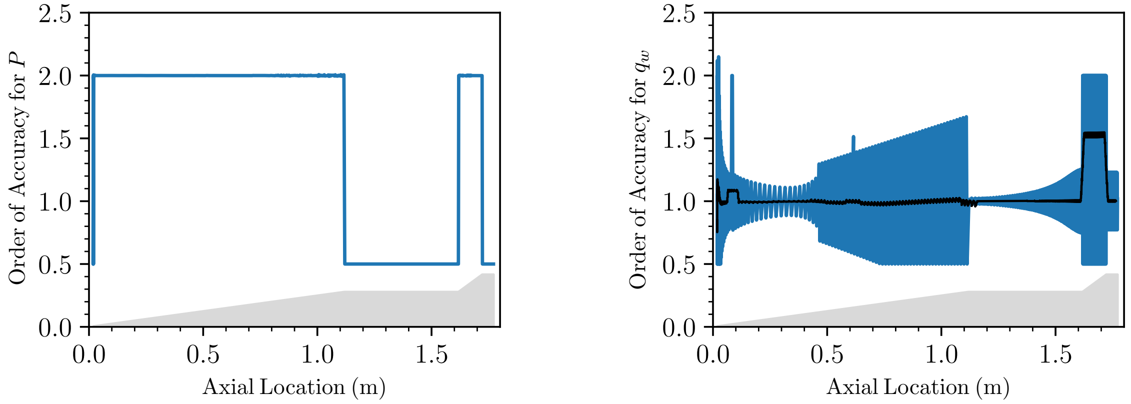

**(c)** Order of accuracy for pressure

**(d)** Order of accuracy for heat flux

**Figure 4-6.** GCI calculation for Run 30 using turbulent (Van Driest) model.

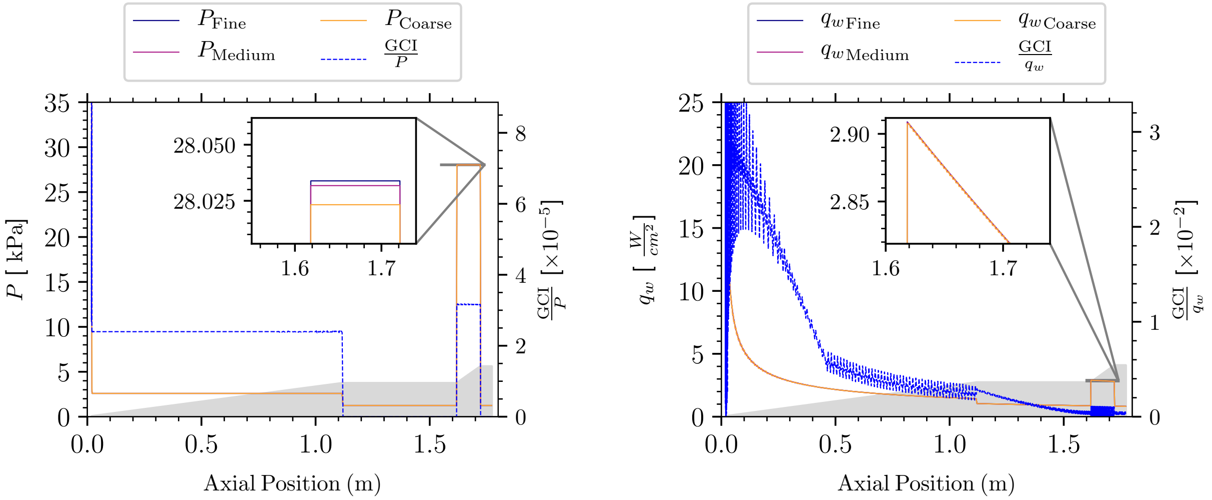

**(a)** Pressure

**(b)** Heat flux

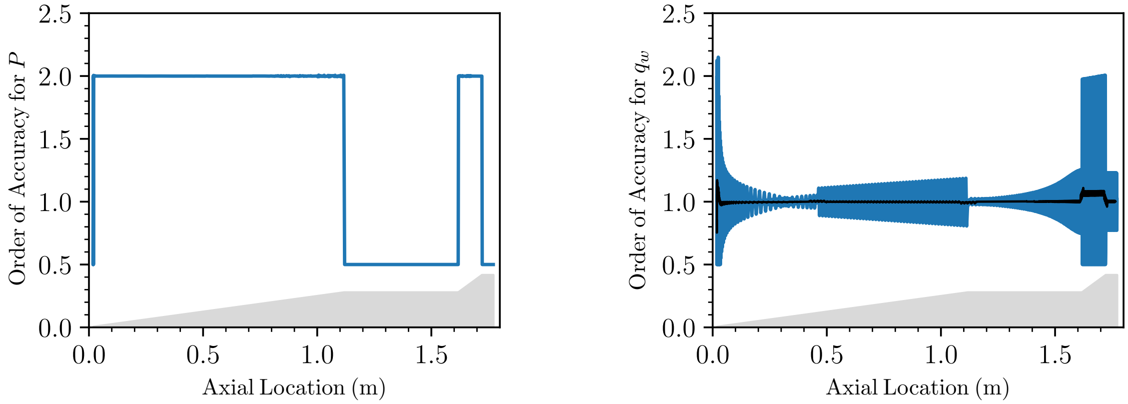

**(c)** Order of accuracy for pressure

**(d)** Order of accuracy for heat flux

**Figure 4-7.** GCI calculation for Run 38 using laminar model.

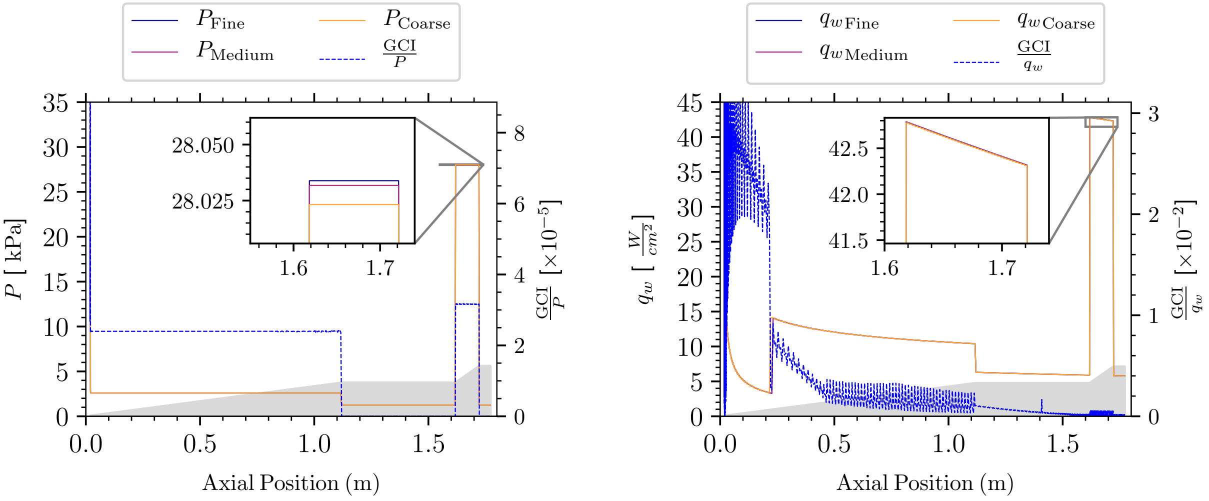

**(a)** Pressure **(b)** Heat flux

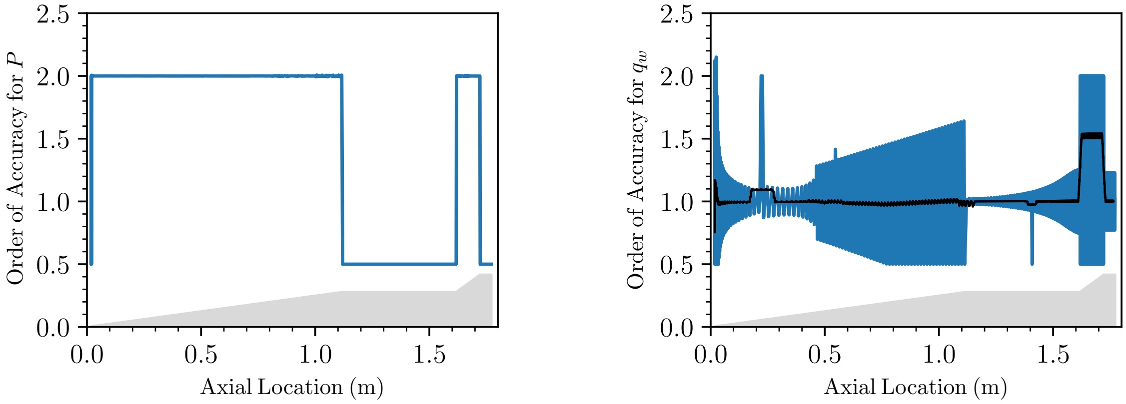

**(c)** Order of accuracy for pressure **(d)** Order of accuracy for heat flux

**Figure 4-8.** GCI calculation for Run 38 using turbulent (Van Driest) model.

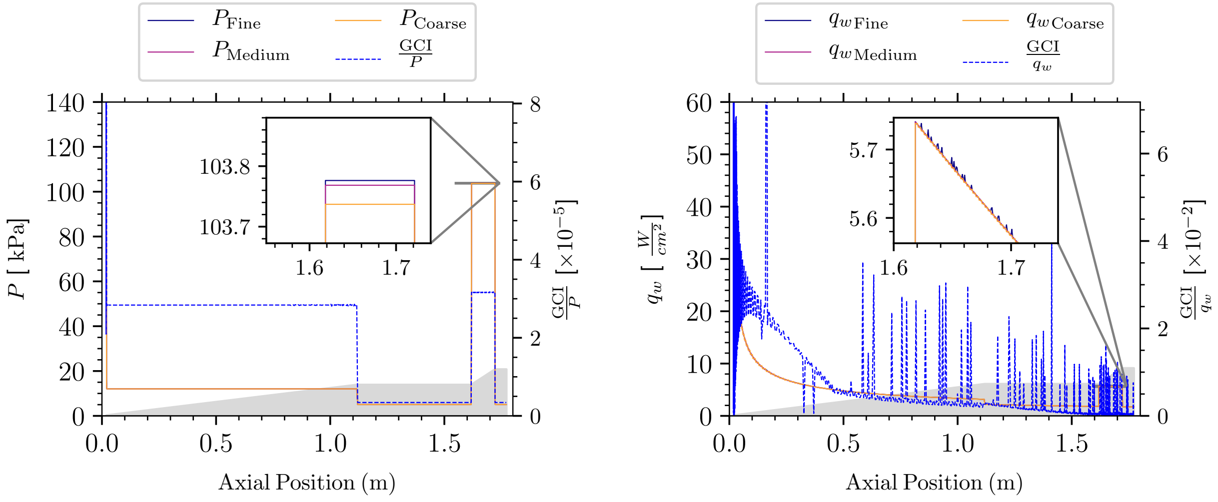

**(a)** Pressure

**(b)** Heat flux

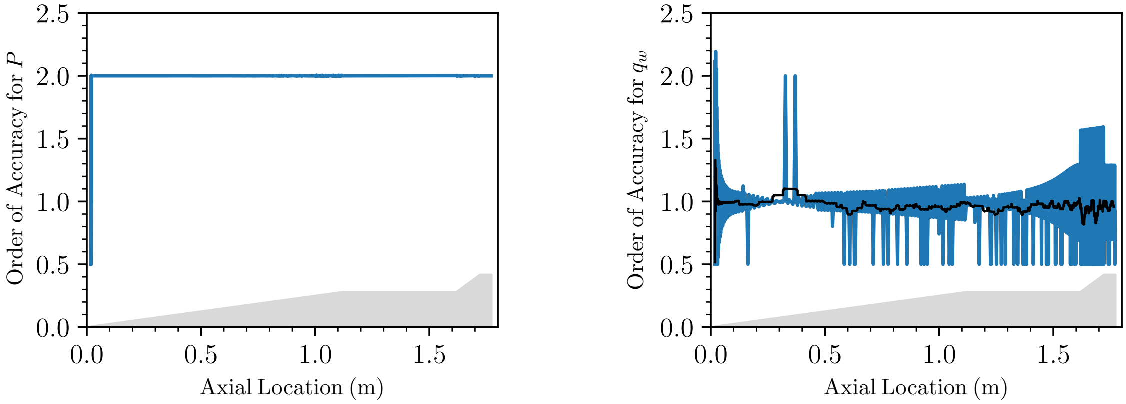

**(c)** Order of accuracy for pressure

**(d)** Order of accuracy for heat flux

**Figure 4-9.** GCI calculation for Run 34 using laminar model.

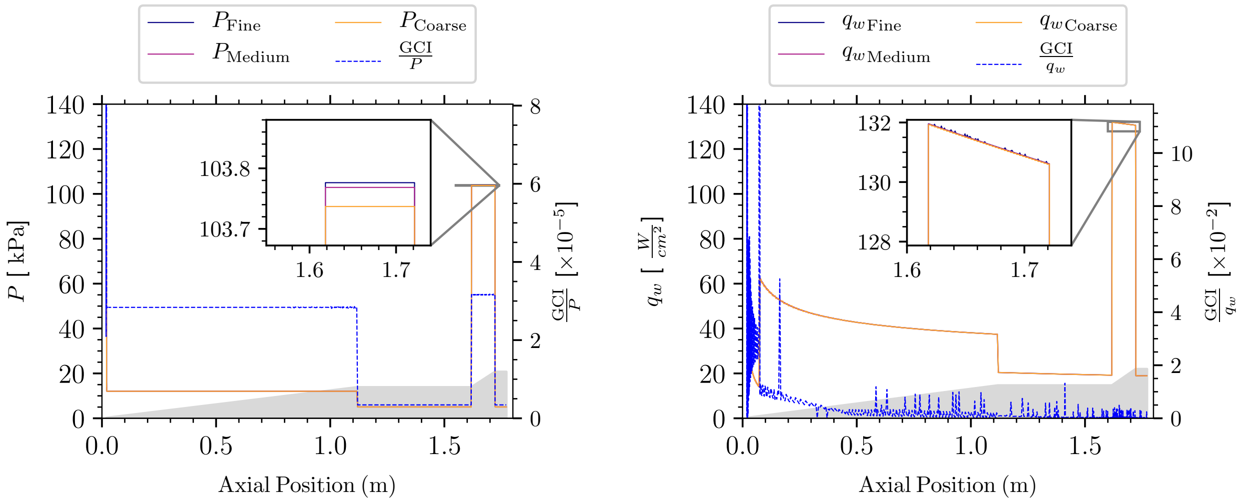

**(a)** Pressure

**(b)** Heat flux

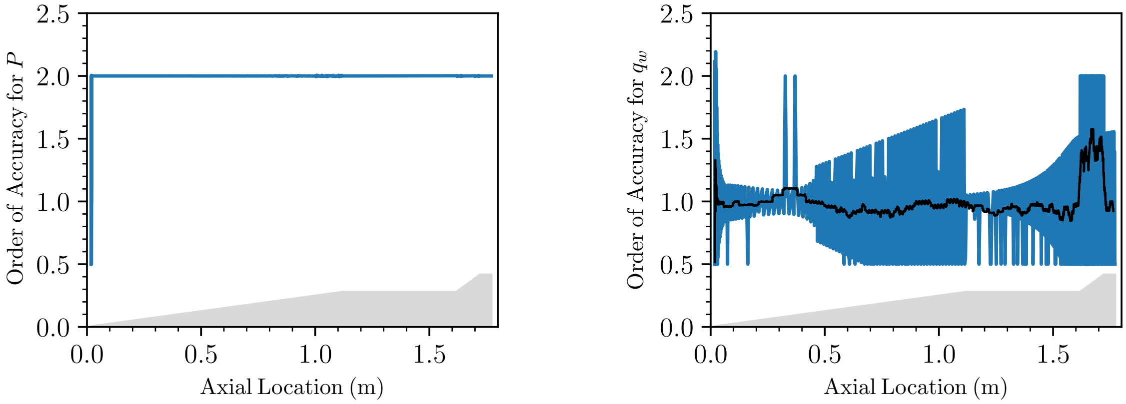

**(c)** Order of accuracy for pressure

**(d)** Order of accuracy for heat flux

**Figure 4-10.** GCI calculation for Run 34 using turbulent (Van Driest) model.

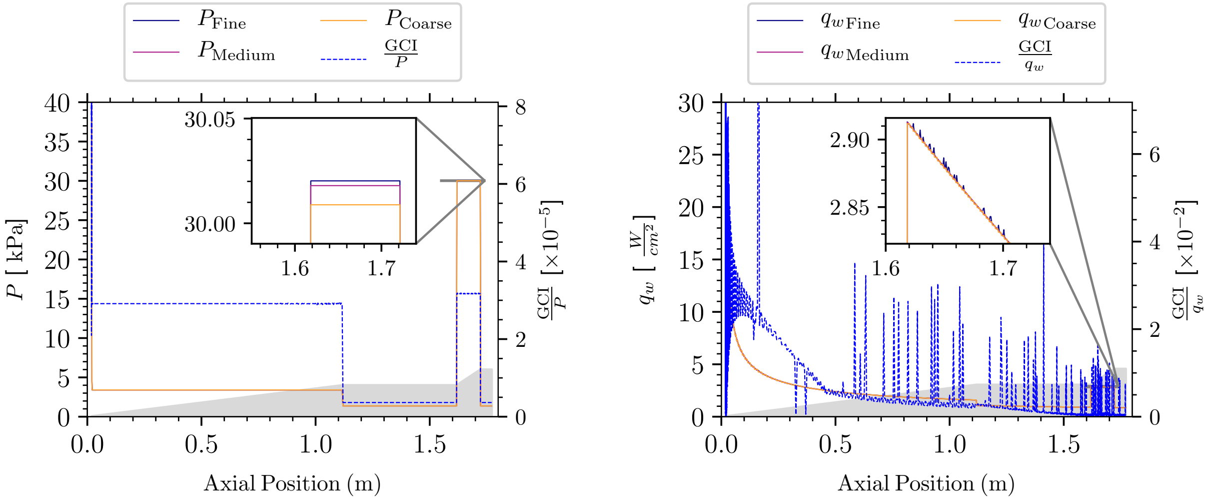

**(a)** Pressure **(b)** Heat flux

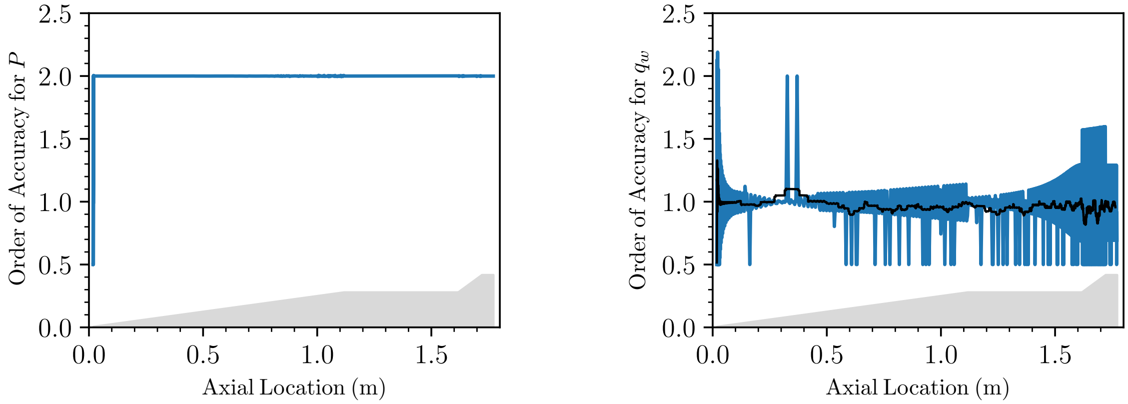

**(c)** Order of accuracy for pressure **(d)** Order of accuracy for heat flux

**Figure 4-11.** GCI calculation for Run 42 using laminar model.

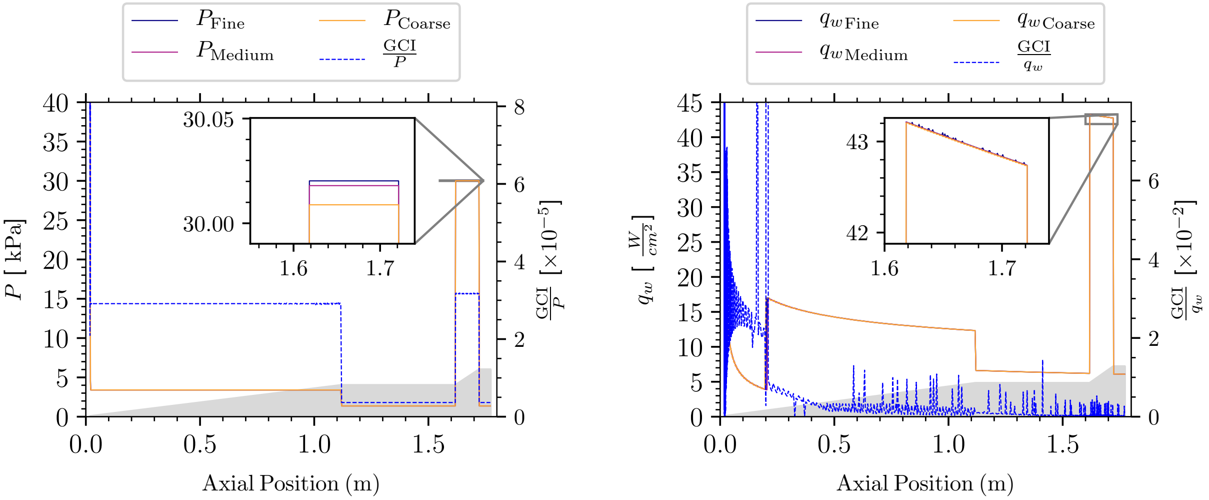

**(a)** Pressure **(b)** Heat flux

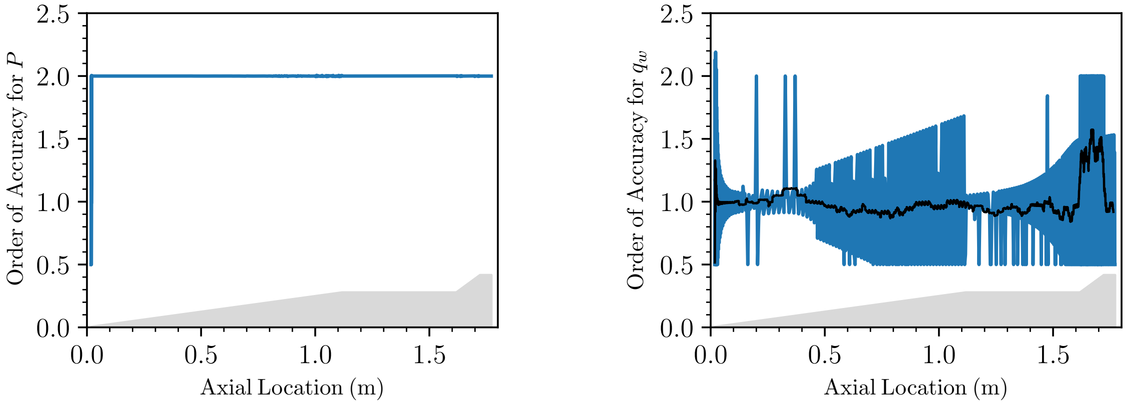

**(c)** Order of accuracy for pressure **(d)** Order of accuracy for heat flux

**Figure 4-12.** GCI calculation for Run 42 using turbulent (Van Driest) model.

Driest model than for the laminar model. In all cases, however, the order of accuracy is essentially centered at one. As mentioned above, the expected order of accuracy for the MNA+FPBL heat flux results is two, so the plots are surprising. This discrepancy could be caused by a number of factors, including the interpolation method used in the GCI calculation and the simulation details such as vehicle geometry and flow regime transition. However, since the GCI value is small, switching the factor of safety from 1.25 to 3.0 does not change the overall conclusion that MNA+FPBL has small numerical uncertainty. This phenomena is planned to be explored in the coming year.

### 4.2.2. Euler+MEIT

Results from the Euler+MEIT model are shown in Figures 4-13–4-16 for simulations of the four HIFiRE-1 runs (30, 34, 38, 42). This model represents the standard mid-fidelity option within MFTK that coincides with legacy production codes. Note that the HIFiRE-1 geometry is shown as a shaded figure in the background of each plot to show the change in uncertainty due to changes in geometry.

For pressure, there are areas in the domain that are not fully resolved with a GCI ratio of up to 50 near the flare. Generally, spikes in the GCI ratio are lower than 10 for all runs, and significantly lower for most of the body. However, these large spikes near the flare do indicate high local numerical uncertainty, which is detrimental for predictions using this model combination. Additionally, the order of accuracy confirms this lack of convergence with spikes from the order of accuracy. For heat flux, rather than modeling the laminar-to-turbulent transition region, MFTK currently switches from laminar to turbulent at the transition location (approximately $x = 0.45$ m, $x = 0.505$ m, $x = 0.404$ m, $x = 0.505$ m) for Runs 30, 38, 34, and 42, respectively. The transition location for Runs 38 and 42 is given in [8], while the other locations are deduced from the experimental heat flux curves. Heat flux trends show distinct increases at the transition location, consistent with theory. This approach is taken as this effort is focused on assessing model accuracy for predicting quantities of interest and not for predicting transition, a challenge to current research outside the scope of this work. Including both laminar and turbulent solutions is a relatively new addition to MFTK. At the transition location, the GCI ratio spikes substantially (notice Run 34 results in particular), which indicates the manual method of modeling the transition region could use improvement. Currently, the Euler+MEIT model contains the ability to prescribe transition at a manually set point, and shifts the model form at that point. To improve the transition modeling, a more complex transition model could be employed in the future. This transition model should include a length scale in the transition region to ensure a resolvable transition model. In addition to the transition region, the sharp aft (near-flare) region appears to be under-resolved, and for the runs at nonzero angle of attack (Runs 34 and 42), the cone-cylinder intersection is another region with high GCI values. We note that the levels of numerical uncertainty from this study are similar to those of [1], though the GCI used in this study is computed using results from the two finest meshes rather than the two coarsest meshes, as in [1]. The very large spikes in GCI in this study are due to the greatly increased spatial resolution of the calculation, and other application-specific elements contributing to the numerical uncertainty are possible. However, the results also point to the potential need for reduction of numerical uncertainty in the Euler+MEIT model.

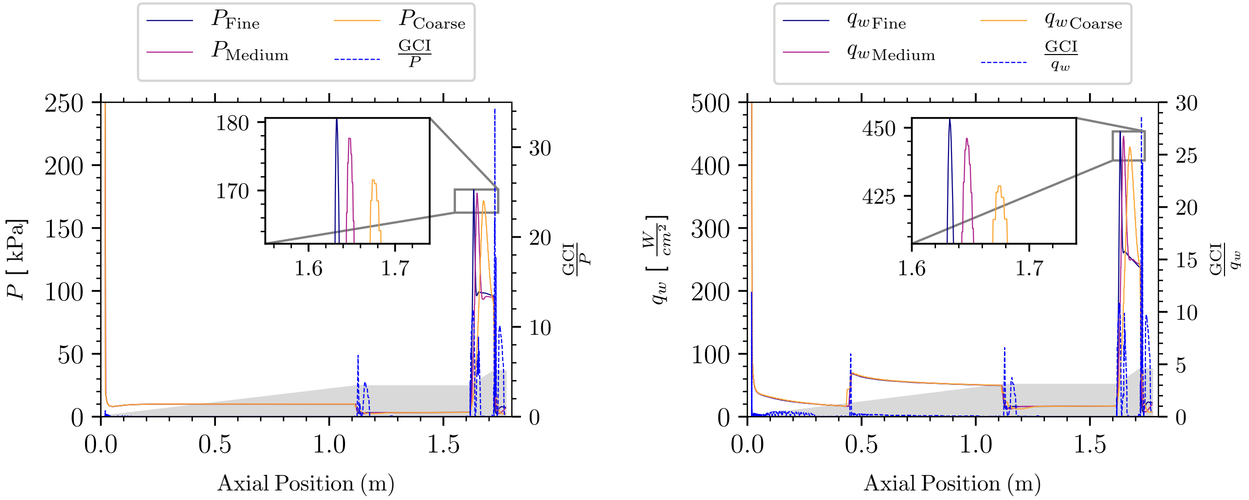

**(a)** Pressure

**(b)** Heat flux

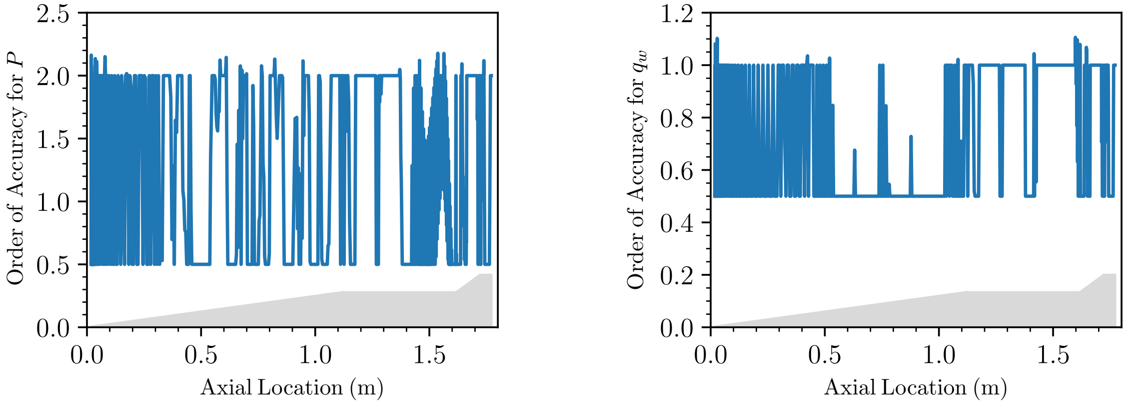

**(c)** Order of accuracy for pressure

**(d)** Order of accuracy for heat flux

**Figure 4-13.** GCI calculation for Euler+MEIT model, Run 30.

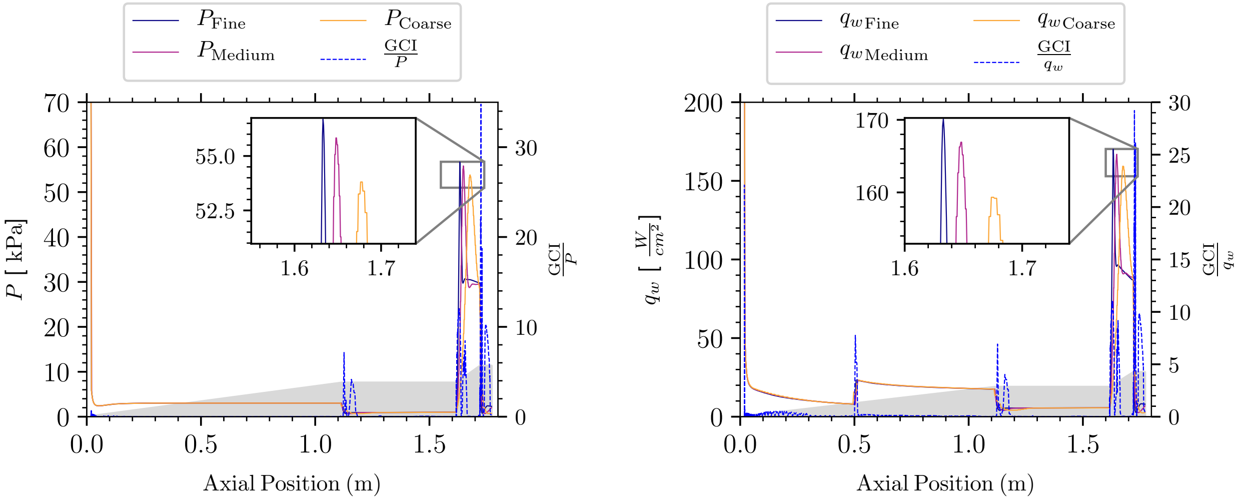

**(a)** Pressure

**(b)** Heat flux

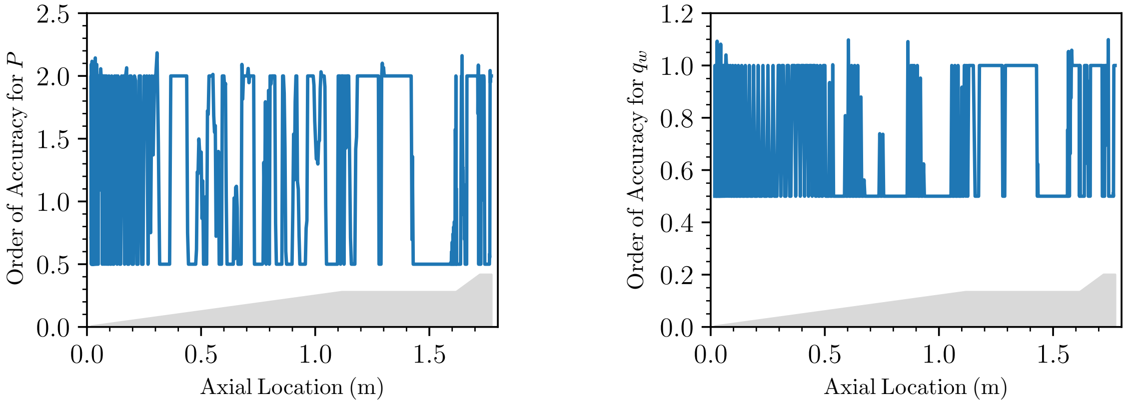

**(c)** Order of accuracy for pressure

**(d)** Order of accuracy for heat flux

**Figure 4-14.** GCI calculation for Euler+MEIT model, Run 38.

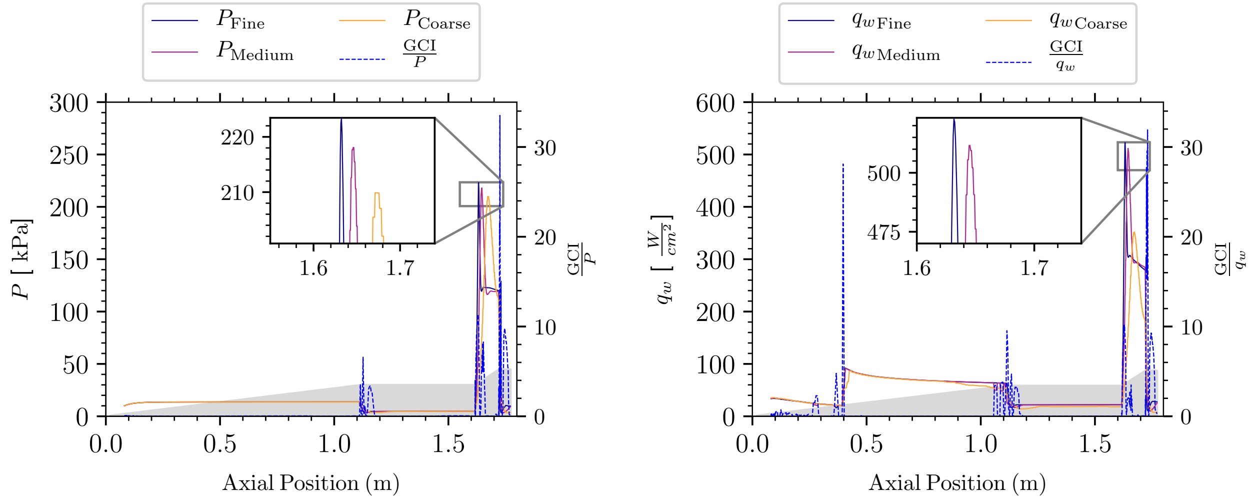

**(a)** Pressure **(b)** Heat flux

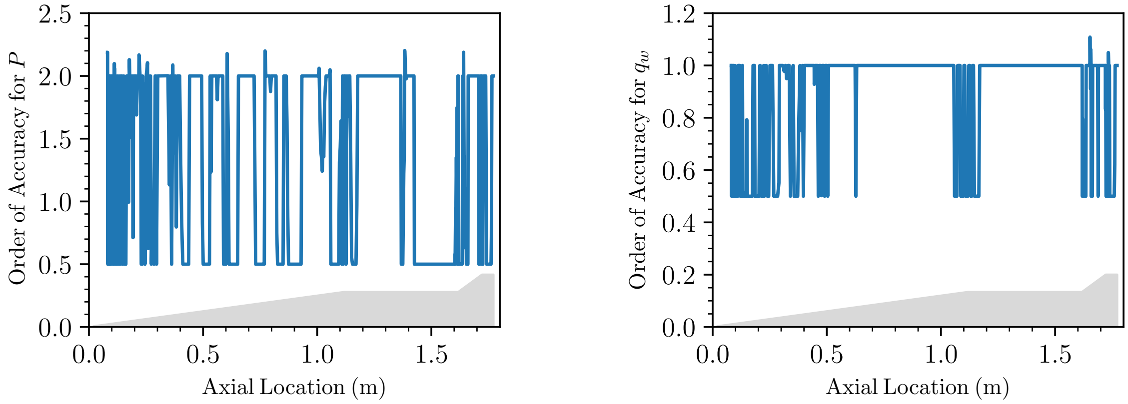

**(c)** Order of accuracy for pressure **(d)** Order of accuracy for heat flux

**Figure 4-15.** GCI calculation for Euler+MEIT model, Run 34.

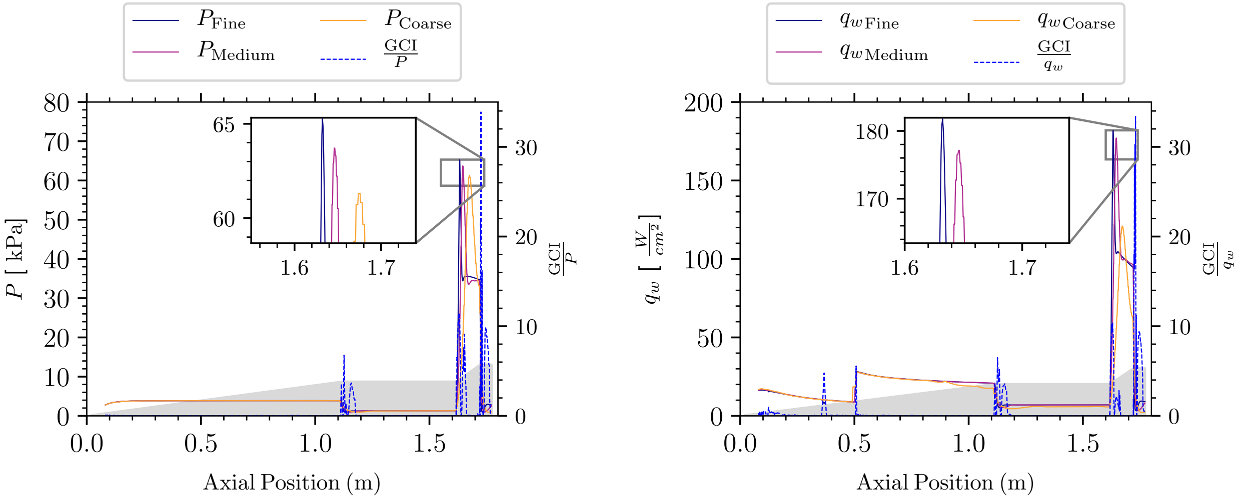

**(a)** Pressure

**(b)** Heat flux

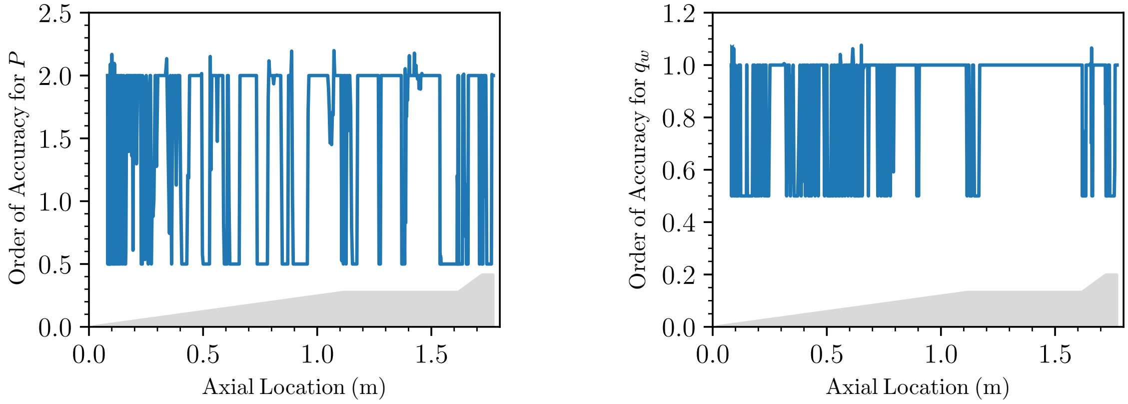

**(c)** Order of accuracy for pressure

**(d)** Order of accuracy for heat flux

**Figure 4-16.** GCI calculation for Euler+MEIT model, Run 42.

### 4.2.3. RANS

The RANS model has the option of two different viscous models: Spalart–Allmaras (SA) and Shear Stress Transport (SST). GCI results for the RANS-SA model simulations are shown in Figures 4-17–4-20, while results for the RANS-SST simulations are shown in Figures 4-21–4-24. These cases represent the high-fidelity options within MFTK. Note that the HIFiRE-1 geometry is shown as a shaded figure in the background of each plot to show the increase in uncertainty due to changes in geometry.

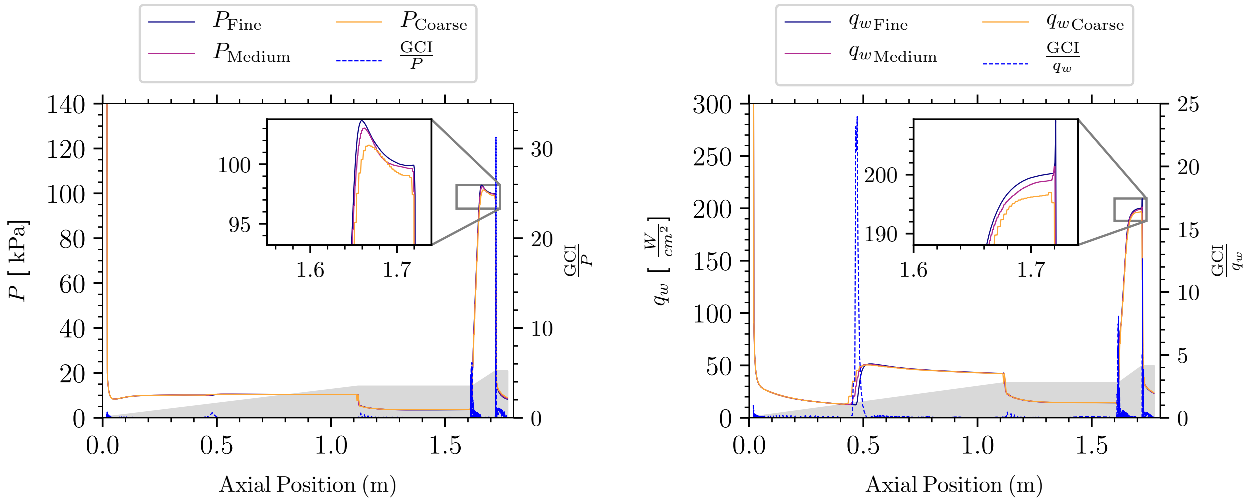

**(a)** Pressure **(b)** Heat flux

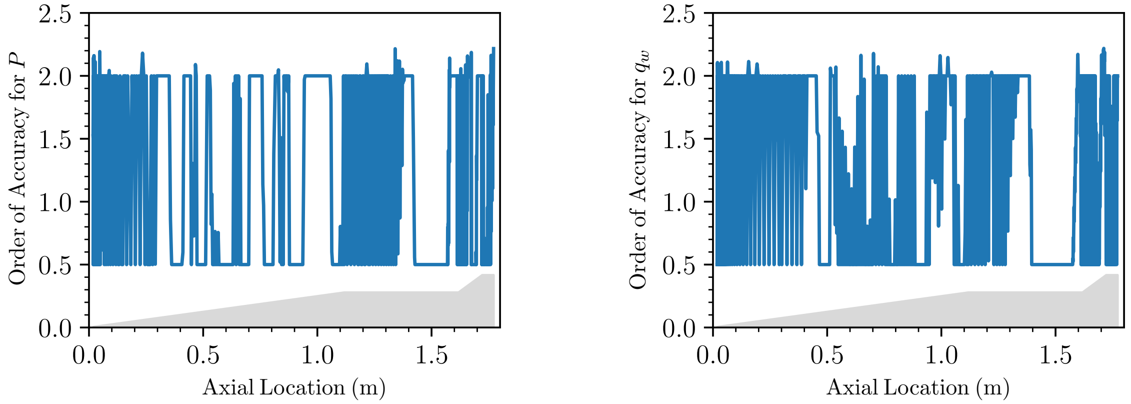

**(c)** Order of accuracy for pressure **(d)** Order of accuracy for heat flux

**Figure 4-17.** GCI calculation for RANS-SA simulation of Run 30.

For pressure, the GCI and order of accuracy for the SA model appear to perform better than the SST model. The order of accuracy of the SA model dwells near 2 more than that of the SST model, and spikes in the GCI are generally fewer in number and lower in magnitude. The effects of this are seen clearly in the shaded regions surrounding error curves in the validation section of this report. For heat flux, the results are similar to pressure where the GCI and order of accuracy for the SA model generally perform better than the SST model.

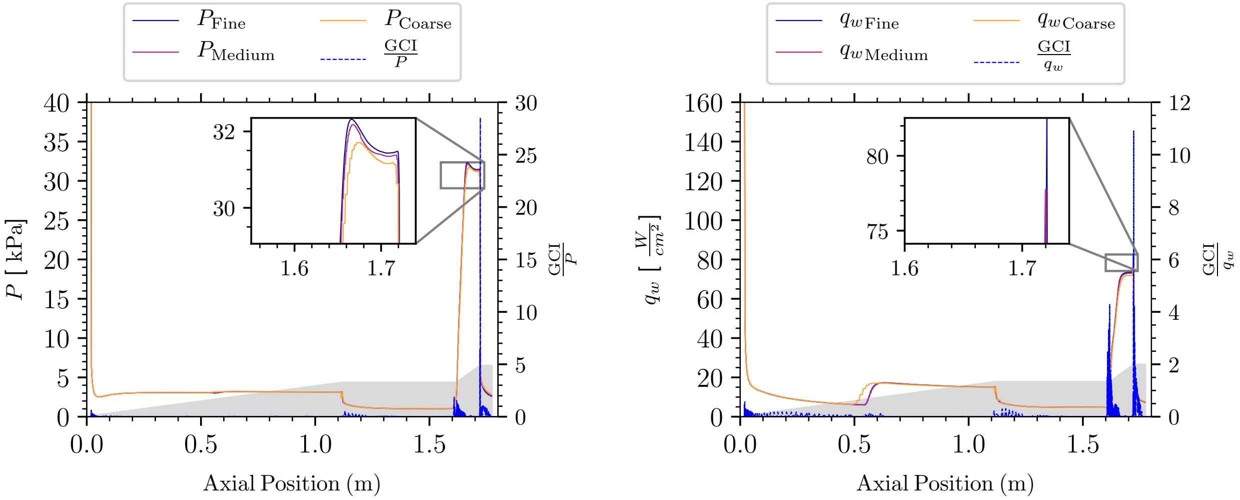

**(a)** Pressure

**(b)** Heat flux

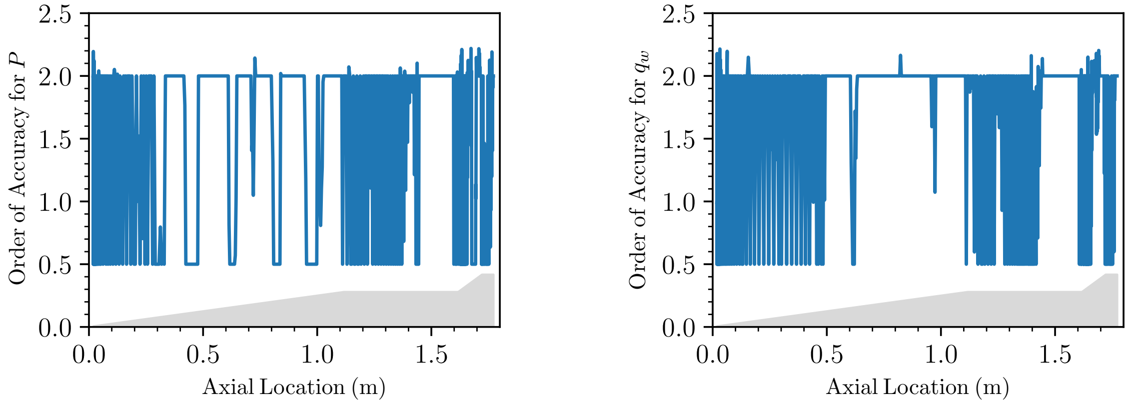

**(c)** Order of accuracy for pressure

**(d)** Order of accuracy for heat flux

**Figure 4-18.** GCI calculation for RANS-SA simulation of Run 38.

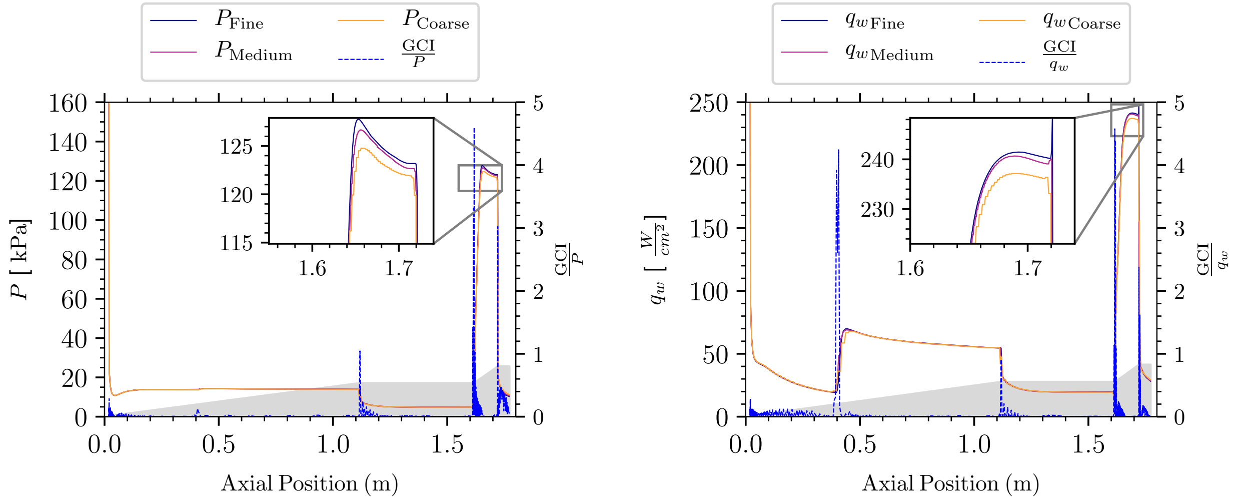

**(a)** Pressure

**(b)** Heat flux

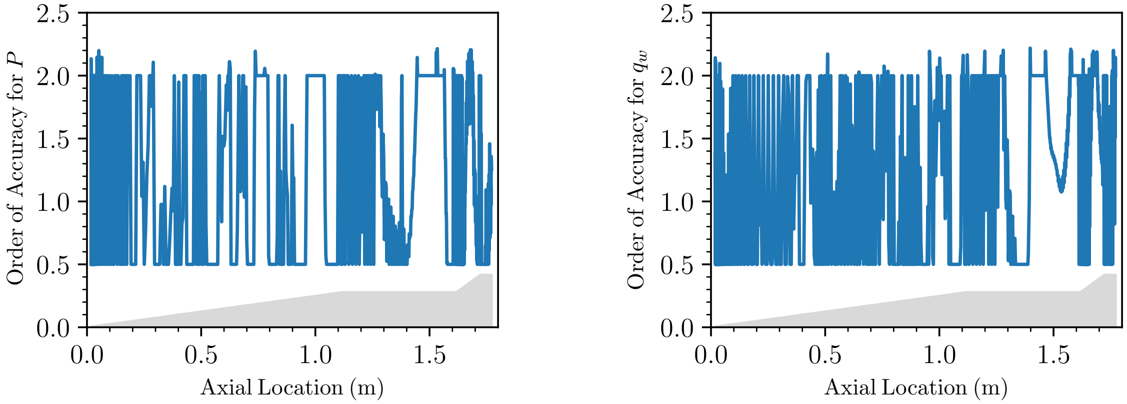

**(c)** Order of accuracy for pressure

**(d)** Order of accuracy for heat flux

**Figure 4-19.** GCI calculation for RANS-SA simulation of Run 34.

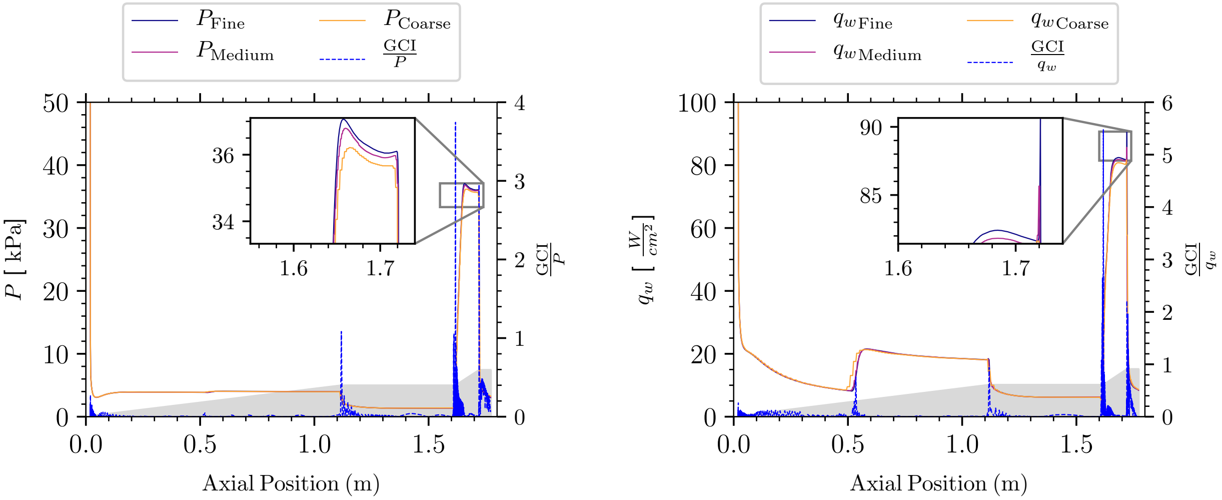

**(a)** Pressure

**(b)** Heat flux

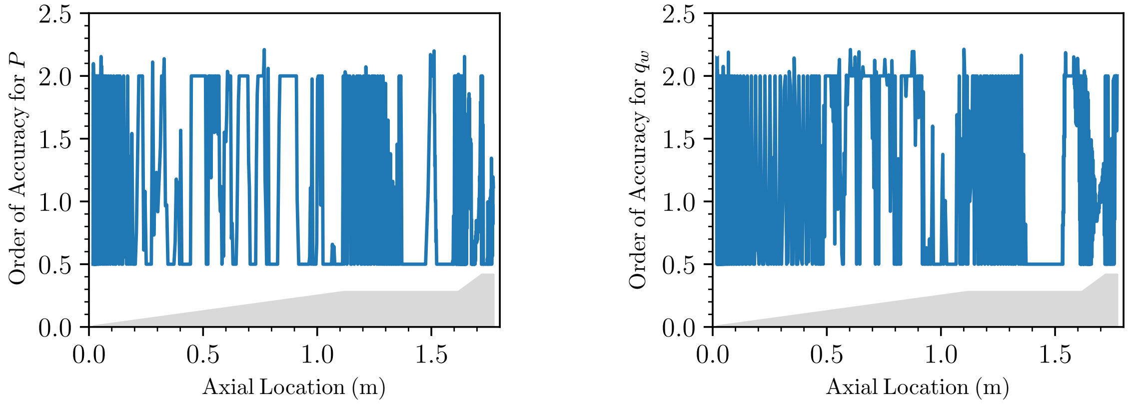

**(c)** Order of accuracy for pressure

**(d)** Order of accuracy for heat flux

**Figure 4-20.** GCI calculation for RANS-SA simulation of Run 42.

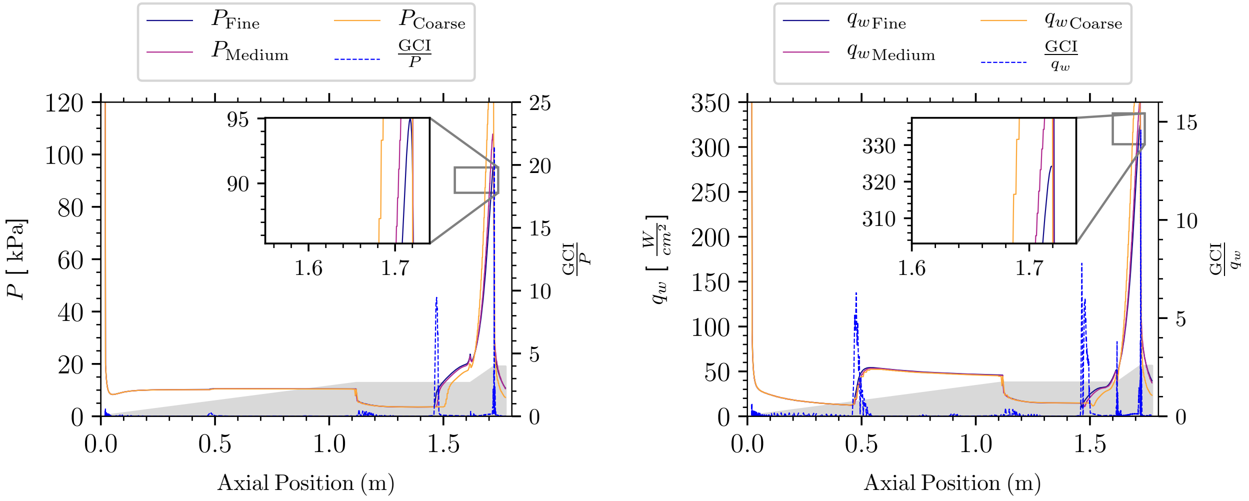

**(a)** Pressure

**(b)** Heat flux

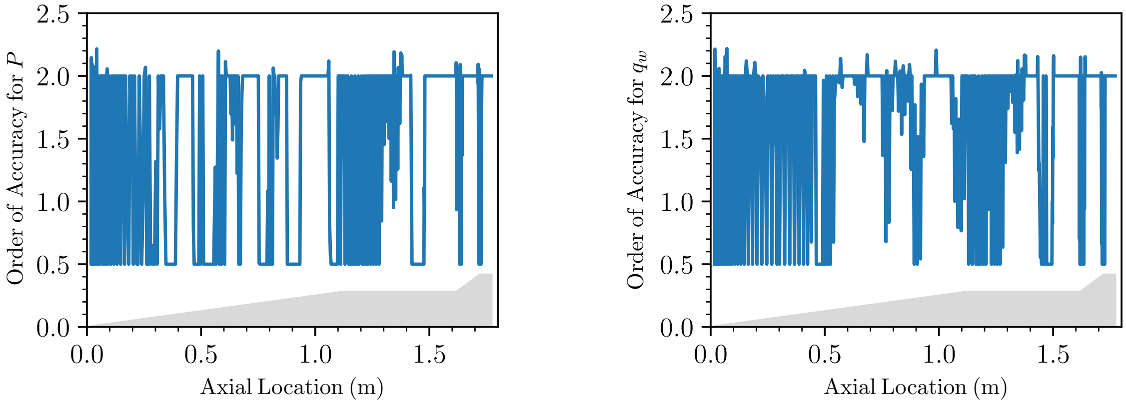

**(c)** Order of accuracy for pressure

**(d)** Order of accuracy for heat flux

**Figure 4-21.** GCI Calculation for RANS-SST simulation of Run 30.

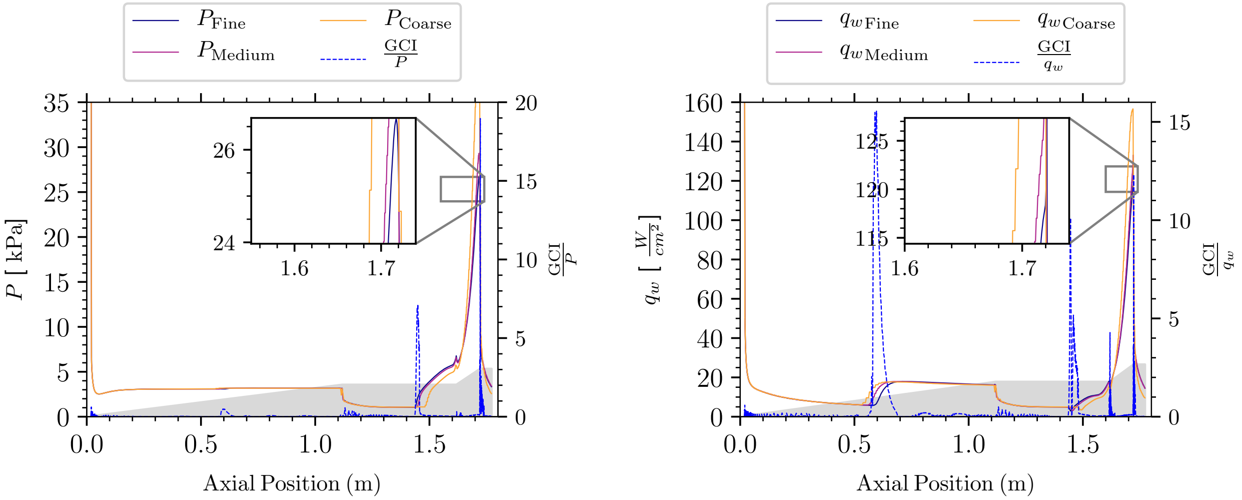

**(a)** Pressure **(b)** Heat flux

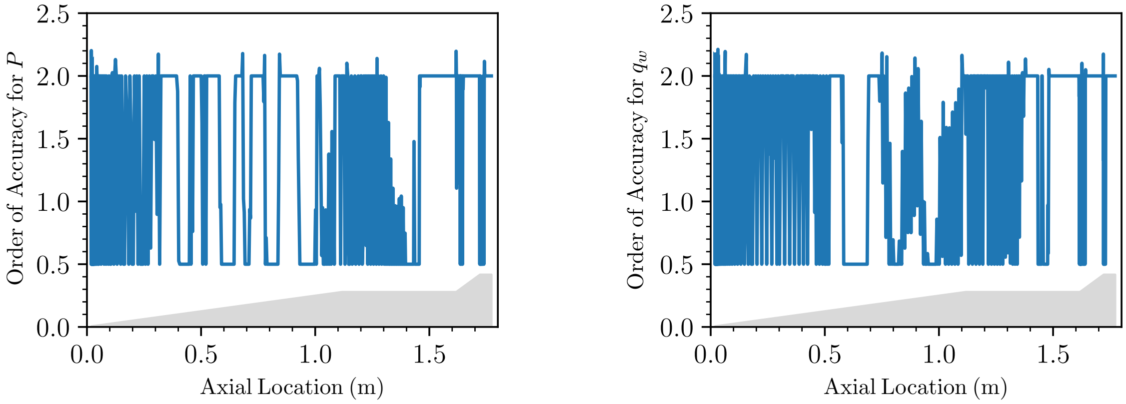

**(c)** Order of accuracy for pressure **(d)** Order of accuracy for heat flux

**Figure 4-22.** GCI Calculation for RANS-SST simulation of Run 38.

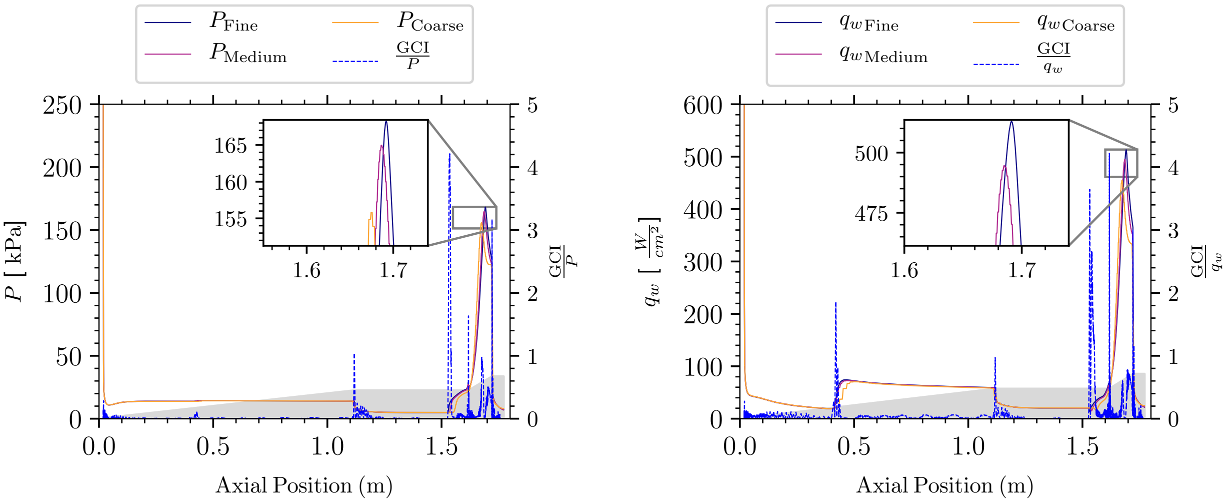

**(a)** Pressure

**(b)** Heat flux

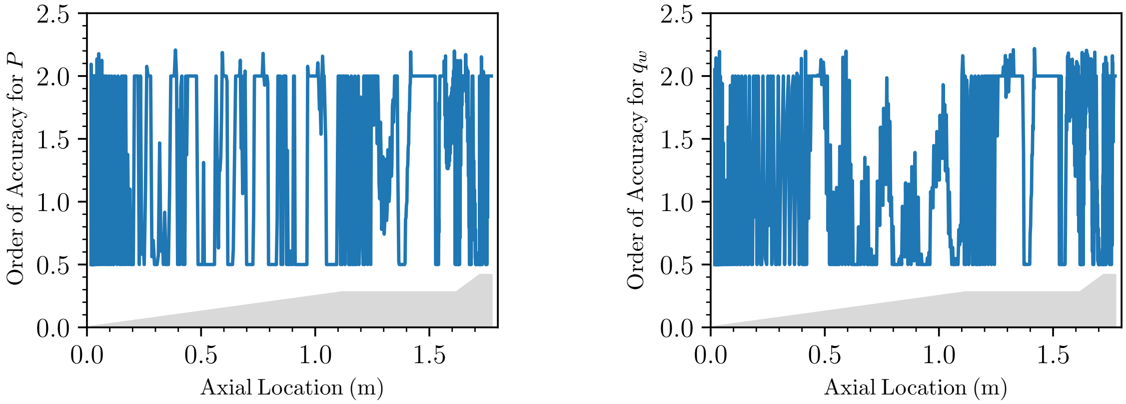

**(c)** Order of accuracy for pressure

**(d)** Order of accuracy for heat flux

**Figure 4-23.** GCI Calculation for RANS-SST simulation of Run 34.

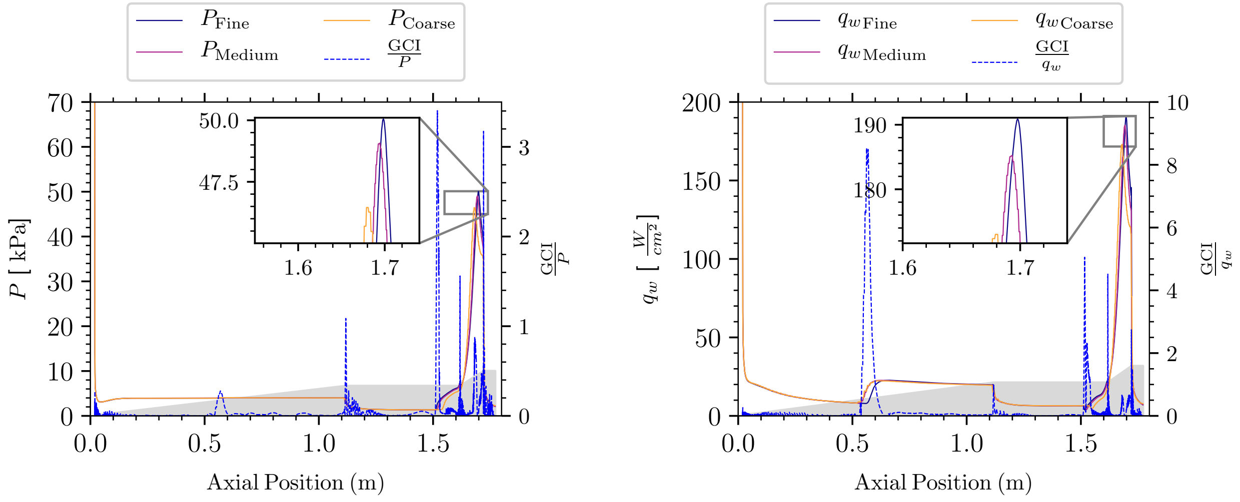

**(a)** Pressure

**(b)** Heat flux

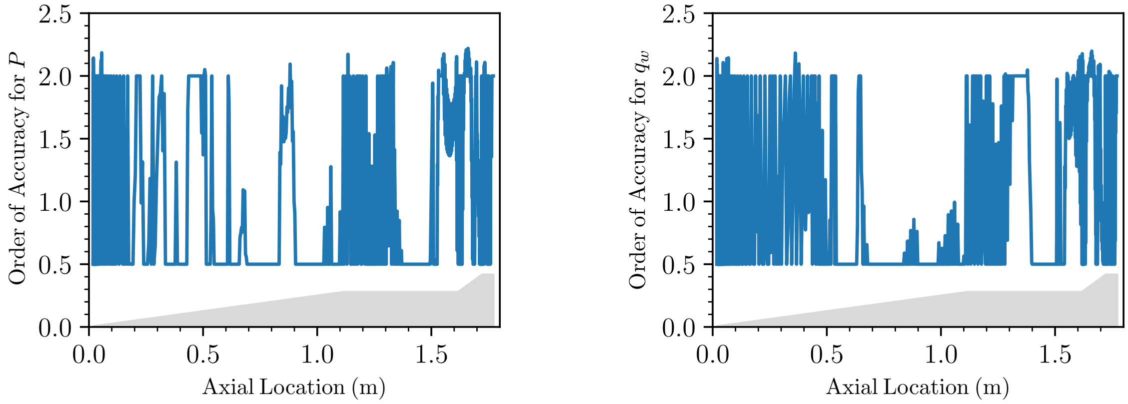

**(c)** Order of accuracy for pressure

**(d)** Order of accuracy for heat flux

**Figure 4-24.** GCI Calculation for RANS-SST simulation of Run 42.

Examining the results for the SA model, it can be noted that for the runs at 0° angle of attack, there are no/very small spikes in the pressure GCI until the flare region. Then, there are two spikes, one at the start of the flare, and one at the end of the flare, where the geometry becomes cylindrical again. For heat flux, the GCI spikes at the transition location and flare for Run 30, but only at the flare for Run 38. This is likely due to the larger flow speed and heat flux values present in Run 30, but could also be related to the fact that transition occurred in Run 38 due to a manual trip, which may be more easily predicted by the model. For the runs at nonzero angle of attack (Runs 34 and 42), the pressure GCI spikes at the cone-cylinder interface and flare, while the heat flux GCI spikes at the transition location, cone-cylinder interface, and flare. The additional spike in GCI relative to the runs at 0° angle of attack is interesting to note for Run 42 vs Run 38.

For the SST model, trends between runs are similar to those in the SA model results. However, the spike in heat flux GCI for Run 30 is also present for Run 38. In addition, small spikes in the pressure GCI appear for Runs 34 and 42, where spikes at this location only appear for the heat flux GCI in the SA model results.

## 4.3. Future Work

For future work, additional code verification should be performed for the MEIT and RANS equations to ensure the proper implementation of the models. Specifically, substantial work on MEIT code verification is planned for FY23. As in [1], numerical uncertainty is lowest for the RANS-SA model, but the order of accuracy is not maintained at a consistent value, and the GCI is significant in several areas. The high GCI value is an important result since these mid- and high-fidelity meshes were considered to be well refined before the analysis was completed. It was noted in [1] that future simulations should use additional mesh refinement. This is done in the current study despite the increased computational cost, and results in decreased numerical uncertainty in general. As expected, the low-fidelity MNA+FPBL model's numerical uncertainty is the lowest of all the simulation results, even with the incorrect factor of safety when the difference between $p_{\text{obs}}$ and $p_{\text{th}}$ is smaller than 10%. This is due to the simplistic nature of the model and the fact that reaching well inside of the asymptotic region is less computationally expensive. Additional work will be completed to address the degradation of $p_{\text{obs}}$. For the mid- and high-fidelity models, spikes in GCI remain large, and the numerical uncertainty for the Euler+MEIT and RANS-SST models specifically could be further examined. Spikes in GCI are typically at points where the body geometry makes it hard to predict flow accurately due to the sharp geometry and resulting flow features such as shock waves. Thus, a certain level of numerical uncertainty is expected, and the observed levels may not be significantly reducible. A potential approach to addressing regions of high numerical uncertainty is further local or global mesh refinement to ensure the solution is within the asymptotic region. In addition to local and global mesh refinement, the transition from laminar to turbulent solutions should be improved to ensure the transition is smooth. Without a smooth transition, this region is not able to enter the asymptotic range and will yield large numerical uncertainty.

# 5. VALIDATION

In the preceding sections, code verification and solution verification results are presented and discussed. These results provide evidence that the MFTK models solve the correct mathematical models and that the simulations evaluated are accurate for the intended use. Model validation is the process of asking to what degree a model represents physical phenomena for its intended uses [5], and involves the comparison of simulation results with experimental data. In this section, model validation theory is presented, followed by a selection of comparison results. These results are presented both in terms of QoI trends over the vehicle and in terms of errors with uncertainties. In this comparison, the varying accuracy of the models in MFTK is seen, and the effect of certain geometric features and physical phenomena are apparent in the results of each model.

## 5.1. Model Validation Theory

Though formally defined in the introduction, informally, model validation seeks to determine the degree to which the model is solving the physically appropriate equations. For high-speed aerodynamics, these would include compressible forms of the continuity, momentum, and energy equations. For the turbulent flows, including the full forms of the governing equations (as in direct numerical simulation) is often not tractable; therefore, closure models are frequently used (as in RANS). The inviscid treatment of certain flows is another example of a modeling assumption. Model validation processes can be used to determine the suitability of such modeling assumptions.

Comparing simulation predictions to experimental results is fundamental to model validation. There are several levels of scrutiny in comparisons that are seen in literature. A helpful comparison is found in Figure 12 of [14] that presents six levels of validation comparisons. The first and least descriptive is the viewgraph norm where contours are placed next to each other, but differences in values are often obscured from the wealth of field information and colorful scales. The next plots show several levels of comparisons that switch to a common set of axes that are much better at revealing direct information. Increasing the levels of UQ on measurements and predictions increases the rigor.

The ASME Standard for Verification and Validation in Computational Fluid Dynamics and Heat Transfer (ASME V&V 20) [5] goes beyond comparisons in plots to the calculation of validation comparison error and the validation uncertainty. In this standard, the validation comparison error $E$ is defined as

$$E = S - D, \tag{5.1}$$

where $S$ represents the simulation solution and $D$ represents the experimental data. Equation (5.1) provides the simplest validation metric, which nonetheless transitions from the qualitative comparisons in plots to a quantitative measure used to evaluate predictive accuracy. It can be used to reveal trends in model form error over space, time, or parameter sets.

The validation comparison error reveals differences, but how meaningful are those differences, and could experimental and/or modeling uncertainties explain them? To help answer these questions, ASME V&V 20 also includes the calculation of a validation uncertainty

$$U_{\mathrm{val}} = \sqrt{U_{\mathrm{num}}^2 + U_{\mathrm{input}}^2 + U_D^2}, \tag{5.2}$$

where $U_{\mathrm{num}}$ is the numerical uncertainty commonly assessed by grid convergence studies, $U_{\mathrm{input}}$ is the input parameter uncertainty propagated through the model, and $U_D$ is the experimental data uncertainty [5]. Equation (5.2) is in the form of a standard uncertainty at the $1\sigma$ or $2\sigma$ (68% or 95%, respectively) confidence level, depending on the confidence level of the uncertainty components. Here, $\sigma$ is the standard deviation. If the input and experimental uncertainties are at the $1\sigma$ confidence level, the numerical uncertainty can be converted to the $1\sigma$ confidence level by dividing the GCI by a expansion factor, as discussed in [5]. Throughout this work, input uncertainties are not quantified and experimental uncertainties are assumed to be at the 95% confidence level. Thus, the numerical uncertainty is taken to be equal to the GCI, and validation uncertainties are presented at the 95% confidence level. Uncertainties expanded to the 95% confidence level are capitalized by convention [5]. Thus, all uncertainties in the present study are described by capitalized variables. The validation uncertainty provides perspective on the validation error. For example, if $|E| \gg U_{\mathrm{val}}$, then model form error is discernible from the relatively small validation uncertainty and model improvements may be prudent if the errors are larger than desired. On the other hand, if $|E| \leq U_{\mathrm{val}}$, model form error is not distinguishable among the validation uncertainty and efforts to reduce uncertainty may be pertinent.

Note that $E$ is the validation comparison error and includes possible errors in measured data and simulation predictions. It is, therefore, not the model form error. The exact model form error is challenging to isolate but can be bounded. In ASME V&V 20 [5], the model form error is bounded by

$$\delta_{\mathrm{model}} \in [E - U_{\mathrm{val}}, E + U_{\mathrm{val}}]. \tag{5.3}$$

This bounding motivates efforts to minimize uncertainty in both experiments and simulations so that the model form error can be known with greater accuracy.

## 5.2. Validation Results

The validation studies herein include surface pressure and heat flux comparisons for all HIFiRE-1 experimental runs mentioned in Chapter 3 (30, 34, 38, 42). In addition to traditional comparison plots, the validation comparison error $E$ from (5.1) and validation uncertainty $U_{\mathrm{val}}$ from (5.2) are calculated and plotted to enable quantitative comparisons of predictive accuracy at all three fidelity levels of MFTK. Errors and uncertainties are shown for each run. Error and uncertainty are also shown for individual geometric sections, and for each meridional angle of the nonzero angle of attack runs. To explore the effect of parameter variation on error, the error is plotted for varying Reynolds number or angle of attack, with the other parameter fixed. Total error integrated over the body and averaged for all runs is also compared between models. The experimental data have known uncertainties [8]. Similarly, the solution-verification studies in Chapter 4 provide numerical uncertainty values $U_{\mathrm{num}}$. Note that for all of the simulation results herein, the fine mesh is used and iterative convergence is achieved by driving normalized residuals below $10^{-12}$ when possible, and below $2 \times 10^{-8}$ in all cases. For some of the more computationally intensive RANS cases, relaxing the residual tolerance to $10^{-9}$ or $10^{-8}$ enables convergence without significantly affecting QoIs or the order of accuracy. The parameter uncertainty $U_{\mathrm{input}}$ is not calculated in this work but recommended for future work.

### 5.2.1. *Surface Pressure Comparisons*

The first validation comparison is the surface pressure along the axial length of the vehicle as shown in Figures 5-1–5-4. The test vehicle geometry is shown with the second *y*-axis as a gray region to provide background to the drastically different behavior along the length. The results include measured data and predictions from the RANS-SA model, the RANS-SST model, the Euler+MEIT model, and the MNA+FPBL model. The experimental pressure uncertainty is 3% [8], interpreted as 3% of reading in the associated error bars/uncertainty bands. The simulations have numerical uncertainty from the GCI results from solution verification shown as shaded regions that are colored according to their respective model color. The data are taken from the 0° meridian (meridian with highest sensor density). The fore-cone has very few pressure sensors. However, this is acceptable, as the pressure is nearly constant in this region. The instrumentation density increases towards the rear of the vehicle where the flow is more complex. The pressures increase drastically on the 33° flare region. The predictions use meshes that are derived from the same source. From a 3D source mesh, a 2D axisymmetric mesh with 524,288 cells is derived for the RANS simulations. For the Euler+MEIT simulations, a 3D mesh is derived from the RANS 3D mesh with relaxed refinement in the boundary layer region (65M total cells), and from this 3D mesh, a 2D axisymmetric mesh is derived with a similarly resolved boundary layer for Euler+MEIT having 262,144 total cells. This results in Euler meshes which are more representative of typical meshes for this model, which does not model viscosity. Because the viscous boundary layer is not resolved by this model, it does not need a mesh with as fine of resolution near the wall. For the MNA+FPBL model, which only requires a surface mesh, the 3D surface is extracted from the RANS 3D source mesh.

These figures each include an inset plot that highlights the aft end of the cylindrical and the flare regions where the pressure measurements and predictions are quite complex. As noted in [1], the RANS predictions compare very well on the fore-cone and cylinder sections. It was mentioned in that report that the inviscid nature of the surface pressure in these sections played an important role in the accuracy of prediction. As noted in [15], RANS models have a known weakness in the prediction of turbulent flow through a shock/boundary layer interaction. Indeed, Maclean et al. noted in their computational work with the HIFiRE-1 data that their SST model suffered from

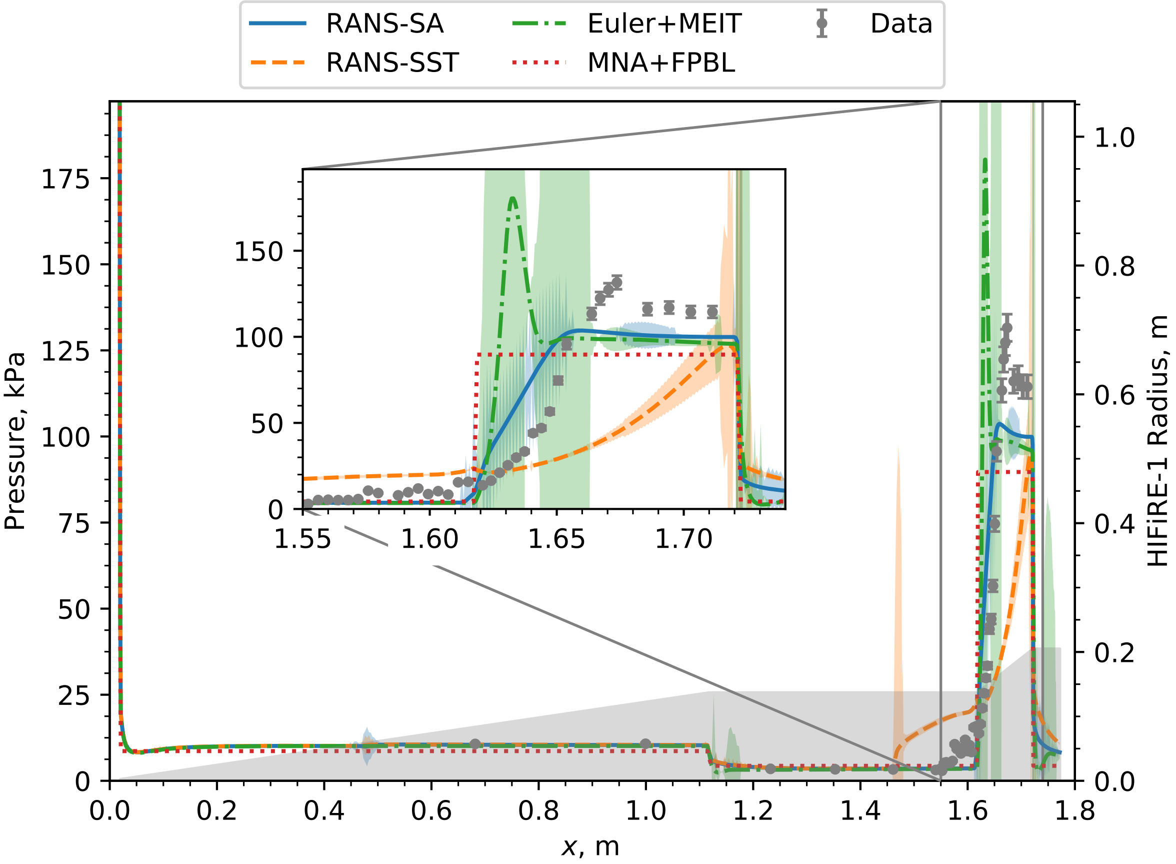

**Figure 5-1.** HIFiRE-1 wind tunnel test pressure data and predictions, Run 30.

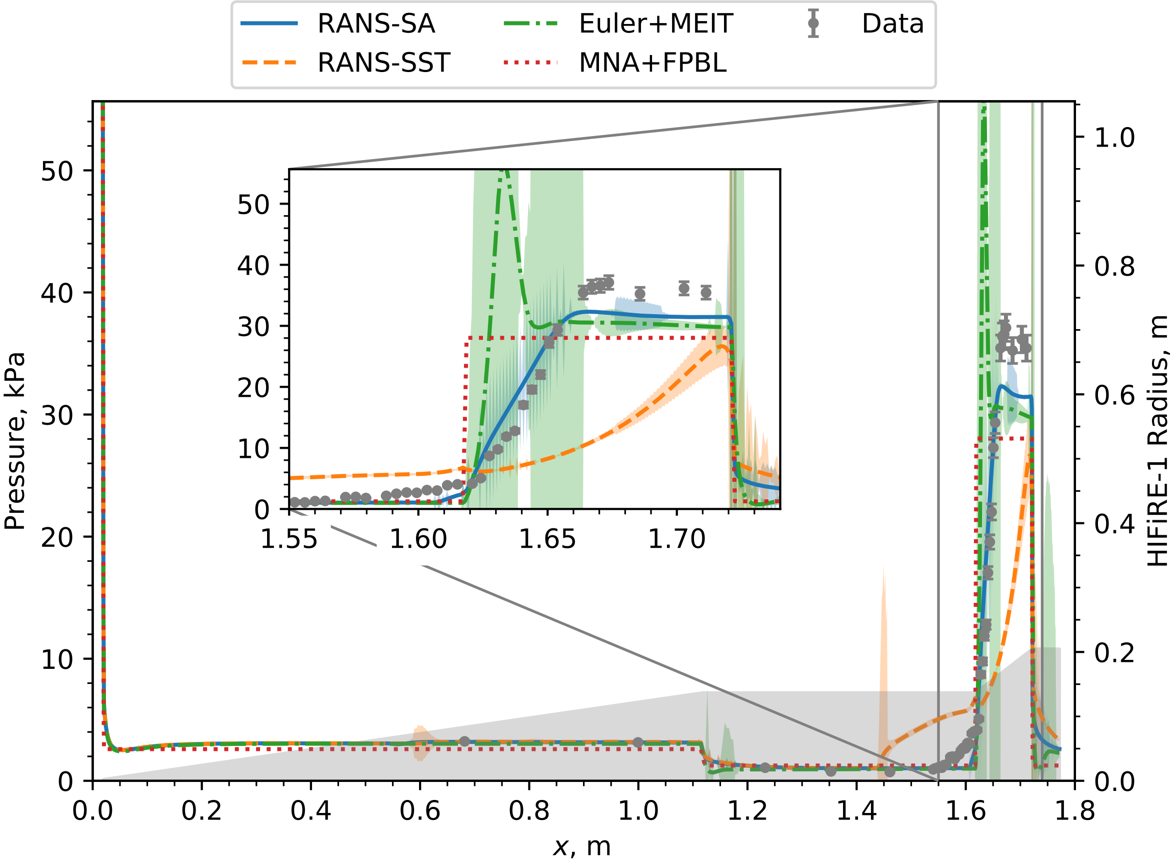

**Figure 5-2.** HIFiRE-1 wind tunnel test pressure data and predictions, Run 38.

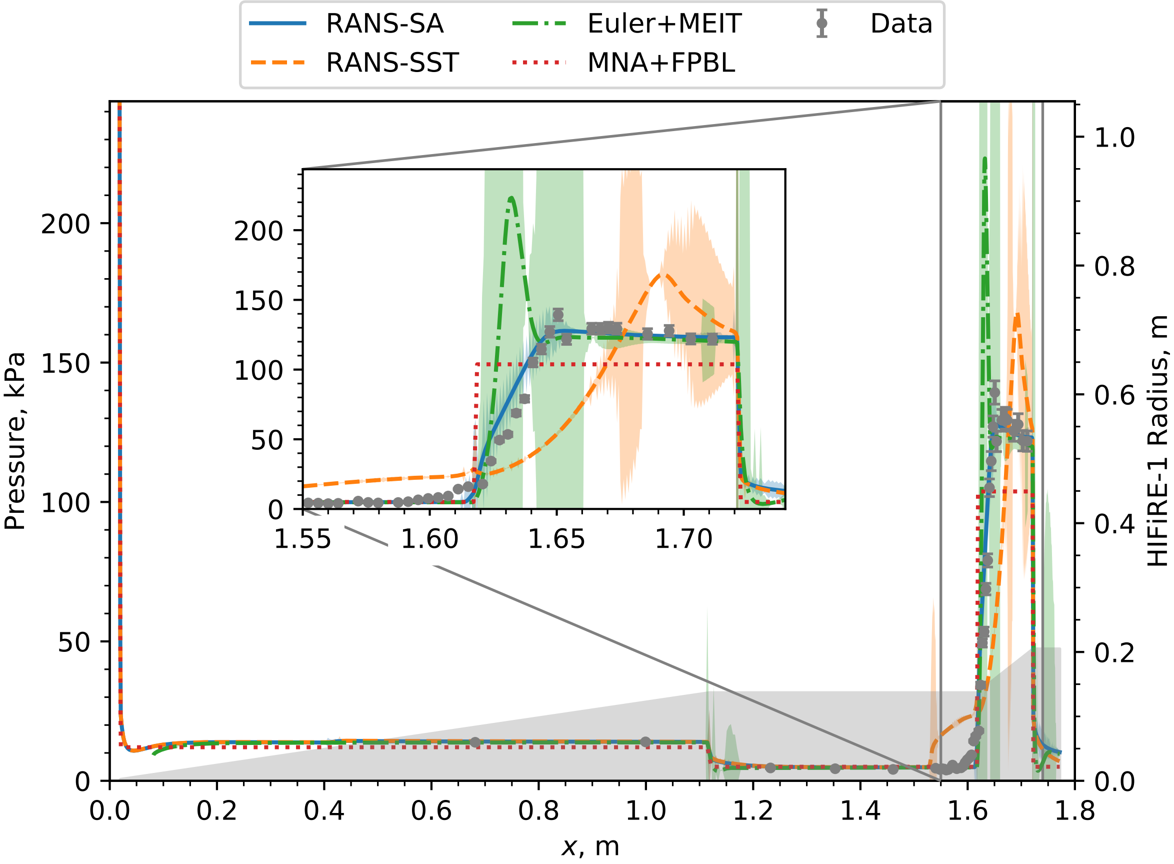

**Figure 5-3.** HIFiRE-1 wind tunnel test pressure data and predictions, Run 34.

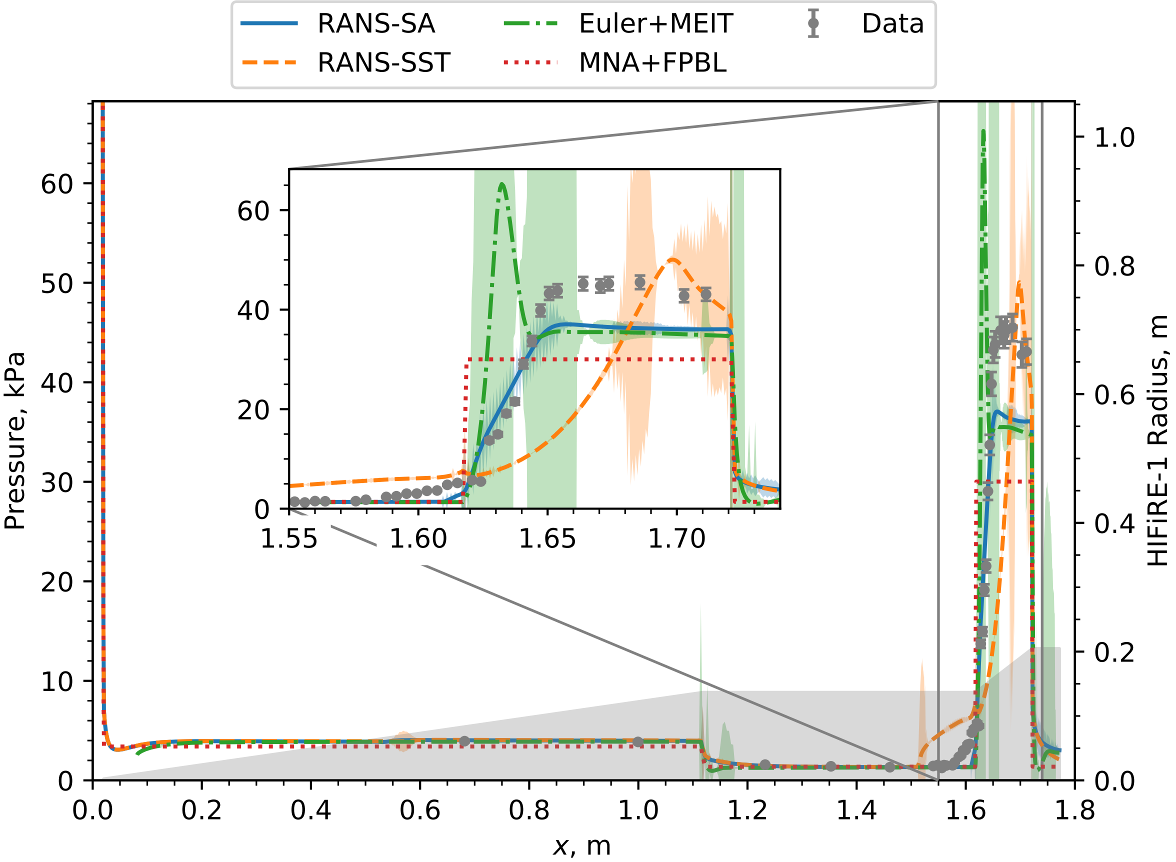

**Figure 5-4.** HIFiRE-1 wind tunnel test pressure data and predictions, Run 42.

a predicted increase in Reynolds shear stress caused by vorticity from the separation shock, and that this behavior was caused by an overly aggressive choice of stress limiting [10]. They tuned the eddy viscosity calculation in both the SST and SA models used, and achieved significantly better agreement with experimental results. Such tuning could prove useful in program-specific use cases of the SPARC RANS models, either in manual form for a specific geometry and set of flow conditions, or via an automated process.

Over the majority of the flare region, the SA model predicts the pressure significantly more accurately than the SST model. The over-prediction of pressure in this region is consistent with [10]. In general, the numerical uncertainty associated with the SA model is substantially lower than that of the SST model, indicating lower variation between results from the three mesh refinement levels. The SST model typically displays a spike in numerical uncertainty at 1.45 m as well, where separation is predicted to begin. For the runs at 0° angle of attack, the numerical uncertainty increases further inside of the flare region, and is largest at the maximum predicted pressure. For the runs at 2° angle of attack, there are two distinct regions of large numerical uncertainty, one before and one after the peak pressure value, which occurs where the separation region terminates and the shock impinges on the flare. Spatially rapid and quantitatively aggressive changes take place around this location, and the refinement of the mesh becomes more important. The SA model avoids this problem due to its prediction of a shock which does not impinge on the flare, and the accompanying relatively constant pressure prediction across the flare. This does make the SA model a more accurate choice for all flow features or QoIs, however, as it is known to fail in the prediction of the separation region seen experimentally [10]. It is important to note that while the 0° angle of attack cases show little difference between the peak pressure prediction on the flare for the SA and SST models, the 2° angle of attack cases show significantly higher values from the SST predictions, and indicate a specific spatial maximum. This sort of difference has the potential to impact design decisions. To provide a sense of the differences in pressures between runs, Figure 5-5 shows the RANS-SA predictions for each run. The pressure is clearly higher at the high Reynolds number runs (30 and 34) and there is a noticeable difference between predictions for 0° and 2° angles of attack.

The mid-fidelity Euler+MEIT and low-fidelity MNA+FPBL models of MFTK have not historically been the focus of validation work to the extent that the RANS models have. Though previous efforts to produce credibility evidence for these models have been carried out, the first known validation study employing a rigorous standardized process on them was performed in [1] . Both lower fidelity models predict pressure well on the fore-cone and cylinder, but are less accurate in the flare region. MNA+FPBL predictions are generally least accurate and not smooth, but show little numerical uncertainty as mentioned in Chapter 4. Pressure predictions in the flare region appear similar to a step function, and miss experimental values by a significant amount. A detailed discussion of the MNA+FPBL model's behavior and the causes of it is given in [1]. The Euler+MEIT model overpredicts the pressure gradient at the start of the flare and the maximum pressure for all runs, before reaching a relatively constant value close to the RANS-SA prediction for the rest of the flare. Spikes in numerical uncertainty occur at the cone/cylinder transition, and the largest numerical uncertainty of all models in the flare region. This uncertainty is largest at the start and end of the flare. Overall, the Euler+MEIT numerical uncertainty indicates that the model is not mesh-converged. More quantitative error and uncertainty comparisons are given later in this section.

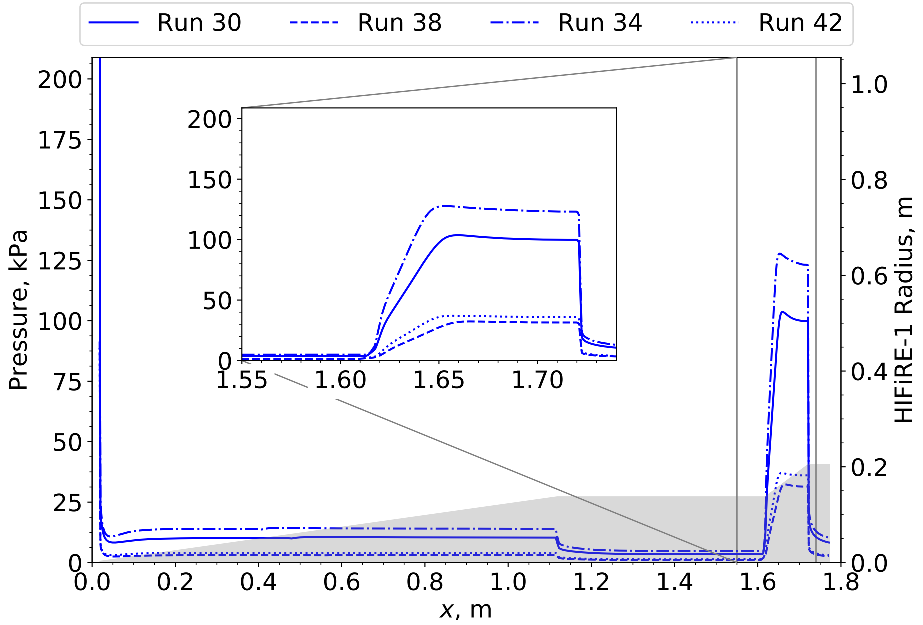

**Figure 5-5.** Comparison of pressure predictions from RANS-SA models for all analyzed runs at 0° meridional angle.

In Figures 5-6–5-9, the relative error for each model on the four runs is shown, together with the total relative validation uncertainty, $U_{\text{val}}$. This error is computed using (5.1) and normalized by the experimental data. The validation uncertainty is computed using (5.2), and is normalized by the QoI (in the plots below, pressure). The error is low on the fore-cone and cylinder, and rises to large values in the flare region. However, each model has significant relative errors before the flare is reached, which is not immediately apparent from the pressure plots above. A comparison with the equivalent plot from [1] shows reduced validation uncertainty in general for the RANS-SST and Euler+MEIT predictions, and higher validation uncertainty for the RANS-SA prediction. These changes in validation uncertainty are likely due to the increased refinement of the nominal mesh, and accompanying use of the GCI metric on the finer two meshes rather than the coarser two.

As noted in [1], error was generally discernible due to reasonably low validation uncertainty for the MNA+FPBL and RANS-SA models. This trend continues in the present study, for all runs. There is a noticeable validation uncertainty present for the RANS-SA model in contrast to the results in [1], but in general, the error is discernible. The Euler+MEIT validation uncertainty is still too large in the flare region for error to be discernible, and the same is true for the RANS-SST results in some cases (notably parts of the Run 30 and Run 34 results). However, the validation uncertainty is reduced to such an extent for the lower Reynolds number runs that error becomes distinct. This is an improvement and shows the value of mesh refinement studies.

The study described in this report seeks to draw conclusions regarding the accuracy of each model in MFTK on the four runs examined. Such conclusions regarding the accuracy of each model for a given run and of a given model across runs are difficult to make from the above plots. In addition, the change in accuracy of each model due to a given change in parameter (Re or angle of attack),

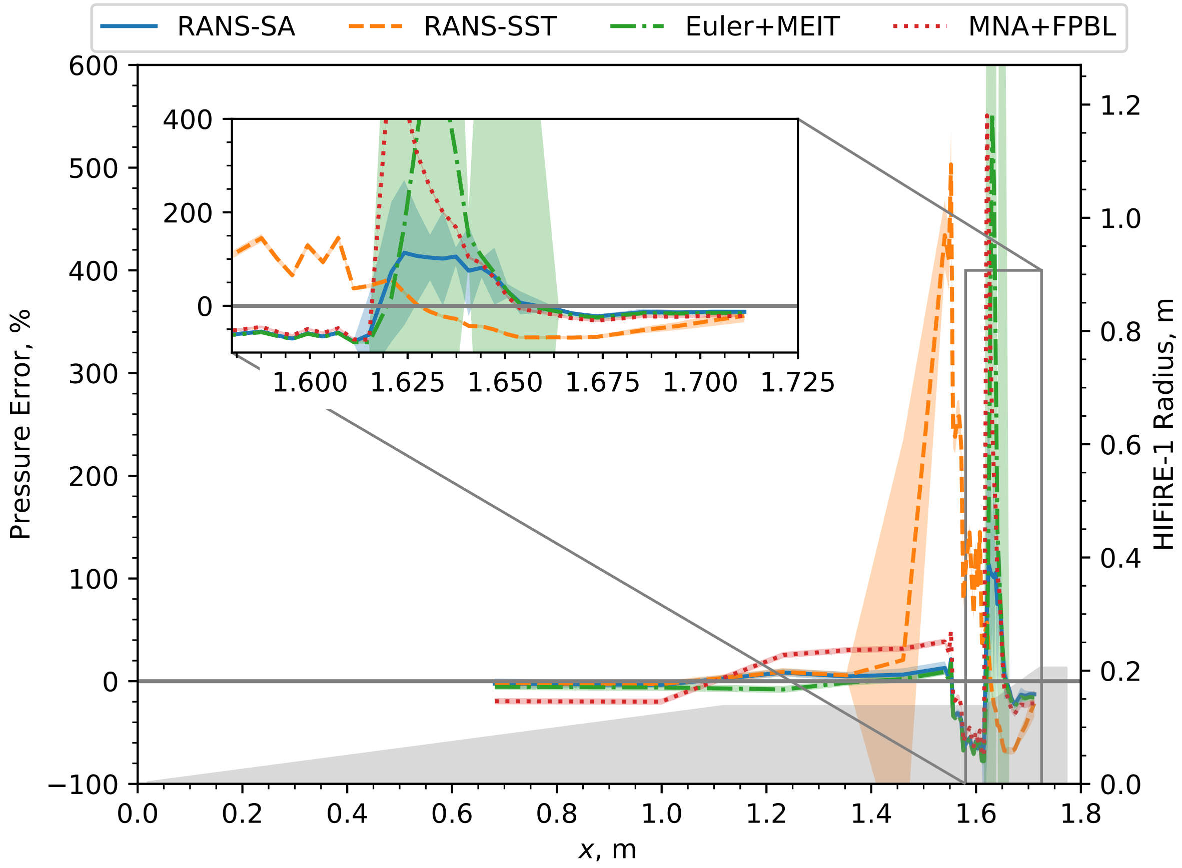

**Figure 5-6.** HIFiRE-1 pressure prediction error with uncertainty for Run 30.

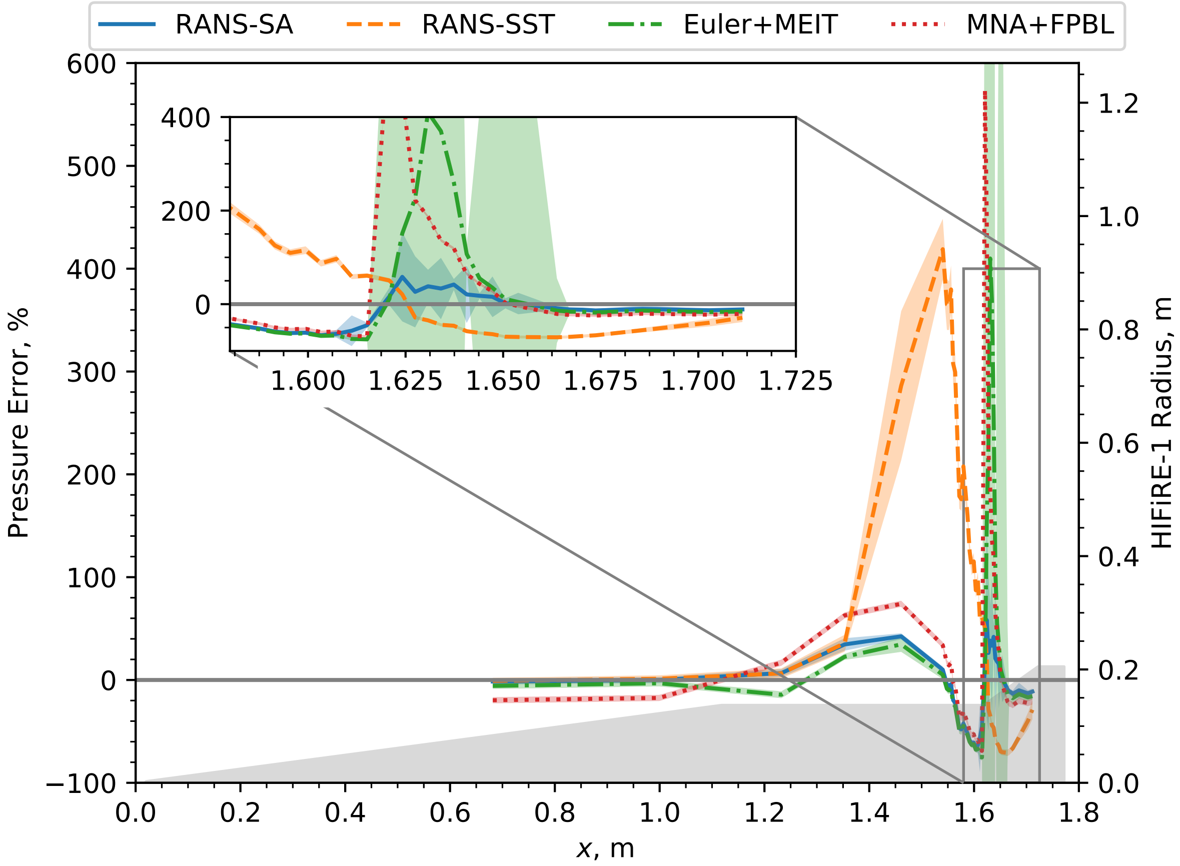

**Figure 5-7.** HIFiRE-1 pressure prediction error with uncertainty for Run 38.

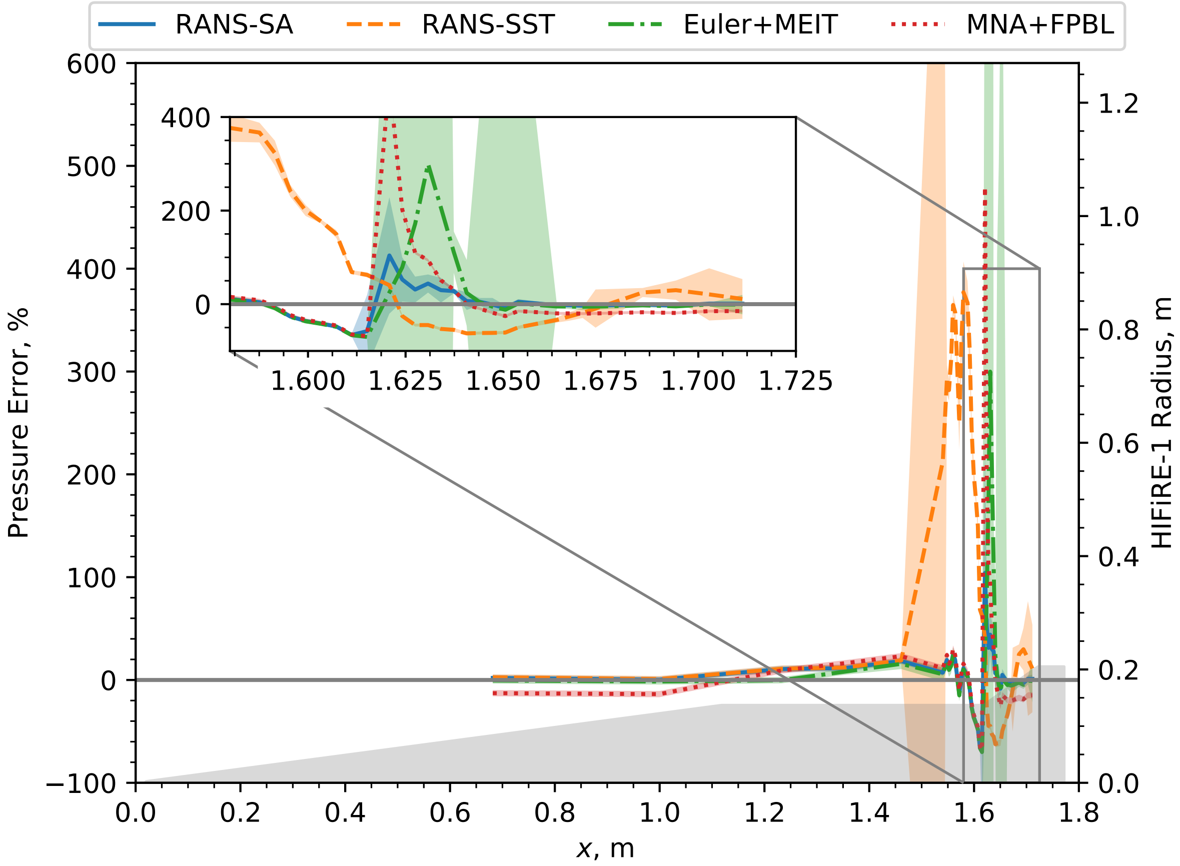

**Figure 5-8.** HIFiRE-1 pressure prediction error with uncertainty for Run 34.

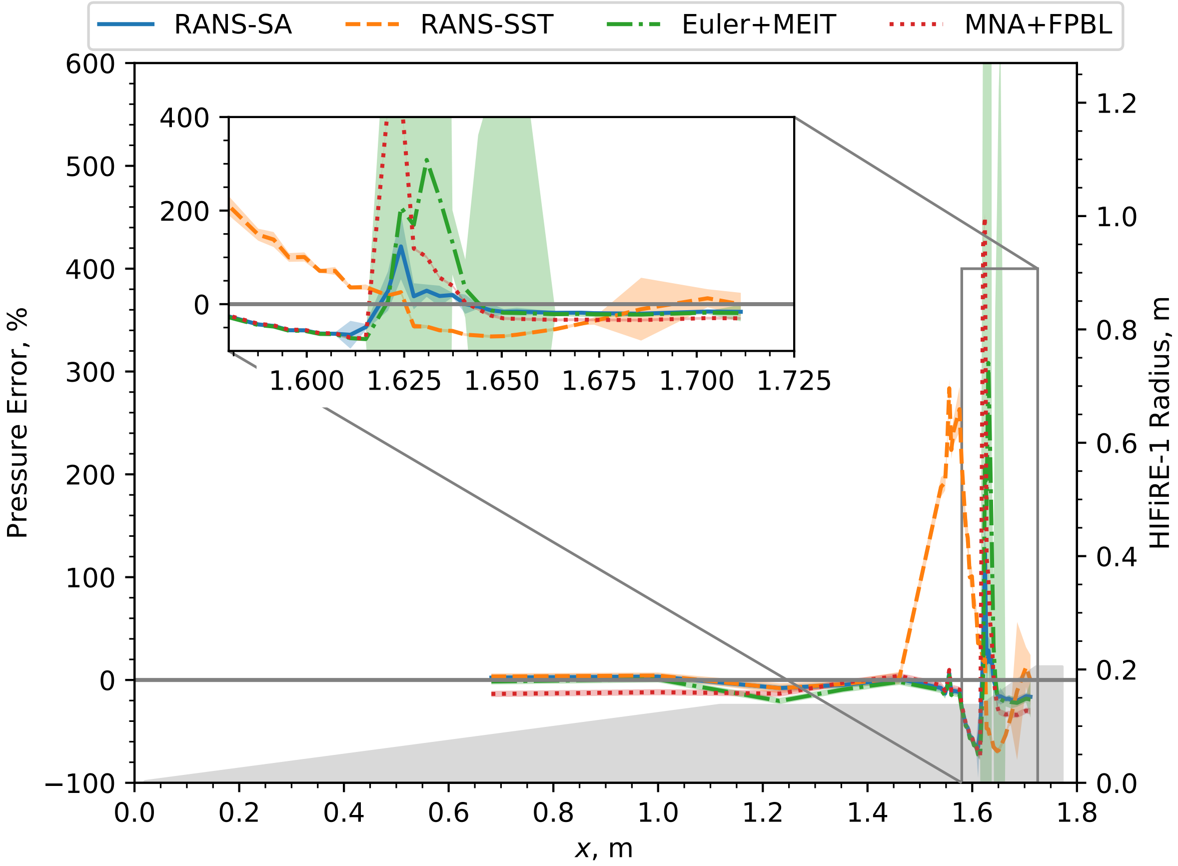

**Figure 5-9.** HIFiRE-1 pressure prediction error with uncertainty for Run 42.

is difficult to ascertain from the above plots. Thus, as in [1], bar charts of error with uncertainty are given.

First, the average accuracy of each model across all runs is examined. The relative error is integrated over the vehicle in the axial direction at each meridional angle, and these integrated errors are then averaged. Finally, the average from the four runs is taken for each model. The result is shown along with average validation uncertainty in Figure 5-10. This provides a graphical illustration of the concept of multiple fidelities in MFTK, by clearly showing that in the most comprehensive and general sense, the RANS models provide the lowest error, followed by Euler+MEIT, and finally MNA+FPBL. It also shows two important caveats to this generalization, namely that high-fidelity models such as RANS-SST can struggle to predict flow in certain scenarios and can result in higher error than lower fidelity models. Specifically, this can occur when the simulated flow contains features which are challenging to accurately predict, such as transition and separation. The validation uncertainty of the Euler+MEIT predictions is large enough to prevent the error from being discernible, which is a concern that should be addressed in future work and accommodated for in current usage of the model.

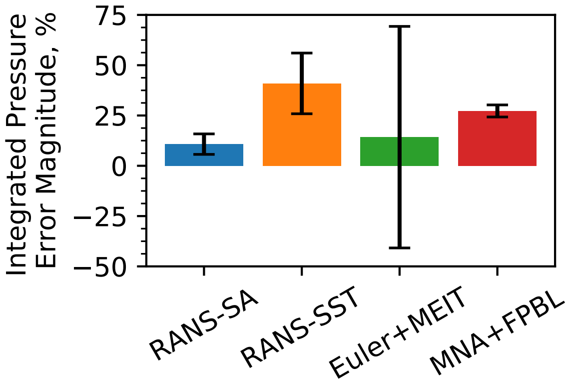

**Figure 5-10.** Relative error averaged across runs.

In Figure 5-11, relative error integrated over the vehicle at the 0° meridional angle is shown with integrated validation uncertainty. It is apparent from these plots that the error is largest in all cases for the RANS-SST model, followed by that of the MNA+FPBL model. Generally, the Euler+MEIT model shows the 3rd largest error, and the RANS-SA error is smallest, although this trend is reversed for Run 34. Validation uncertainty is largest for the Euler+MEIT model, and is also large for RANS-SST, except for Run 42. The smallest validation uncertainty is associated with the MNA+FPBL model.

The plots in Figure 5-11 give a direct comparison between results for each run at the 0° meridional angle. To examine model performance over the entire vehicle, the consolidation of error and uncertainty data is taken to the next level by computing a weighted average of the integrated results from the 0°, 90°, and 180° meridional angles. The 270° meridional angle is not considered, as it is not a unique angle, but should be identical to the 90° meridional angle due to flowfield symmetry, and would bias the weighted average toward the errors on the sides of the vehicle. Figure 5-12 shows the resulting composite error and validation uncertainty for each run. For Run

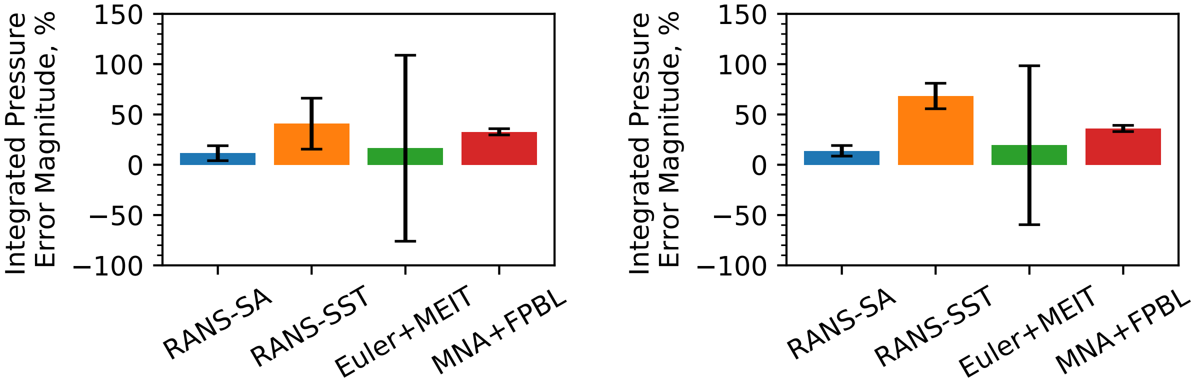

**(a)** Run 30 **(b)** Run 38

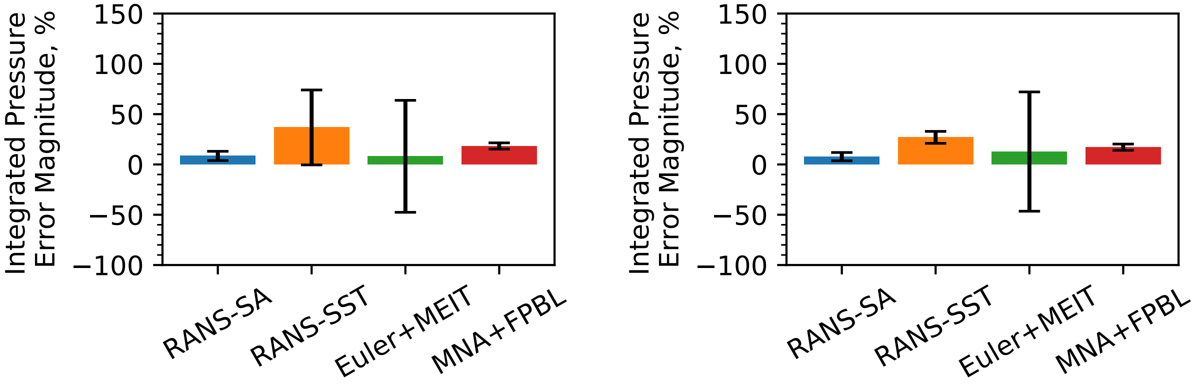

**(c)** Run 34 **(d)** Run 42

**Figure 5-11.** Relative error and validation uncertainty, integrated over all axial locations at the 0° meridional angle.

34, inclusion of the nonzero meridional angles results in increased error for all models except RANS-SST. However, for Run 42, error decreases with inclusion of the nonzero meridional angles for all models except MNA+FPBL. Indeed, comparing the composite errors for each model at each meridional angle does not show clear trends across models. The RANS-SST model has the highest error at the 0° meridional angle for both runs, and the MNA+FPBL model has the highest error at the 180° meridional angle for both runs. The other models do not show consistent trends with meridional angle.

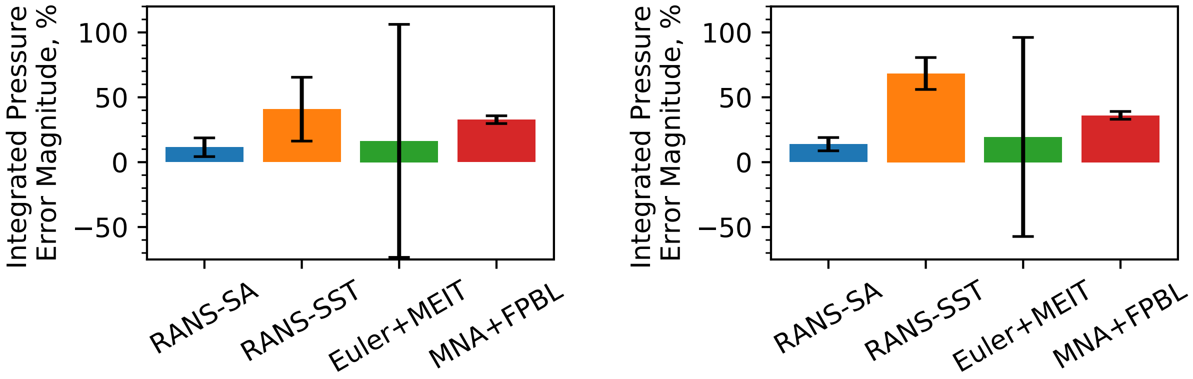

**(a)** Run 30

**(b)** Run 38

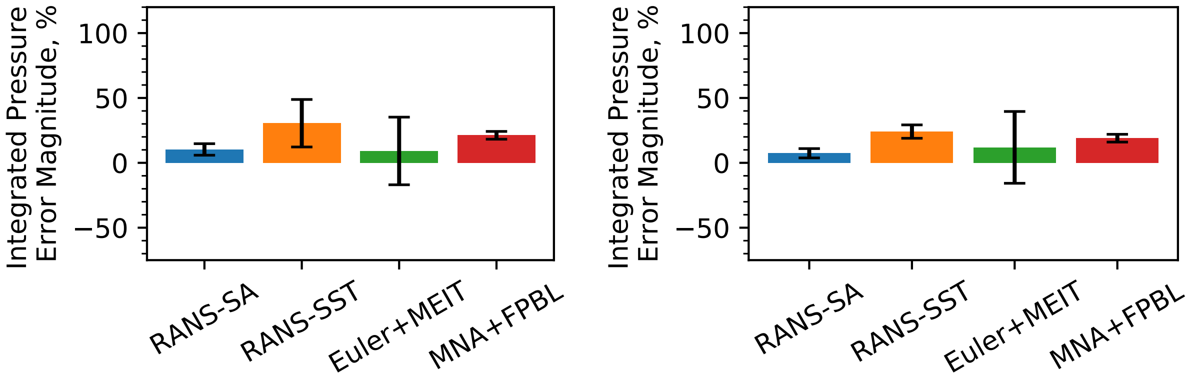

**(c)** Run 34

**(d)** Run 42

**Figure 5-12.** Relative error and validation uncertainty, integrated over vehicle and averaged over all meridional angles.

Though overall errors as shown in Figure 5-12 are valuable to examine for the sake of making conclusions about model accuracy in general over the entire vehicle, each model is affected by the flow geometry. Thus, it is useful to examine each geometric section of the HIFiRE-1 vehicle independently, to draw conclusions regarding model performance on each section. Figure 5-13 shows integrated error and validation uncertainty for each model on each section, at the 0° meridional angle. There are no pressure sensors with reported experimental data on the laminar cone, so no information is plotted for this section. It is apparent that for all runs, pressure error is generally lowest on the turbulent cone, and highest on the flare. This follows the trends seen in

Figures 5-6– 5-9. Notable anomalies include the high error in the RANS-SST predictions on the cylinder, which correspond to the large error in the region just before the flare, where the RANS-SST model predicts the early onset of flow separation. In addition, RANS-SA has higher error on the cylinder than on the flare for Runs 38 and 34. RANS-SA maintains a roughly 40% or lower error (generally below 20%) on all geometric sections, which is relatively impressive. By contrast, RANS-SST, Euler+MEIT, and MNA+FPBL all reach significantly higher errors on the cylinder or flare. Validation uncertainty is high for RANS-SST on the cylinder, and for Euler+MEIT on the cylinder and flare. Also of note is that error for Run 34, which can be thought of as the most difficult run to predict due to its high Reynolds number and nonzero angle of attack, does not show significantly higher errors than the other runs, and often exhibits lower errors.

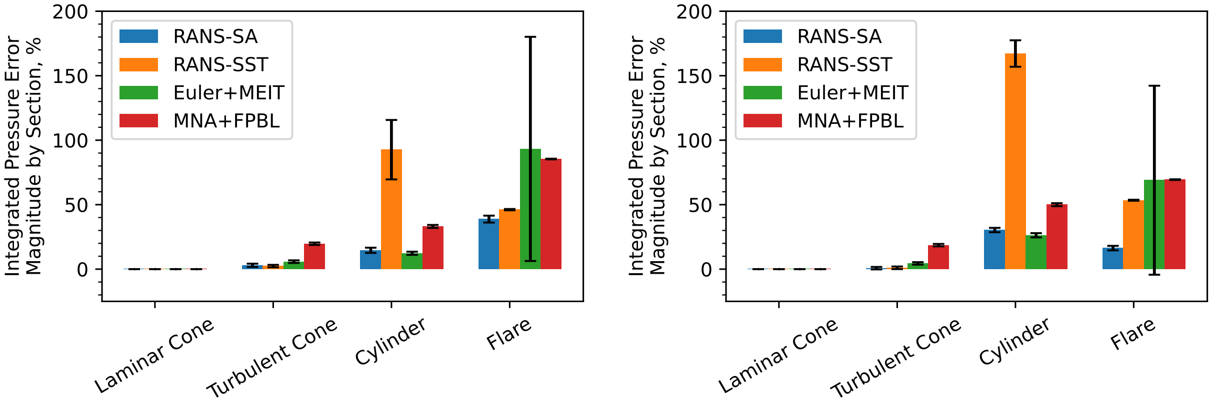

**(a)** Run 30

**(b)** Run 38

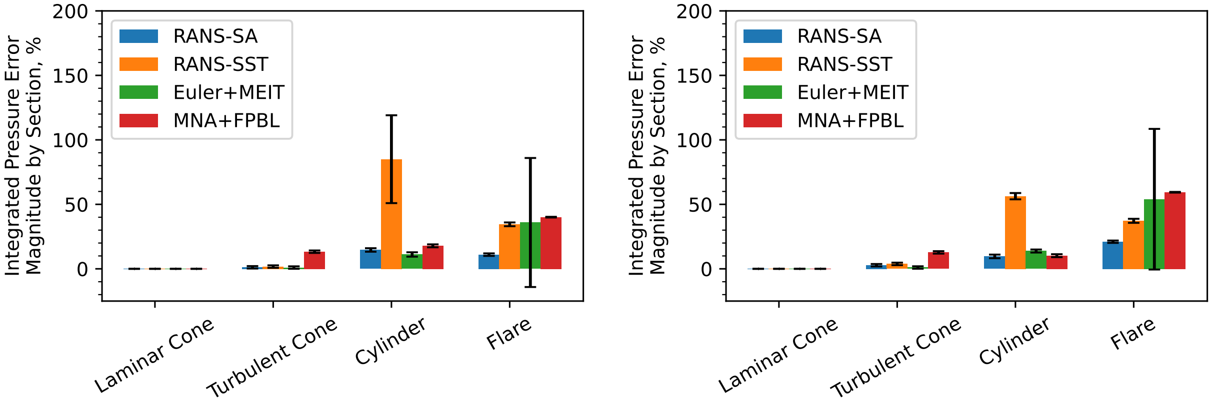

**(c)** Run 34

**(d)** Run 42

**Figure 5-13.** Relative error and validation uncertainty, integrated over vehicle at 0° meridional angle.

In Figure 5-14, section-specific integrated error and validation uncertainty values are shown for the 180° meridional angle, for Runs 34 and 42. Errors are not shown for the laminar cone or flare, or for the 90° meridional angle, due to the scarcity of pressure sensors at these locations. Errors are similar on the cylinder for both runs, but significantly larger on the turbulent cone for Run 34. Interestingly, RANS errors are highest on this section for Run 34. RANS-SST and MNA+FPBL errors are the highest errors on the cylinder. Errors are higher for Run 34 on the turbulent cone at the 180° meridional angle than at the 0° meridional angle. The MNA+FPBL model also shows significantly higher error on the cylinder at the 180° meridional angle than at the 0° meridional angle.

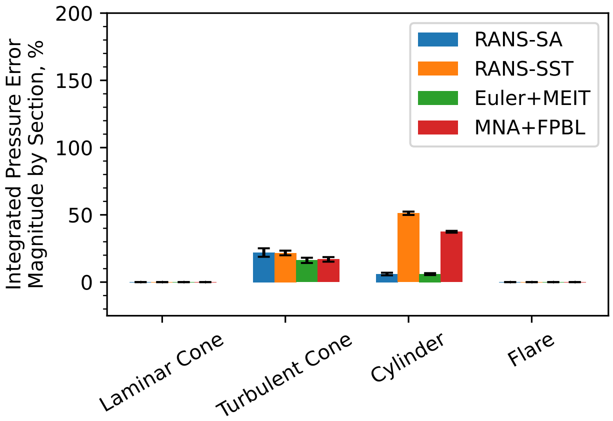

**(a)** Run 34, 180° meridional angle

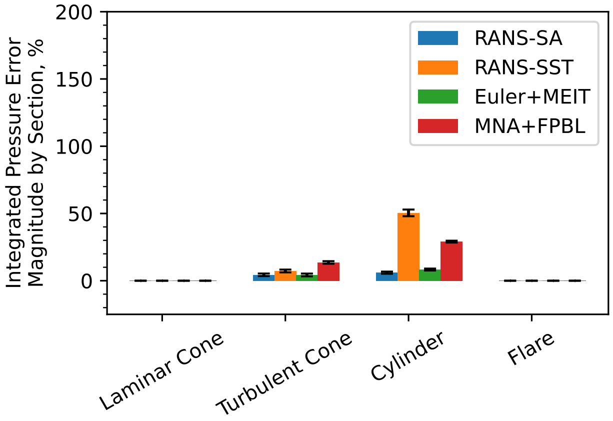

**(b)** Run 42, 180° meridional angle

**Figure 5-14.** Relative error and validation uncertainty, integrated over vehicle at 90° and 180° meridional angles.

Because conical geometry can be of particular interest in hypersonic applications, the integrated errors over the turbulent cone are shown separately with a smaller y-range, allowing for a better view of the error magnitudes from each model. These plots are shown in Figures 5-15 and 5-16. At the 0° meridional angle, the RANS errors are small compared to the MNA+FPBL errors, and are smaller than the Euler+MEIT error when the angle of attack is 0° (Runs 30 and 38). However, they are larger than the Euler+MEIT error when the angle of attack is 2° (Runs 34 and 42). A similar trend is seen for Run 42 in Figure 5-16, but for Run 34, the RANS errors are greater than both Euler+MEIT and MNA+FPBL errors. This indicates that at the 180° meridional angle (leeward side), the RANS models struggle, especially for higher Reynolds numbers. The Euler+MEIT model does as well. Note that due to lack of instrumentation on the vehicle at this meridional angle (two pressure sensors on turbulent cone), and the fact that the sensors were near the cone-cylinder transition, the results should be taken with caution. Thus, the more robust conclusion is that the RANS models appear to struggle near geometric transitions on the leeward side of such hypersonic vehicles at nonzero angles of attack, especially for higher Reynolds numbers.

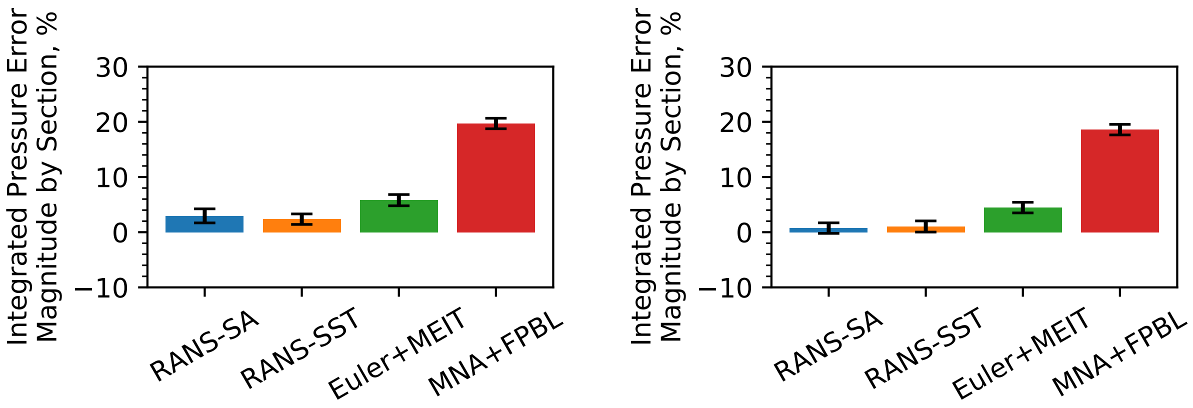

**(a)** Run 30

**(b)** Run 38

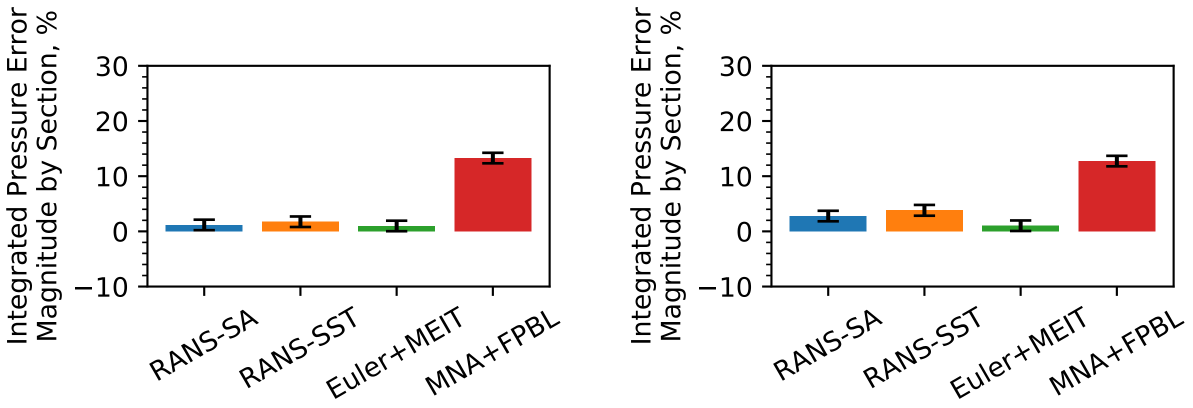

**(c)** Run 34

**(d)** Run 42

**Figure 5-15.** Relative error and validation uncertainty, integrated over turbulent cone section of vehicle, at 0° meridional angle.

In order to isolate the effect of varying the two primary test parameters in Figure 3-2, error plots are also made which show integrated relative error, averaged over meridional angles, with one parameter approximately constant and another varied. In Figure 5-17, integrated relative error and validation uncertainty are shown for fixed Reynolds number with the angle of attack varied. Error is seen to decrease for every model when the angle of attack is 2° rather than 0°.

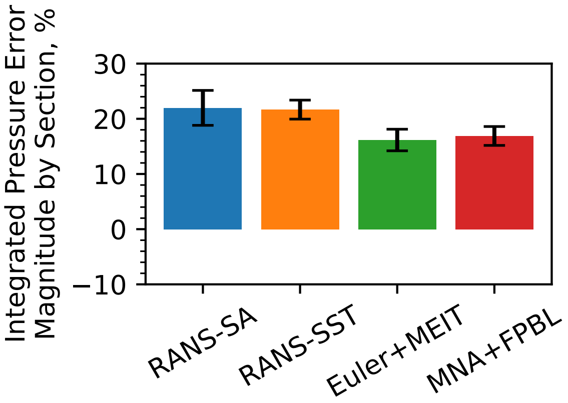

**(a)** Run 34, 180° meridional angle

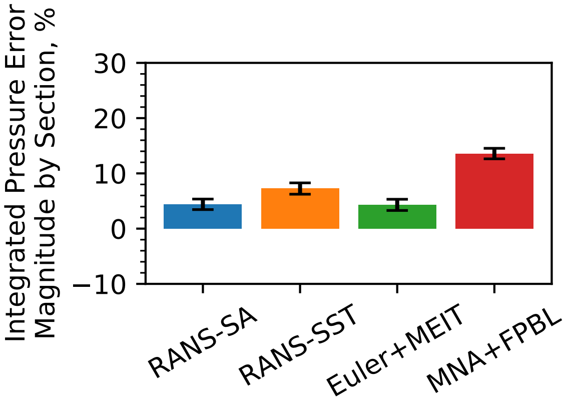

**(b)** Run 42, 180° meridional angle

**Figure 5-16.** Relative error and validation uncertainty, integrated over turbulent cone section of vehicle, at 90° and 180° meridional angles.

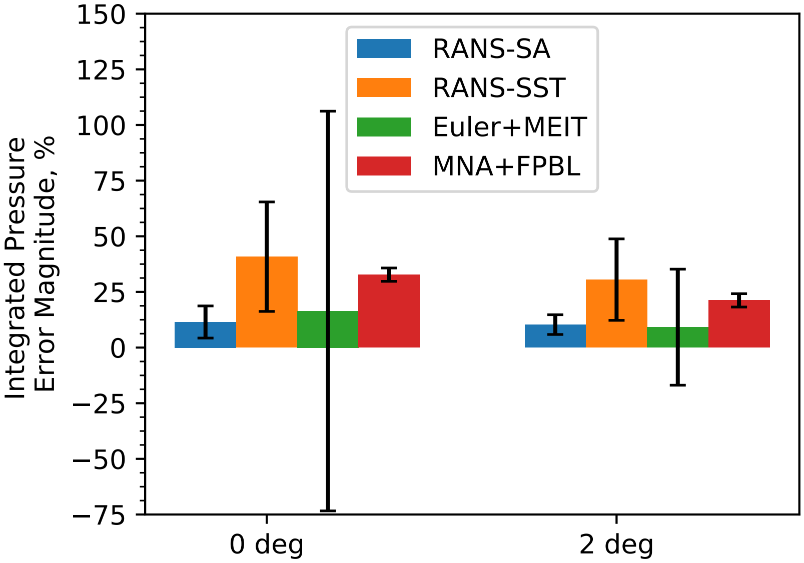

**(a)** Relative error for Runs 30 and 34 (high Re), with varied angle of attack.

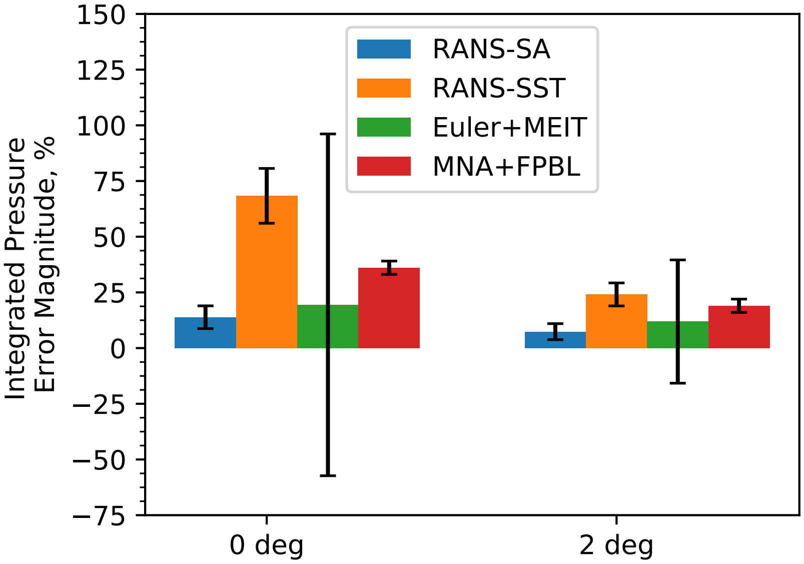

**(b)** Relative error for Runs 38 and 42 (low Re), with varied angle of attack.

**Figure 5-17.** Relative error with fixed Re, varied angle of attack.

In Figure 5-18, integrated relative error and validation uncertainty are shown for fixed angle of attack with the Reynolds number varied. Error decreases for higher Reynolds number for Euler+MEIT in both plots, and for both RANS models in Figure 5-18a. This could be related to the fact that higher Reynolds number corresponds to a reduced separation region size, which could improve agreement between the RANS predictions and experimental results. However, error increases with increasing Reynolds number for the nonzero angle of attack runs, so the model performance with varying Reynolds number should be studied further to obtain a more clear answer.

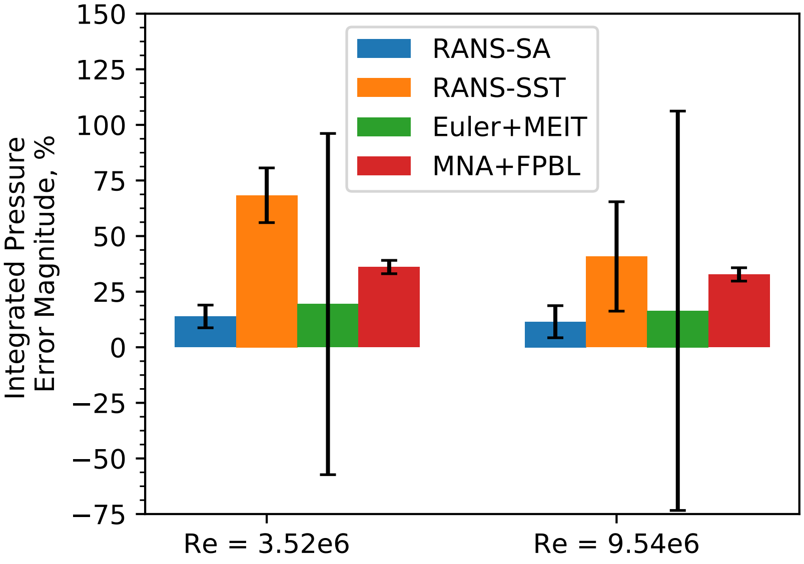

**(a)** Relative error for Runs 38 and 30 (0° angle of attack), with varied Reynolds number.

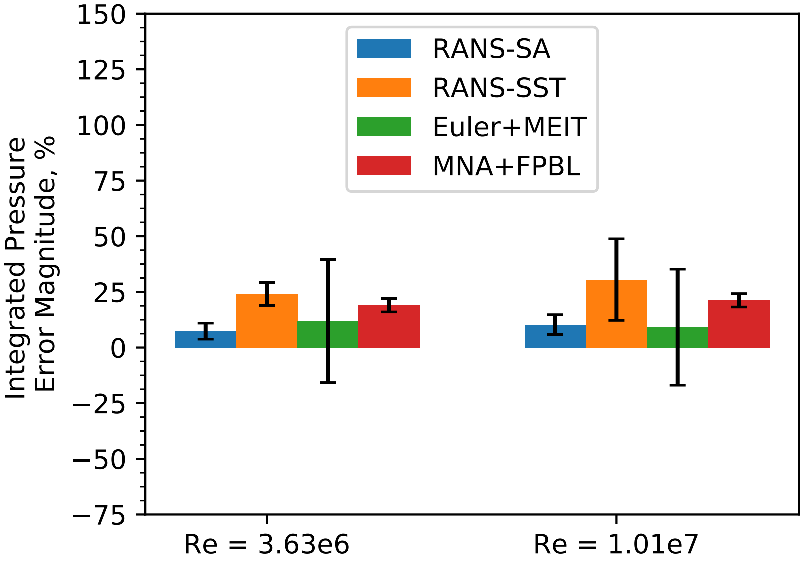

**(b)** Relative error for Runs 42 and 34 (2° angle of attack), with varied Reynolds number.

**Figure 5-18.** Relative error with fixed angle of attack, varied Reynolds number.

### 5.2.2. Surface Heat Flux Comparisons

The surface heat flux along the axial length of the vehicle is shown in Figures 5-19–5-22. The test vehicle geometry is, again, shown with the second $y$-axis as a gray region to provide context for the varying behavior along the length. The results include measured data and predictions from the four models described in the preceding section. The experimental heat flux uncertainty is 5% [8], interpreted as 5% of the reading in the associated error bars/uncertainty bands. The simulations have numerical uncertainty from the GCI results from solution verification shown as shaded regions that are colored according to their respective model color. As with surface pressure, the data are taken from the 0° meridian that has the most sensors. The fore-cone has significantly more heat flux sensors than pressure sensors. On the cylinder, there are also more heat flux sensors, and there are equal numbers of heat flux and pressure sensors on the flare.

The previous report on MFTK validation activities [1] mentions several key phenomena in the Run 30 results. Though the results in the present report are from simulations on fine (1L) meshes, whereas results in [1] were from simulations on medium (2L) meshes, these observations hold true for the current Run 30 results, and are in general common to all runs. One important difference is the reduced numerical uncertainty in the 1L mesh predictions as shown by smaller bands surrounding simulation results. This is a general trend, with numerical uncertainty still having spikes at the laminar-turbulent transition location, the cone/cylinder intersection, and on the flare. As noted in [1], the transition from laminar to turbulent flow on the cone is apparent. This is true for all runs, though the onset of transition diverges significantly from model to model for the low Reynolds number runs (Runs 38 and 42). These runs had the flow manually tripped at $x = 0.505$ m, which resulted in a large spike in measured heat flux, followed by a normal transition trend. The transition is turned on in the computational models in the same way for all runs, so different behavior at transition does not arise from trip type. However, the lower Reynolds number appears to allow some models (notably RANS-SST) the opportunity to predict more slowly transitioning flow which more closely matches these experimental trends. For Runs 30 and 34, simulation predictions show a much steeper increase in heat flux at the transition location than the experimental data display. The RANS-SST trend is more reasonable for Runs 38 and 42, with the Run 42 prediction showing good agreement. Euler+MEIT and MNA+FPBL show very sharp increases in predicted heat flux at the transition location, as there is no mechanism in these models for predicting transitional heating or for blending laminar and turbulent heating. Following transition, the MNA+FPBL curve proceeds to take the form of a nearly horizontal line to the cone/cylinder interface and the Euler+MEIT results overshoot the experimental trend in this region before decreasing to a similar value. The Euler+MEIT model predicts a similar overshoot at the flare before decreasing to approximate the experimental values reasonably well. Indeed, this model performs on par with the RANS models in the flare region, notably for Run 34. Heat flux is generally underpredicted by a substantial amount in the cone and flare regions by the MNA+FPBL model.

The RANS-SA model predicts heat flux trends associated with earlier transition than the RANS-SST predictions for all runs except for Run 30. Though the transition location is manually set, the model's formulation results in prediction of a more rapid transition. It also exhibits a relatively slow increase to a value lower than the experimental data on the flare. This is likely due in part to the fact that the SA model generally predicted no separation region, so the high-speed flow did not impinge on the flare after the cylinder/flare interface. The RANS-SST model predicts a slower rate of increase of heat flux in the flare region than the experimental data as well, but does not flatten out. This behavior is due to the low heating in the overpredicted separation region. Rather, for the 0° angle of attack runs, it increases to a maximum value higher than the experimental value at that point and roughly equal to the maximum experimental value. For Runs 34 and 42, it predicts an increase in heat flux to approximately $x = 1.69$ m and a decrease from there to a value significantly higher than the experimental value. The experimental data peaks around $x = 1.67$ m for the 0° angle of attack runs and around $x = 1.65$ m for the 2° angle of attack cases. This is related to the decreased separation region size, with the peak likely coming from impingement of the high-speed flow on the flare at the end of the separation region. Because the separation region terminates earlier on the windward side for the RANS-SST results at nonzero angle of attack, the predicted heat flux peaks earlier as well. As noted for surface pressure, the difference between the location and value of the maximum predicted by the SA and SST models would be critical for design decisions in any analysis which used these models to predict these QoIs in a similar context. Awareness of the models' tendencies and possible improvement through tuning of eddy viscosity are important to consider.

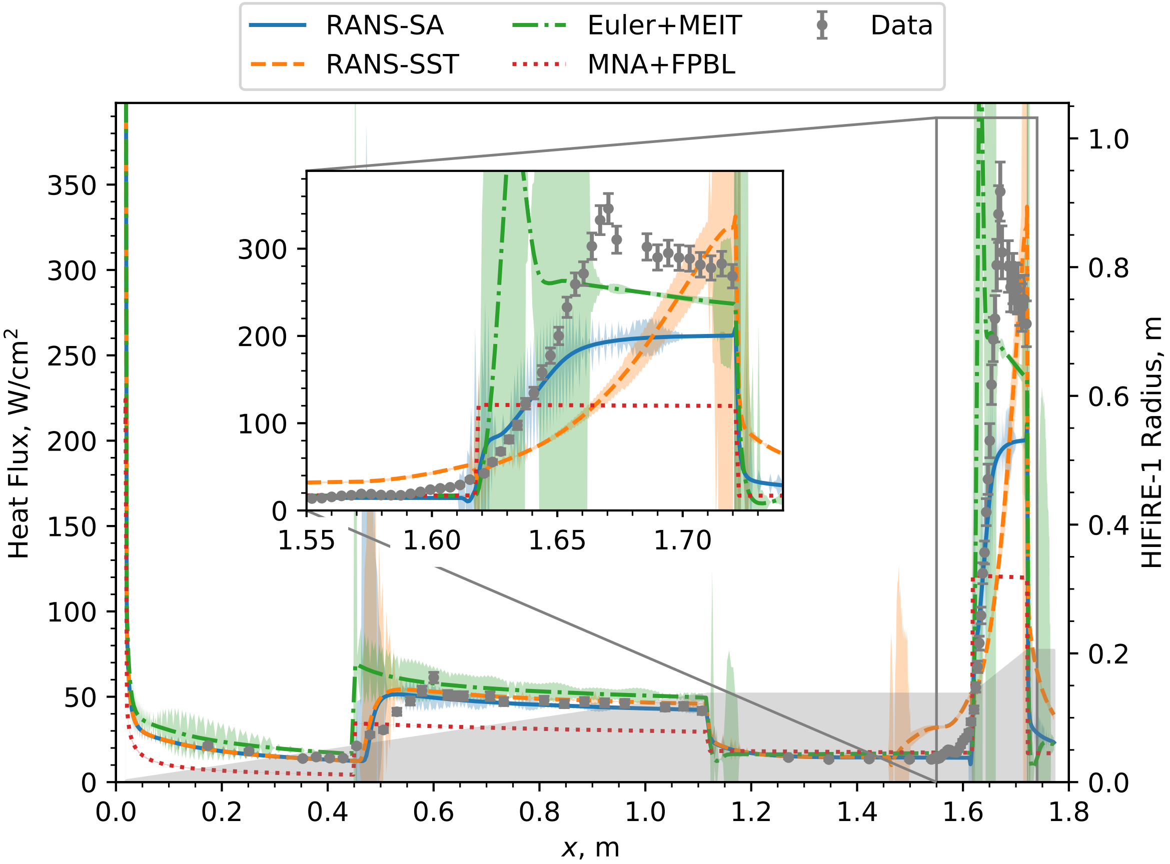

**Figure 5-19.** HIFiRE-1 wind tunnel test heat flux data and predictions, Run 30.

To provide a sense of the differences in surface heat flux between runs, Figure 5-23 shows the

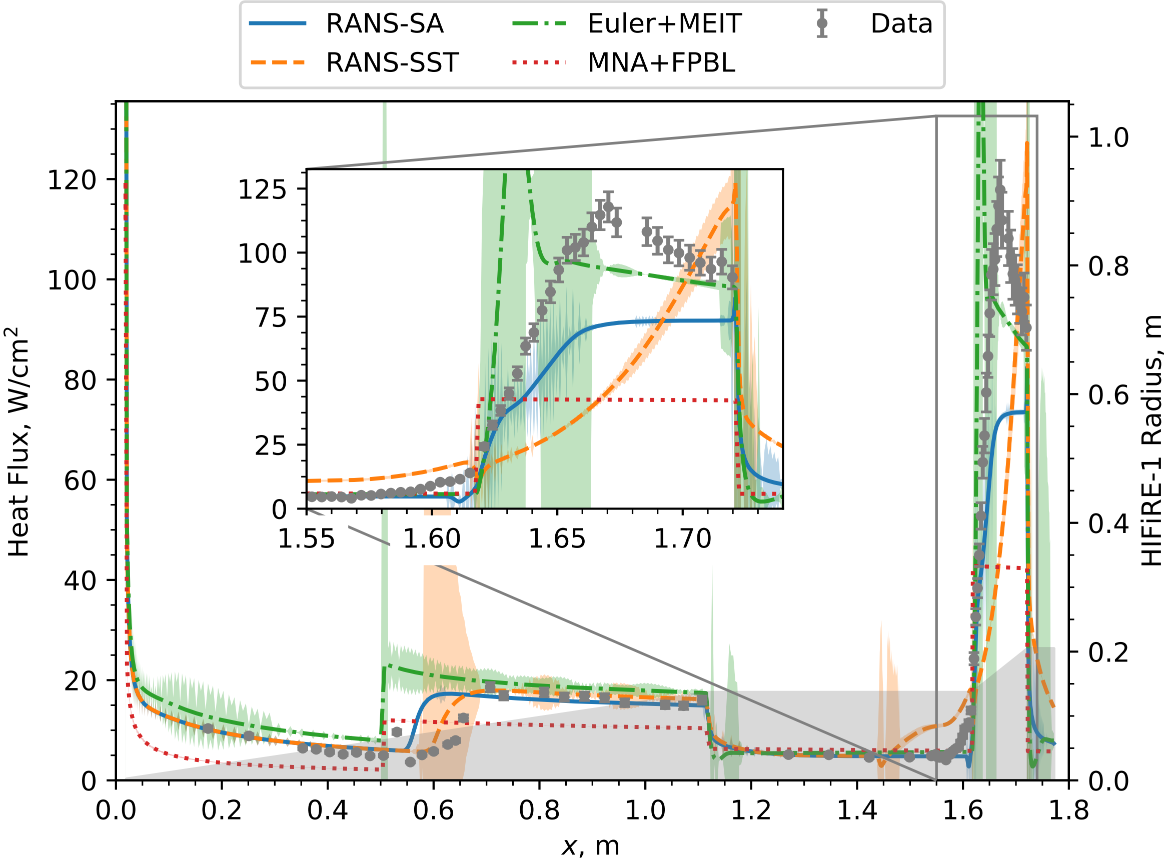

**Figure 5-20.** HIFiRE-1 wind tunnel test heat flux data and predictions, Run 38.

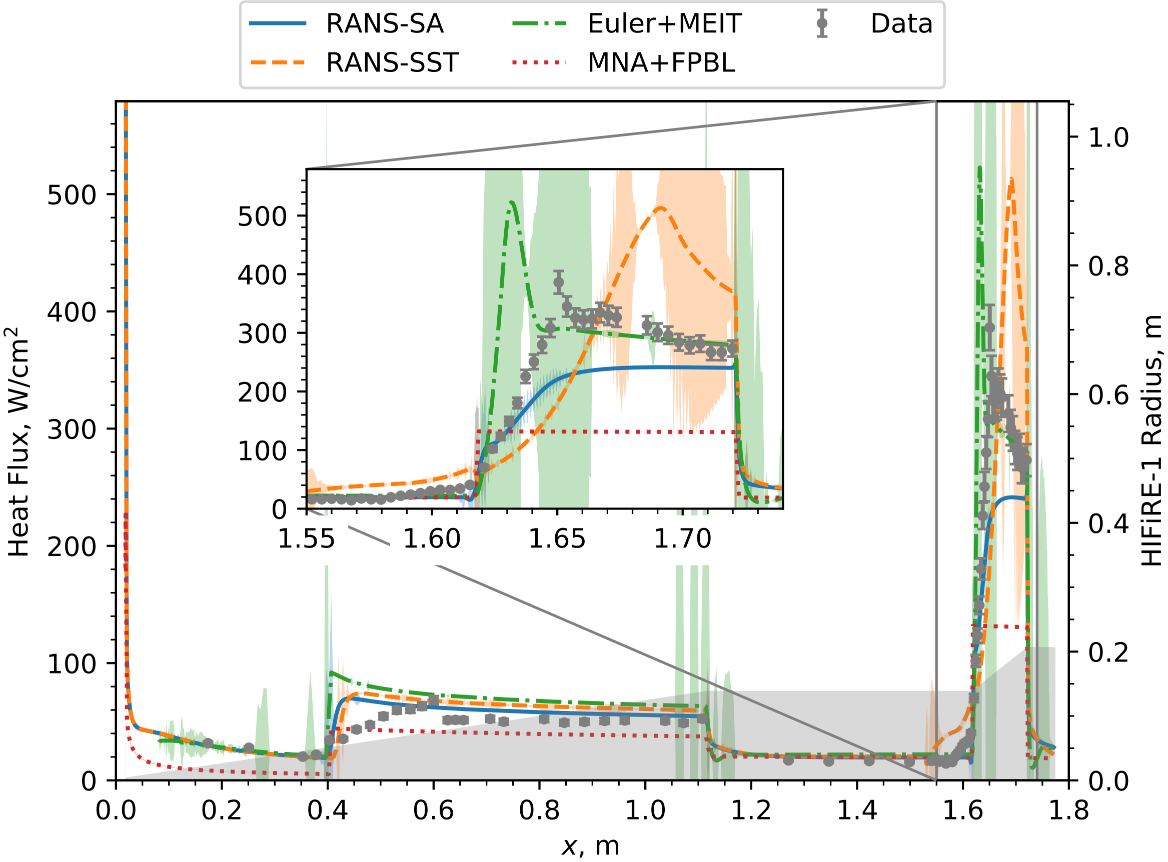

**Figure 5-21.** HIFiRE-1 wind tunnel test heat flux data and predictions, Run 34.

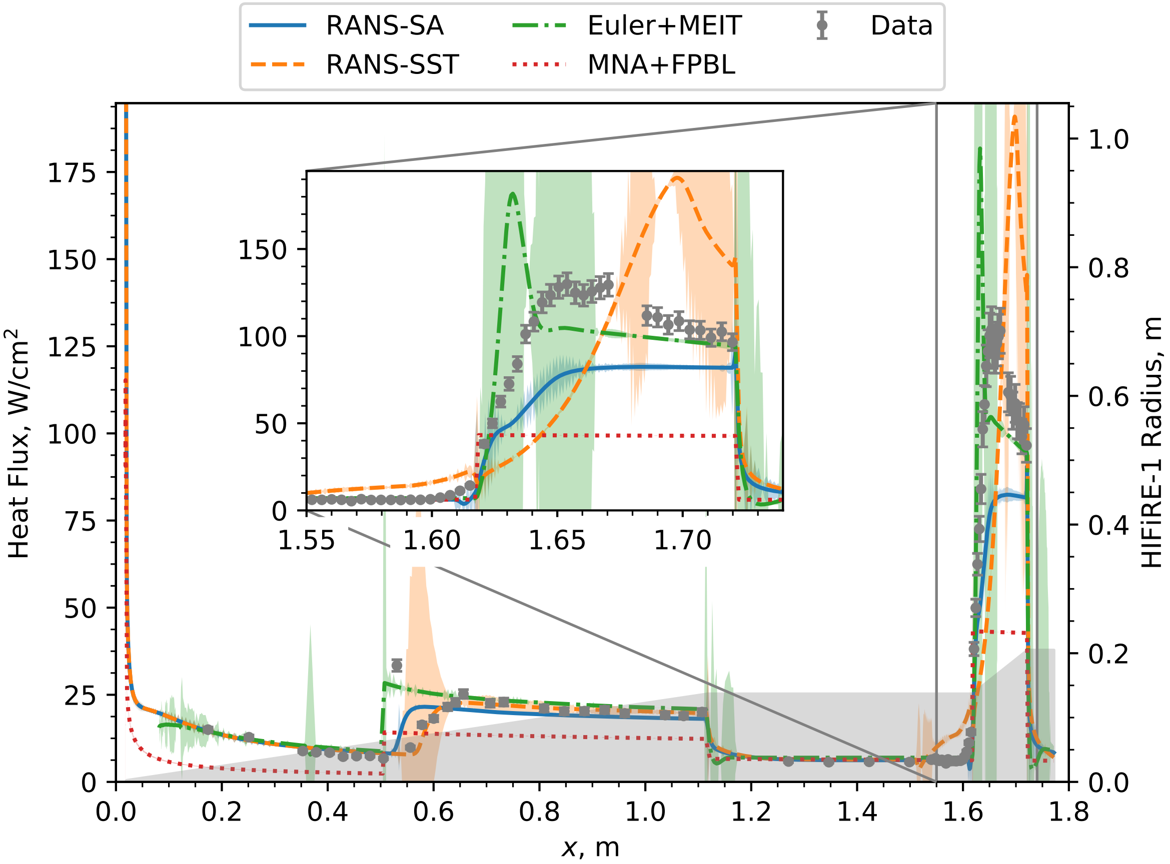

**Figure 5-22.** HIFiRE-1 wind tunnel test heat flux data and predictions, Run 42.

RANS-SA predictions for each run. The heat flux is clearly higher at the high Reynolds number runs (30 and 34) and there is a noticeable difference between predictions for 0° and 2° angles of attack.

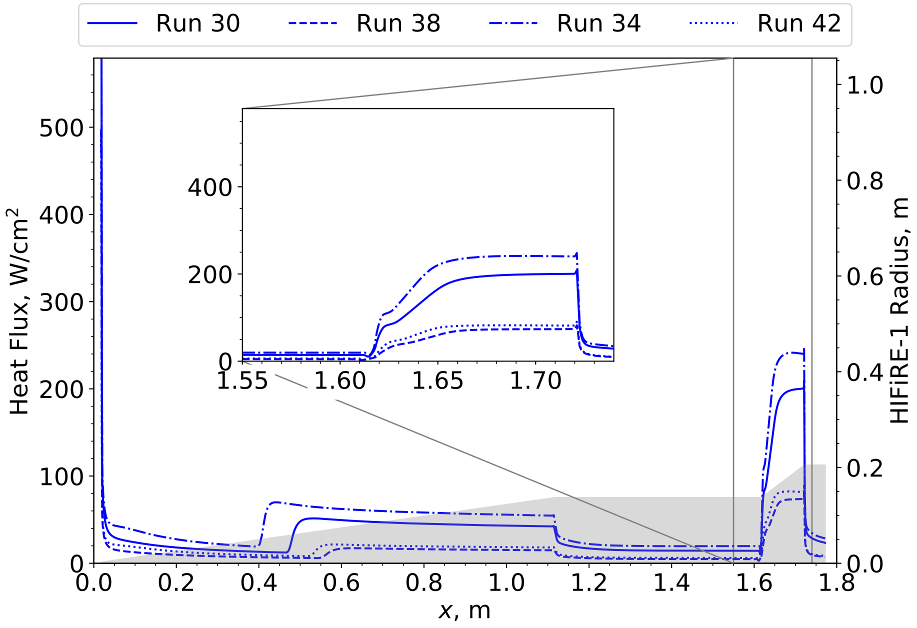

**Figure 5-23.** Comparison of heat flux predictions from RANS-SA models for all analyzed runs.

In Figures 5-24–5-27, the relative error for each model on the four runs is shown, together with the total relative validation uncertainty, $U_{\mathrm{val}}$. Validation uncertainty for all models on Run 30 is generally reduced in this study vs the results from [1]. For all runs, there are large regions in which error is discernable from uncertainty, with exceptions in Euler+MEIT results being the large uncertainty at the transition location, at the cone/cylinder intersection, and on the flare. RANS-SST results show large uncertainty at the transition location and around the flare. Errors are largest for most models (except MNA+FPBL) at the transition location and on the flare. For MNA+FPBL results, the error starts out as a large negative value on the laminar cone and is significant on the turbulent cone and flare. As noted in [1], a difference is expected between MNA+FPBL results and experimental data on the cone and flare, because of the flat-plate geometry assumption used in the model.

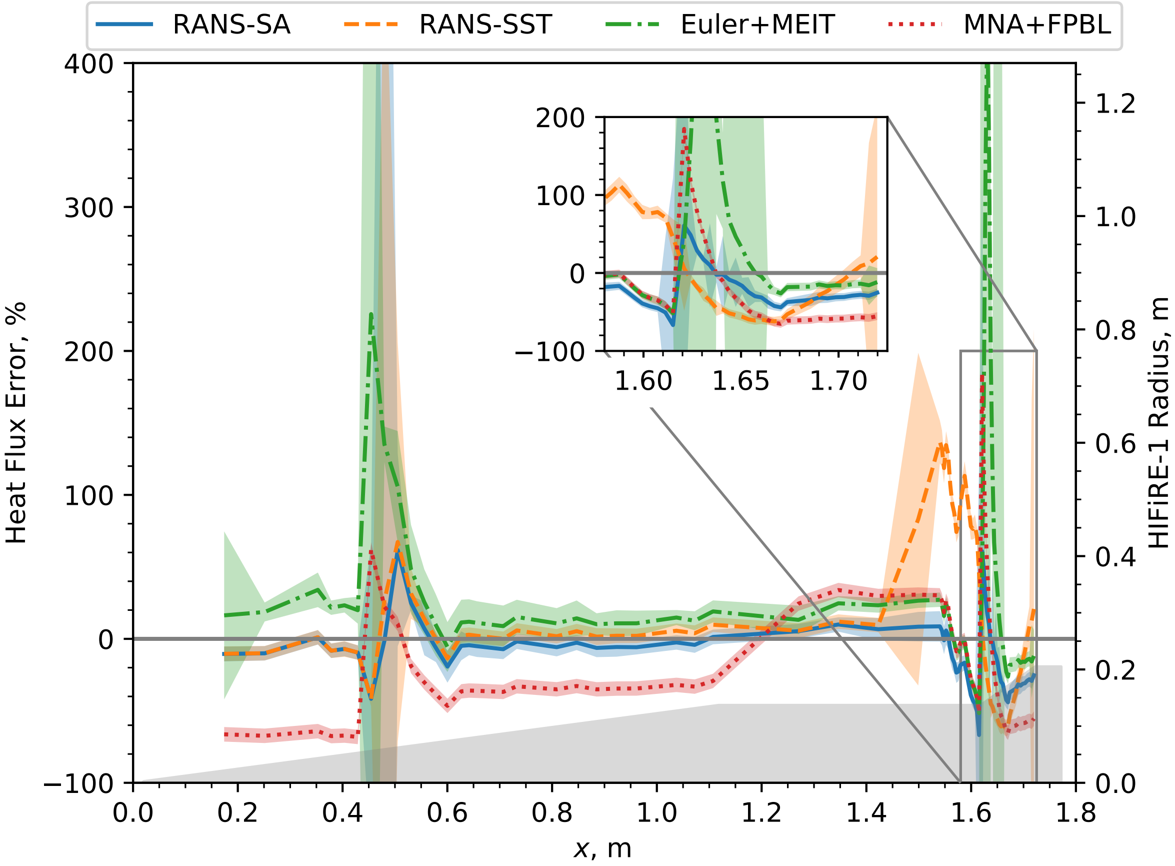

**Figure 5-24.** HIFiRE-1 heat flux prediction error with uncertainty for Run 30.

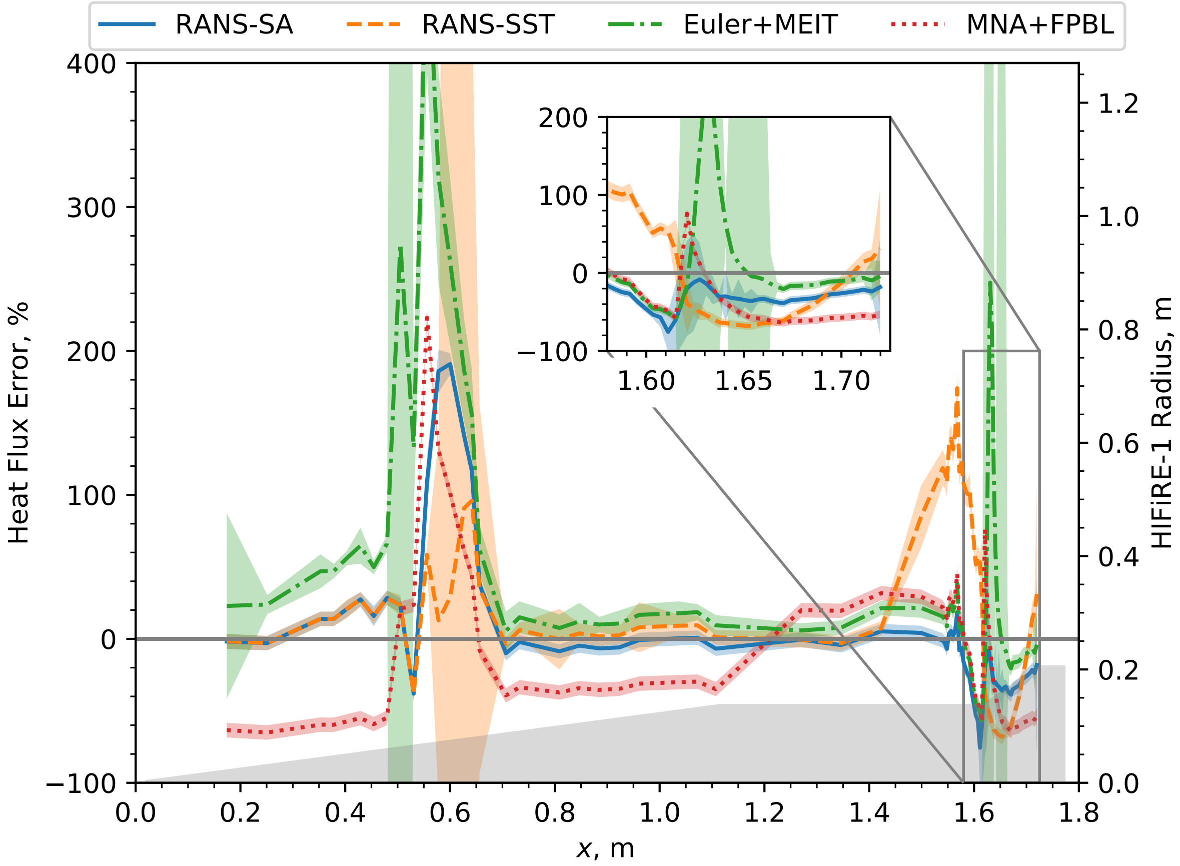

**Figure 5-25.** HIFiRE-1 heat flux prediction error with uncertainty for Run 38.

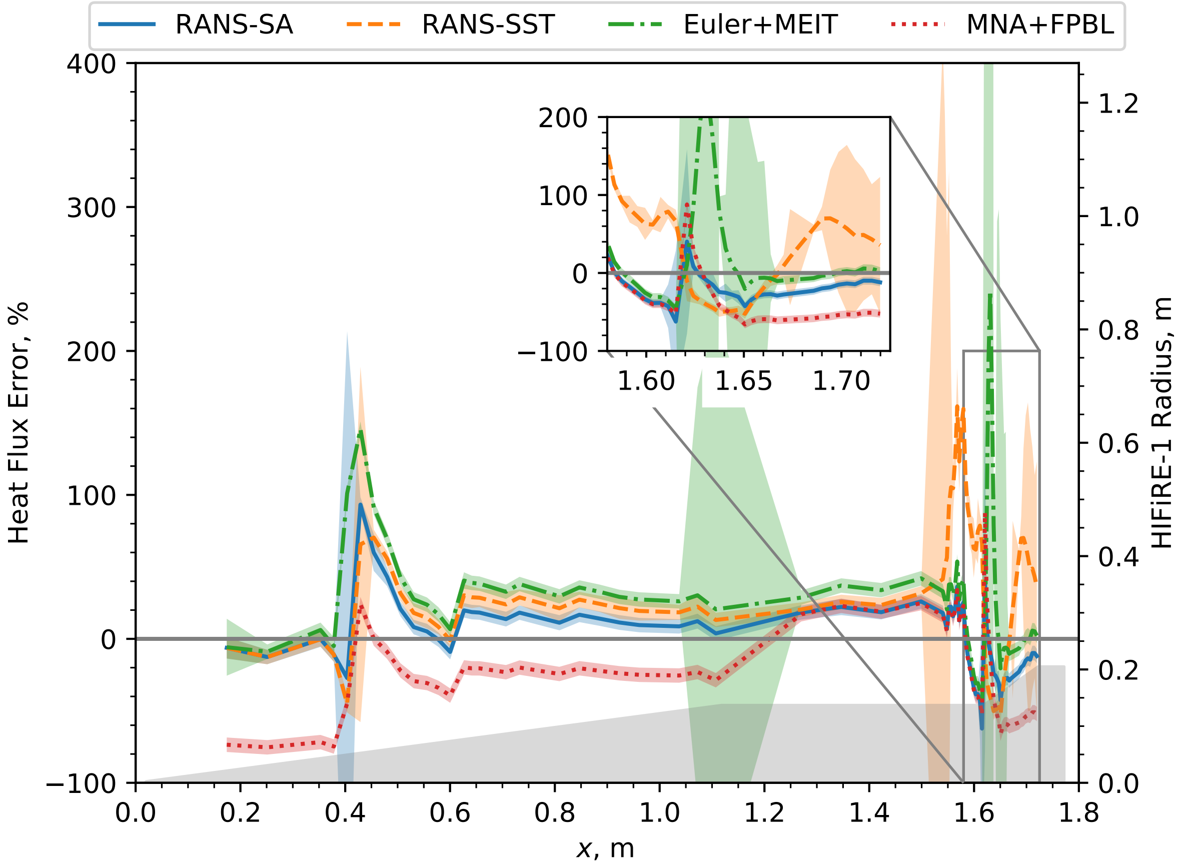

**Figure 5-26.** HIFiRE-1 heat flux prediction error with uncertainty for Run 34.

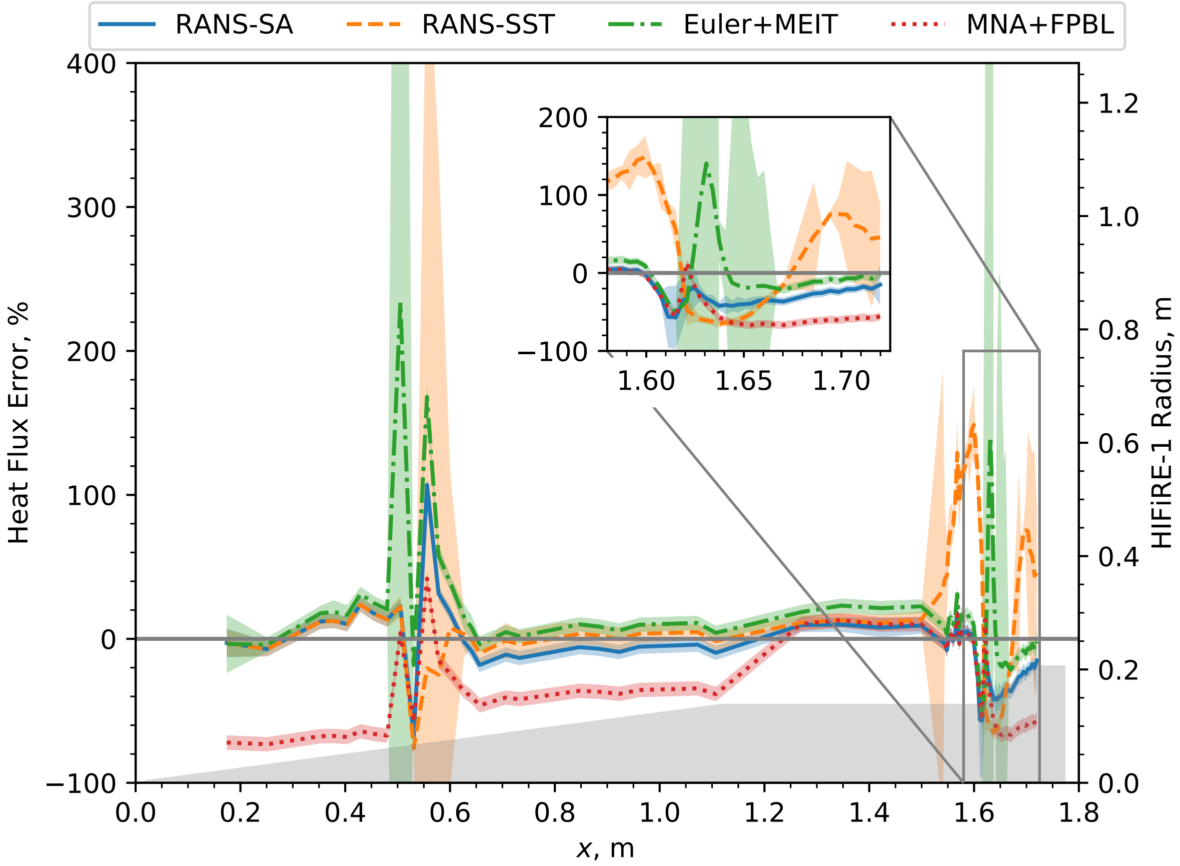

**Figure 5-27.** HIFiRE-1 heat flux prediction error with uncertainty for Run 42.

As in the discussion on surface pressure validation, this section includes several types of bar charts which aid in the drawing of overall conclusions regarding the effect of varying parameters on model performance, and overall model performance. Mean error across models is shown with mean validation uncertainty across models in Figure 5-28. From this figure, it can be seen that the RANS models generally yield the lowest error, followed by MNA+FPBL, and Euler+MEIT, which displays the worst error and highest validation uncertainty. Uncertainty is large for RANS-SA, RANS-SST, and Euler+MEIT. Important caveats to this trend are discussed above, and should be taken into account in uses of each model.

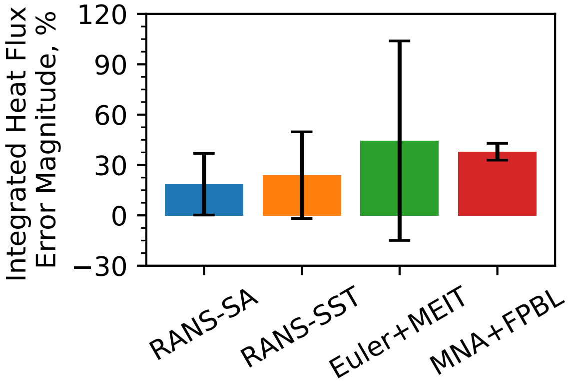

**Figure 5-28.** Relative error averaged across runs.

In Figure 5-29, relative error integrated over the vehicle at the 0° meridional angle is shown with integrated validation uncertainty. Error is generally highest for the MNA+FPBL model, and the RANS models show the lowest errors for all runs. Validation uncertainty is large for Euler+MEIT and RANS-SST for all runs, and for RANS-SA on Run 30.

The plots in Figure 5-29 give a direct comparison between results for each run at the 0° meridional angle. To examine model performance over the entire vehicle, the consolidation of error and uncertainty data is taken to the next level by computing a weighted average of the integrated results from the 0°, 90°, and 180° meridional angles (5-30). In contrast to the surface pressure error results, the heat flux results show reduced relative error in the RANS-SST results compared to Euler+MEIT and MNA+FPBL errors. Integrated error is highest for Euler+MEIT except for on Run 30, where it is lower than MNA+FPBL error. The validation uncertainty is so large as to make error not discernible for the Euler+MEIT results in general, for the RANS-SA results on Runs 30 and 34, and for the RANS-SST results on Run 38. This indicates the usefulness of further mesh refinement and model improvement. It should be noted that inclusion of nonzero meridional angles caused the overall Euler+MEIT error to be relatively larger for Runs 34 and 42, which is attributable to the fact that the current implementation assumes axisymmetric flow.

Figure 5-31 shows integrated error and validation uncertainty for each model on each section, at the 0° meridional angle. It is apparent that for all runs, relative heat flux error is generally lowest on the cylinder, and highest on the turbulent cone and flare. This follows the trends seen in Figures 5-24– 5-27. RANS-SST predictions on the cylinder are relatively high, and this corresponds to the large error in the region just before the flare, where the RANS-SST model predicts the early onset

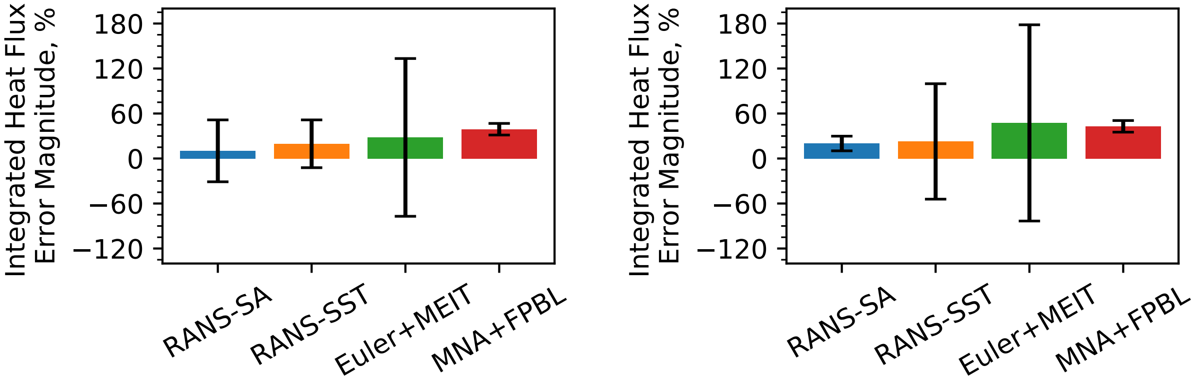

**(a)** Run 30

**(b)** Run 38

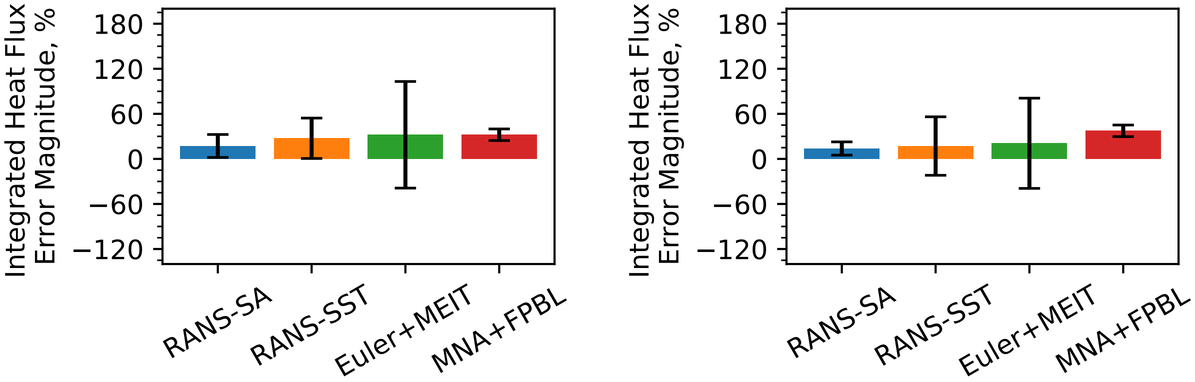

**(c)** Run 34

**(d)** Run 42

**Figure 5-29.** Relative error and validation uncertainty, integrated over all axial locations at the 0° meridional angle.

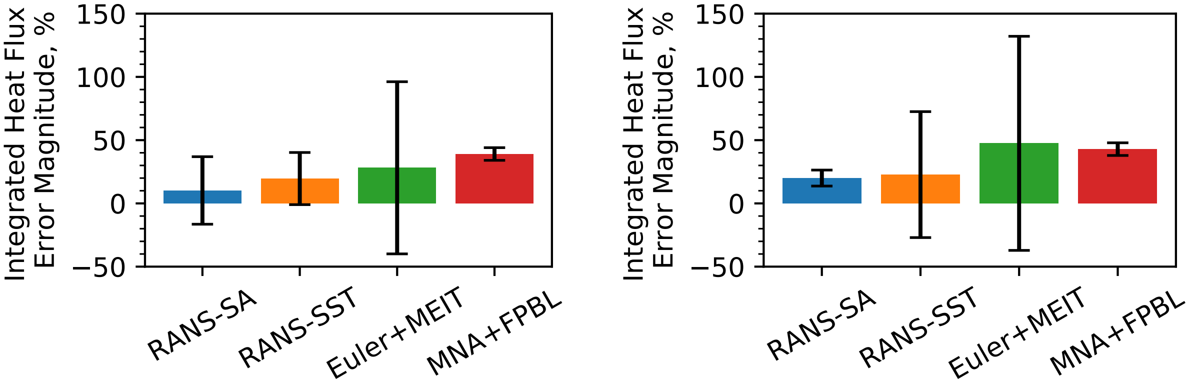

**(a)** Run 30 **(b)** Run 38

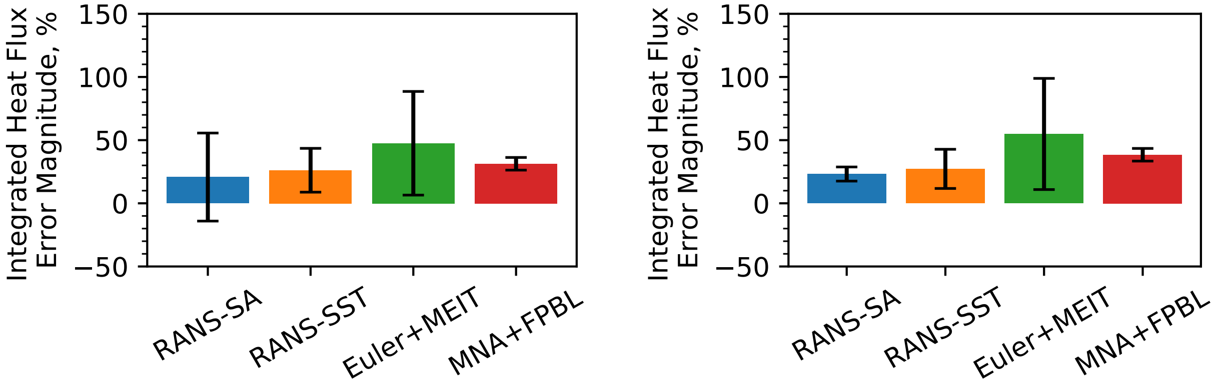

**(c)** Run 34 **(d)** Run 42

**Figure 5-30.** Relative error and validation uncertainty, integrated over vehicle and averaged over all meridional angles.

of the separation region. On the turbulent cone, this model performs better than RANS-SA for Runs 38 and 42 (low Reynolds number). As with surface pressure, the RANS-SA model shows error generally less than 40% for all runs, in each section. The RANS models generally show the highest validation uncertainty on the turbulent cone. Validation uncertainty is generally high in each section for Euler+MEIT.

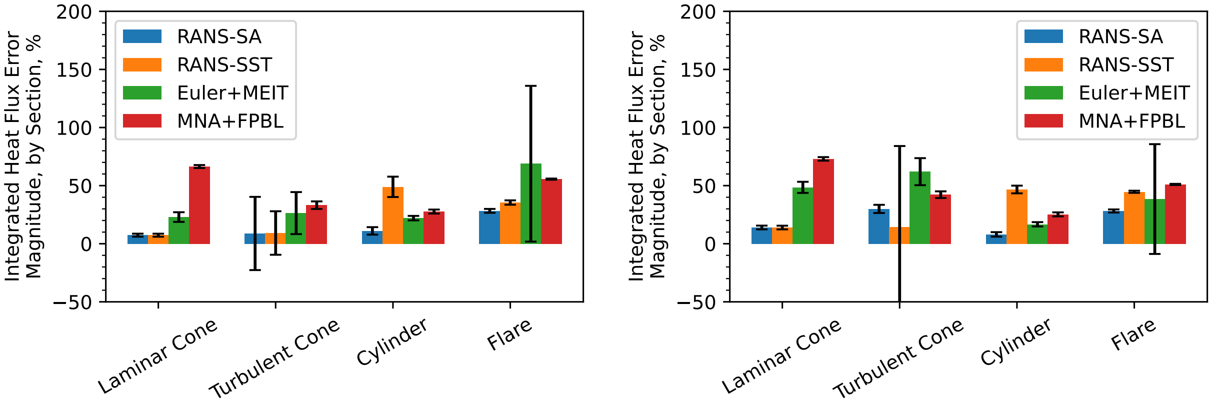

**(a)** Run 30 **(b)** Run 38

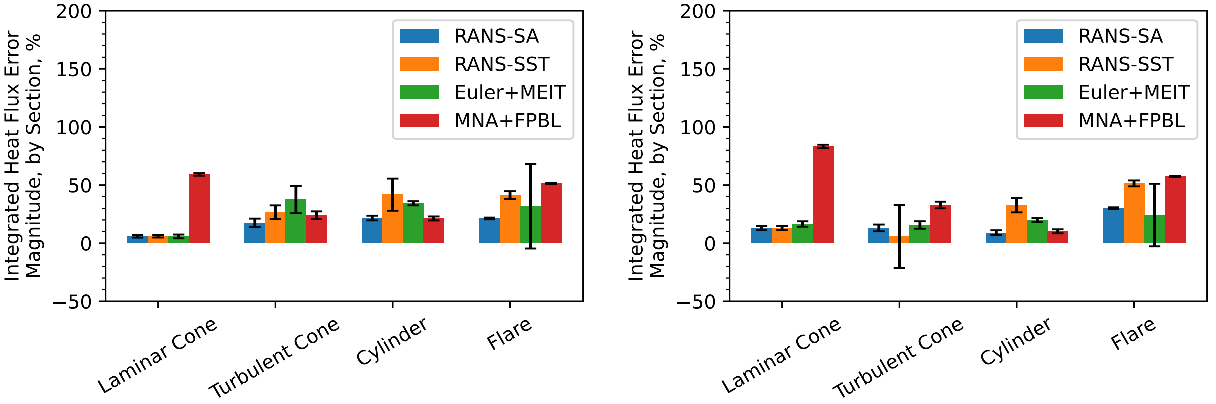

**(c)** Run 34 **(d)** Run 42

**Figure 5-31.** Relative error and validation uncertainty, integrated over vehicle at 0° meridional angle.

In Figure 5-32, section-specific integrated error and validation uncertainty values are shown for the 90° and 180° meridional angles, for Runs 34 and 42. Results are not plotted for some regions due to sensor scarcity at these meridional angles. RANS-SA error is generally lowest for each run and meridional angle. The MNA+FPBL error is higher than that of the other models on the cylinder for nonzero meridional angles, which is not true for the 0° meridional angle. MNA+FPBL generally outperforms RANS-SST and Euler+MEIT on the turbulent cone and cylinder for the 0° meridional angle of Run 34, but at the two other angles, this is generally not the case. The Euler+MEIT model generally struggles at the 90° meridional angle, both in terms of error and validation uncertainty. Other observations may be drawn from these plots depending on specific model applications.

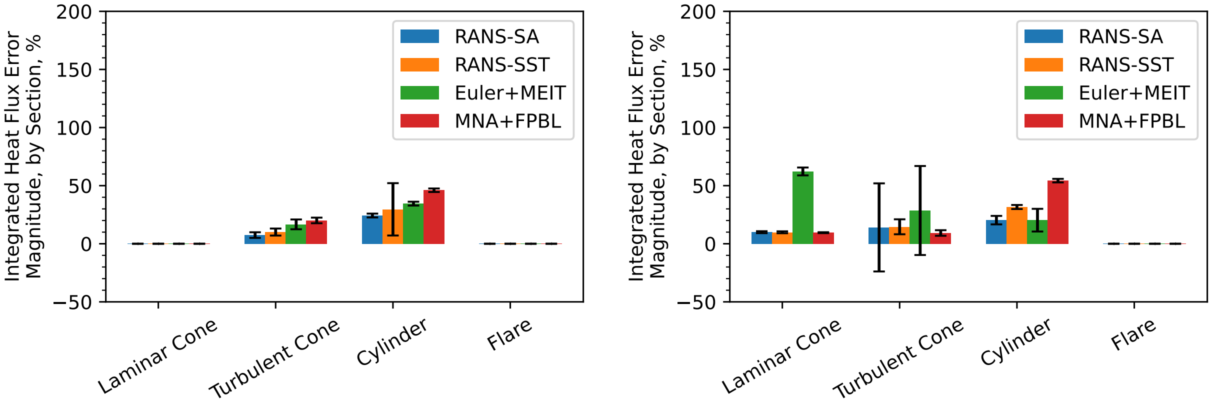

**(a)** Run 34, 90° meridional angle

**(b)** Run 34, 180° meridional angle

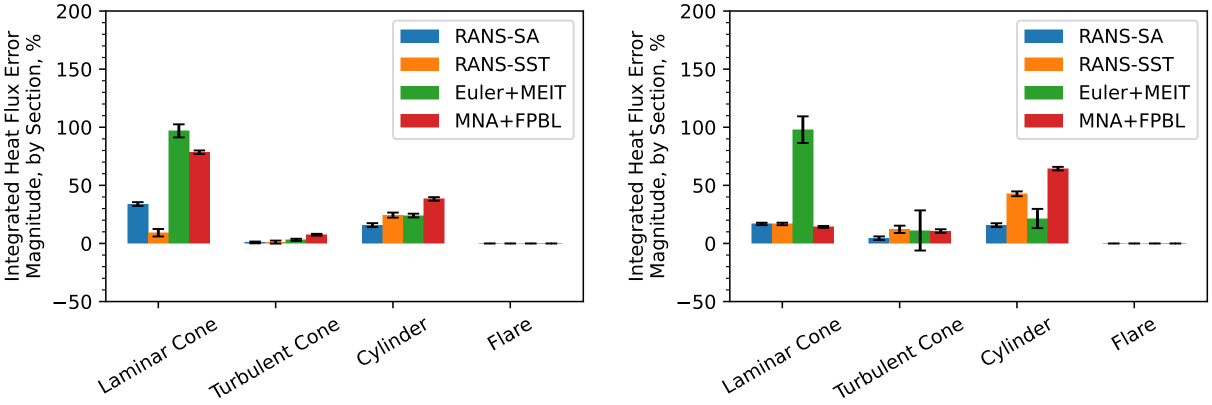

**(c)** Run 42, 90° meridional angle

**(d)** Run 42, 180° meridional angle

**Figure 5-32.** Relative error and validation uncertainty, integrated over vehicle at 90° and 180° meridional angles.

Integrated heat flux errors over the turbulent cone are shown separately in Figures 5-33 and 5-34. At the 0° meridional angle, the RANS errors are generally below 40%, with exceptions for RANS-SA on Run 38 and RANS-SST on Run 34. Euler+MEIT errors are generally the highest, and are accompanied by relatively high uncertainty. Though relative errors rarely exceed 100% for any model, they are not negligible, and can be higher than errors on other sections of the vehicle, as shown in Figures 5-31 and 5-32.

Integrated relative errors for the 90° and 180° meridional angles are shown for Runs 34 and 42 in Figure 5-34. For Run 34, errors are highest at the 0° and 180° meridional angles, except that the MNA+FPBL model has low error at the 180° meridional angle. For Run 42, errors are generally lower than those of Run 34. The lowest errors are seen at the 180° meridional angle, and the highest at the 0° meridional angle. These results are not as conclusive as might be hoped, but do indicate that surface heat flux predictions have significant errors at all meridional angles, and that certain combinations of Reynolds number and angle of attack may result in lower errors (e.g. the Run 42 conditions). In addition, the lower fidelity models appear more prone to variability in error at different meridional angles. One reason for this for the Euler+MEIT model specifically is its current implementation, which assumes axisymmetric flow.

In Figure 5-35, integrated relative error and validation uncertainty are shown for fixed Reynolds number with the angle of attack varied. Relative heat flux error increases for all models except MNA+FPBL when the angle of attack is increased from 0° to 2°. The increase in the Euler+MEIT model's error at nonzero angle of attack is likely partially attributable to the current model formulation which assumes streamlines aligned with the vehicle's axis.

In Figure 5-36, integrated relative error and validation uncertainty are shown for fixed angle of attack with the Reynolds number varied. Error decreases for higher Reynolds number for all models in both plots. This is likely partially attributable to reduced separation region sizes as noted for surface pressure, but also likely has other causes. Because this phenomenon is distinct from that seen in the surface pressure error, further examination would be beneficial to determine fundamental causes for this behavior.

### 5.2.3. Future Work

In this study, the work in [1] is expanded to include three additional runs from the HIFIRE-1 experimental dataset. This allowed for analysis of MFTK model performance over a range of Reynolds numbers and angles of attack, and resulted in several conclusions about model performance in general and for specific scenarios. In addition, simulations were run on the finest mesh (1L), and numerical uncertainty was reduced as a result. In the future, higher enthalpy experimental datasets will be utilized for additional validation studies, in order to examine the performance of the reacting gas models within MFTK. Additionally, the advanced CFL controller will be further utilized, and further mesh refinement for the Euler+MEIT simulations will be explored.

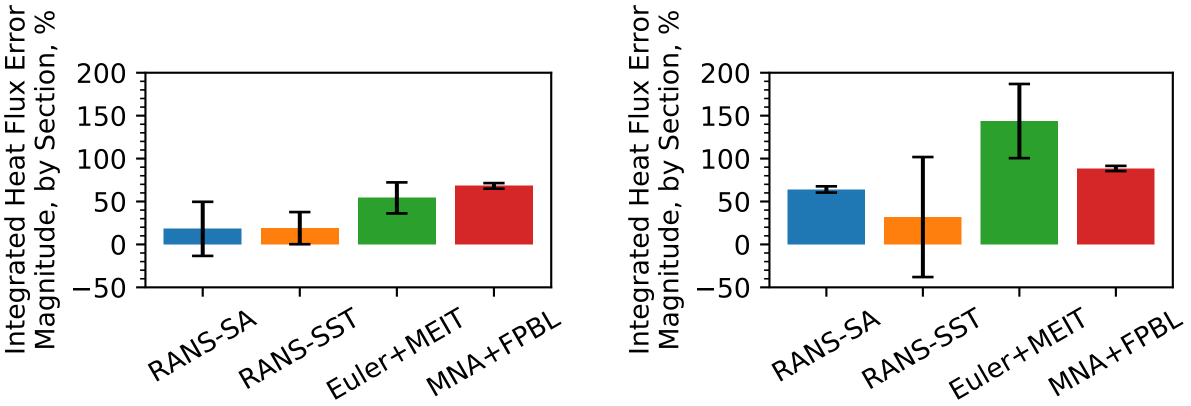

**(a)** Run 30 **(b)** Run 38

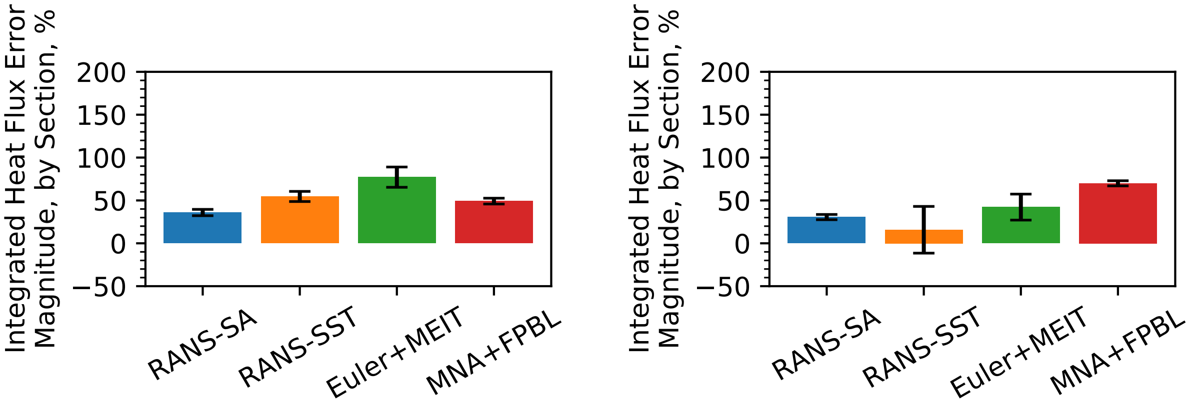

**(c)** Run 34 **(d)** Run 42

**Figure 5-33.** Relative error and validation uncertainty, integrated over turbulent cone section of vehicle, at 0° meridional angle.

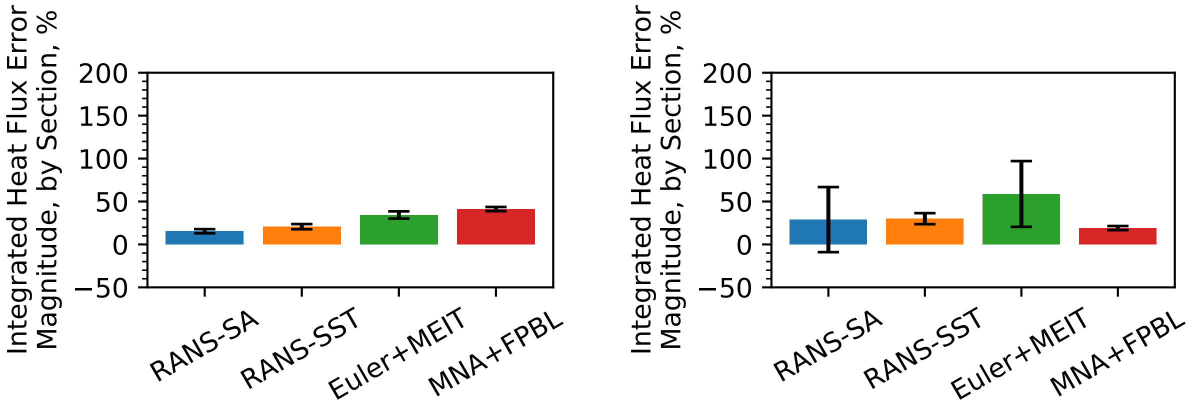

**(a)** Run 34, 90° meridional angle.

**(b)** Run 34, 180° meridional angle.

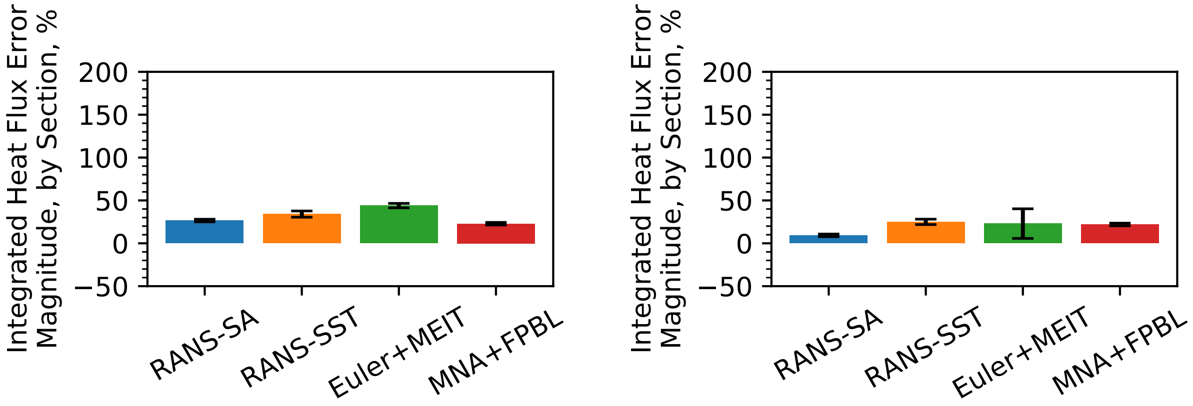

**(c)** Run 42, 90° meridional angle.

**(d)** Run 42, 180° meridional angle.

**Figure 5-34.** Relative error and validation uncertainty, integrated over turbulent cone section of vehicle, at 90° and 180° meridional angles.

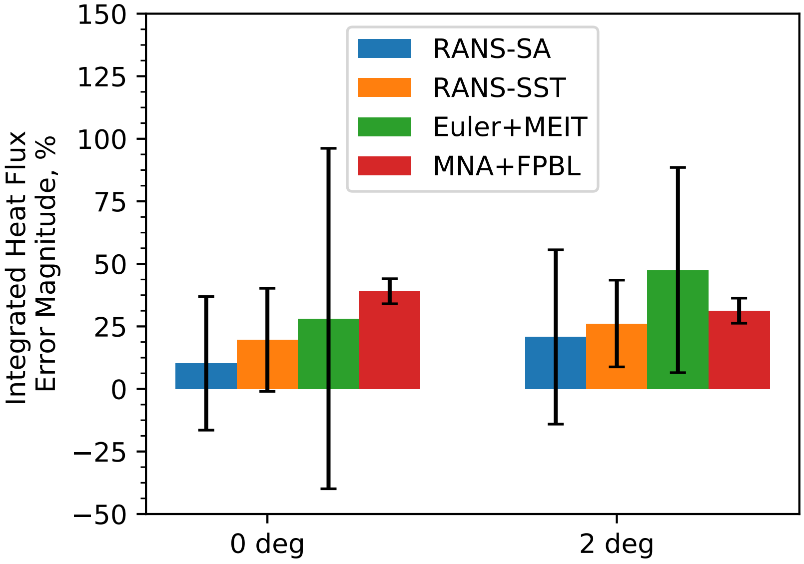

**(a)** Relative error for Runs 30 and 34 (high Re), with varied angle of attack.

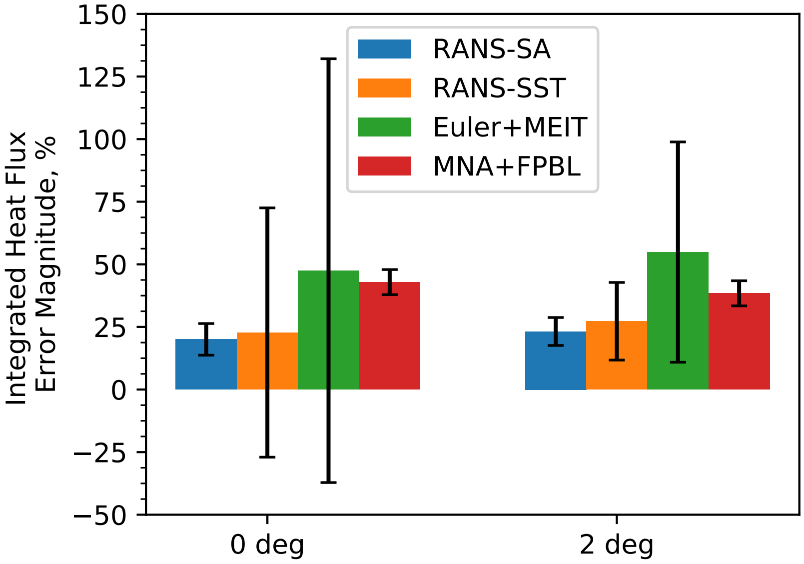

**(b)** Relative error for Runs 38 and 42 (low Re), with varied angle of attack.

**Figure 5-35.** Relative error with fixed Re, varied angle of attack.

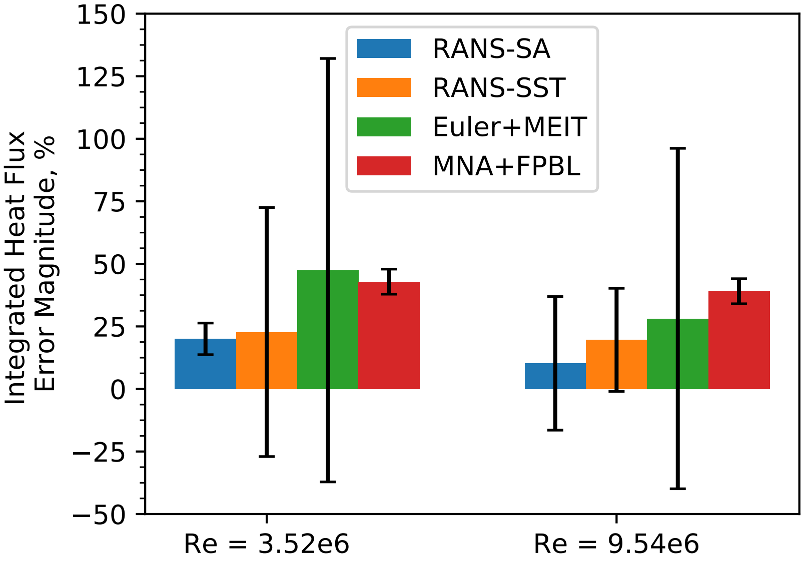

**(a)** Relative error for Runs 38 and 30 (0° angle of attack), with varied Reynolds number.

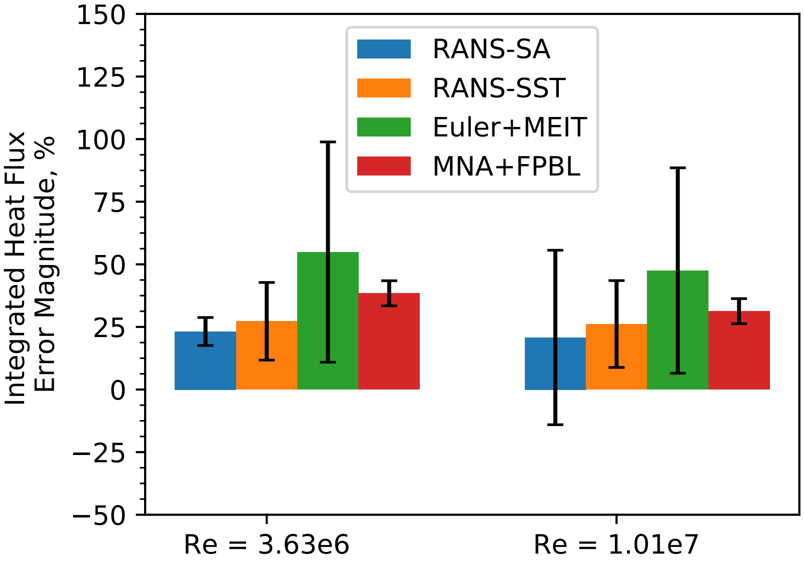

**(b)** Relative error for Runs 42 and 34 (2° angle of attack), with varied Reynolds number.

**Figure 5-36.** Relative error with fixed angle of attack, varied Reynolds number.

# 6. VALIDATION ERROR EXTRAPOLATION

## 6.1. Motivation

Computational simulation is highly useful as a companion to experimentation. In general, simulation results should be compared against experimental data in validation studies. However, computational simulation is often used in practice in situations for which there are no (or limited) experimental data to compare against. There are several possible reasons for this. One is prohibitions against testing. Another common case is when computational simulation is used as a tool for test design, to help minimize the number, cost, and failure of tests. Whatever causes the need for computational results in the face of scarce experimental data, the fact remains that simulations are often used to make predictions which fall outside of the range of available experimental data. Thus, no error estimate can be directly made on such results, as there is no experimental data to compare them to. However, obtaining an estimate of validation error through extrapolation is often more useful than assuming no error or a standard percentage error (i.e. 20% of the QoI magnitude). While the results of validation error extrapolation are thought to prove more useful than no information, it is recommended to consider the impact of making high-consequence decisions with an imperfect process. When using extrapolation to estimate validation error, one must consider to what extent extrapolation is required between the validation and application conditions. In addition, the evidence which provides confidence in the ability to extrapolate should be examined.

In this section, validation error is examined across the parameter space described by the Reynolds numbers and angles of attack of the cases investigated in this report. The validation error computed at locations where experimental data existed is extrapolated to other points in the Reynolds number – angle of attack parameter space. This is done with error trends expressed as lines across a single parameter (2D plots) and with error trends expressed as surfaces over the two-dimensional space defined by both parameters (3D plots). The results follow in the next two sections.

## 6.2. Two-dimensional Results

The first extrapolation exercise done is extrapolation of validation error over Reynolds number space with fixed angle of attack. This is done for both angles of attack considered in this study (0° and 2°). The error considered here is the integrated relative error in each QoI. The error is relative in the sense that it is normalized by the experimental data, and it is integrated over all space (all axial locations for which experimental data exist, for all meridional angles, where applicable). Thus, this is the same overall error for the four runs as is shown in Figures 5-12 and 5-30. This error is interpolated between "known" points (where simulation and experimental results exist) and extrapolated outside of these points. A simple linear extrapolation of the error trend is done, as only two points exist. To provide an uncertainty estimate on the results, the actual validation uncertainty is used at the "known" points, and linear interpolation is used between these uncertainty values at the "known" points. This uncertainty bound is expanded in the extrapolation region by fitting a line between the lower uncertainty bound on one "known" point and the upper bound on the other, and extrapolating uncertainty using these lines. This method assumes a linear error trend and consistent physics (e.g. primarily turbulent versus laminar flow). The resulting plots are shown Figure 6-1. In the two-dimensional plots, the extents of the x-axes show the range of the application space where predictions are desired. Generally, error decreases with increasing Reynolds number for both QoIs and both angles of attack. However, Figure 6-1c shows an increase in predicted relative pressure error with increasing Reynolds number, indicating that the nonzero angle of attack influences the error trend for this QoI. One thing to note in these results is the care that should be used when applying extrapolated error on the left side of the "known" points. All cases examined in this study have turbulent flow, but some involve manual tripping of the flow on the cone (Runs 38 and 42). One case in the HIFiRE-1 dataset (Run 31) is fully laminar at a Reynolds number of $1.59 \times 10^6$ $m^{-1}$. This is approximately half of the value of the Reynolds number for Runs 38 and 42, and serves as a realistic limit on the extrapolations' valid range.

The same two-dimensional extrapolation is performed over angle of attack with (approximately) fixed Reynolds number. The results are shown in Figure 6-2. Relative pressure error generally decreases with increasing angle of attack, whereas relative heat flux error increases. The exception is the relative heat flux error from MNA+FPBL simulations, which increases as angle of attack increases, for both high and low Reynolds numbers. Two important things should be noted from these plots. One is that when the extrapolated error reaches zero, the immediate conclusion from the extrapolation for that point and further into the parameter space is that validation error is zero. This is true, since the error magnitude is examined here, and negative magnitude does not have meaning. Realistically, some nonzero error would likely be assigned to simulation predictions in this scenario. Such an error estimate might be the error from the nearest "known" point, or another measure. The second thing to notice is that the extrapolation range is large on the right side of the "known" points. The limit ($\alpha = 10^\circ$) was chosen to reflect a realistic upper limit for many hypersonic aerthermodynamic analyses. In practice, extrapolating over such a large range is dangerous for any quantity, as reflected by the wide uncertainty bounds at the limit. Indeed, physics often change with a large parameter space, as is possible here with the separation region growing larger and occurring on additional surfaces as the angle of attack is increased. However, in the absence of experimental data, such an error estimate with an accompanying high uncertainty may be the best option.

While the plots in Figures 6-1 and 6-2 clearly show the error and uncertainty extrapolation technique investigated in this study, the uncertainties used are only the experimental uncertainties as opposed to total validation uncertainties. Thus, the same procedure is followed with the validation uncertainty (Equation 6.1), integrated over axial space and averaged over the three meridional angles. Both the experimental uncertainties and the overall validation uncertainties are at the $2\sigma$ (95%) confidence level, as discussed in Section 5.1, and are used to bound the error as shown in Equation 6.2. The plots with validation uncertainty are shown in Figures 6-3 and 6-4. The uncertainties are much larger, especially in the extrapolated regions, indicating that a different technique may be appropriate for better estimating the uncertainty, but that the technique used here

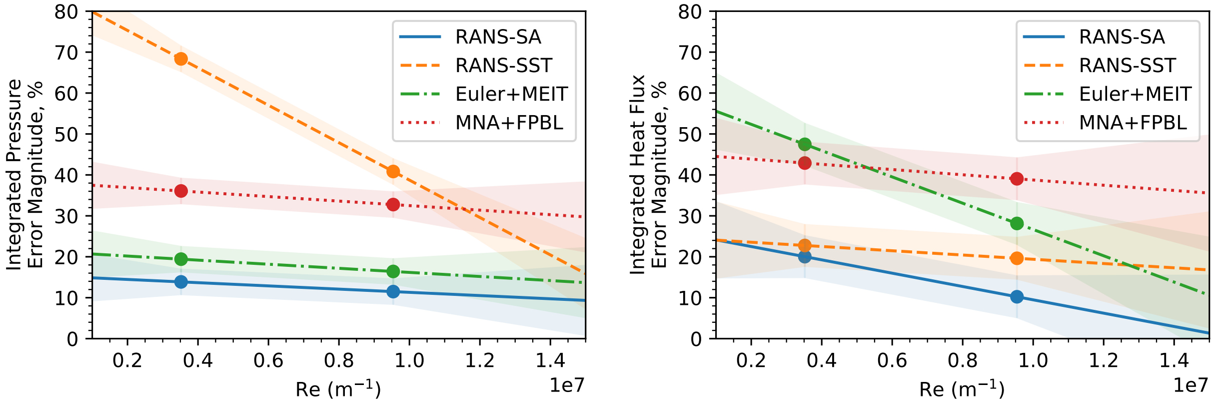

**(a)** Pressure error, $\alpha = 0°$.

**(b)** Heat flux error, $\alpha = 0°$.

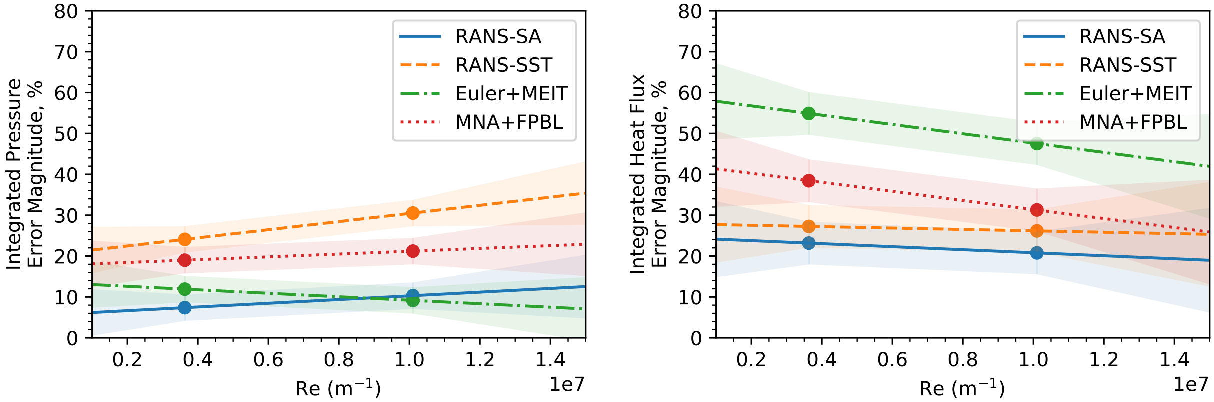

**(c)** Pressure error, $\alpha = 2°$.

**(d)** Heat flux error, $\alpha = 2°$.

**Figure 6-1.** Validation error extrapolation across Reynolds number, with only experimental uncertainty.

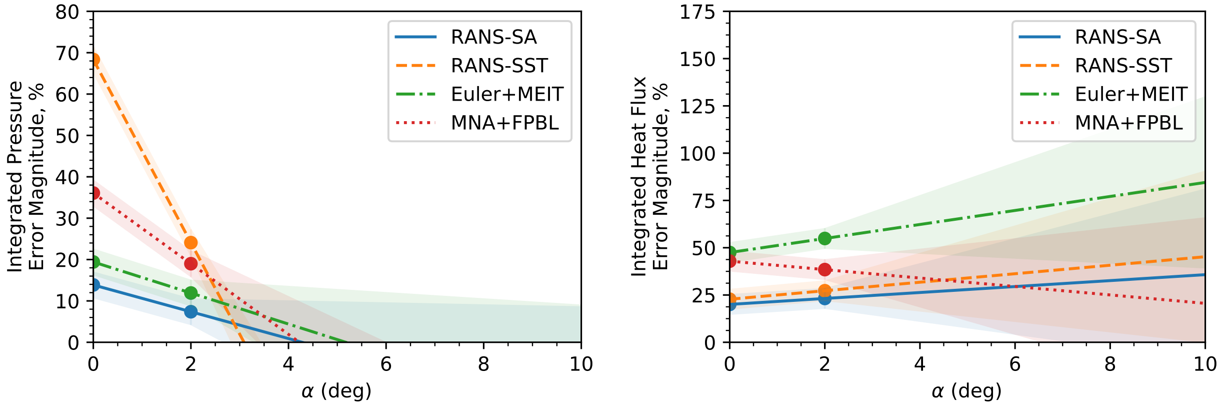

**(a)** Pressure error, Re $\approx 3.6 \times 10^6$ m$^{-1}$.

**(b)** Heat flux error, Re $\approx 3.6 \times 10^6$ m$^{-1}$.

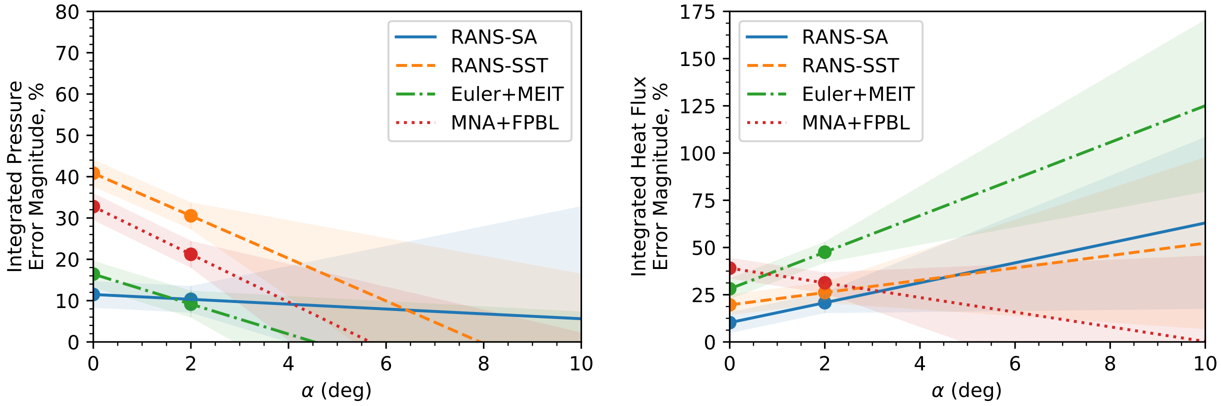

**(c)** Pressure error, Re $\approx 1 \times 10^7$ m$^{-1}$.

**(d)** Heat flux error, Re $\approx 1 \times 10^7$ m$^{-1}$.

**Figure 6-2.** Validation error extrapolation across angle of attack, with only experimental uncertainty.

could serve as a conservative estimate of extrapolation uncertainty. Another apparent conclusion from these results is the caution which is needed when placing confidence in extrapolated values. The Euler+MEIT uncertainties are quite high in most cases, and RANS-SST uncertainties are often significantly higher than those of RANS-SA and MNA+FPBL. In many cases, the predicted uncertainty is reasonably low for both RANS-SA and MNA+FPBL.

$$\begin{aligned} U_{\text{val}} &= \sqrt{U_{\text{num}}^2 + U_{\text{input}}^2 + U_D^2} \\ &\approx \sqrt{GCI^2 + U_D^2} \end{aligned} \tag{6.1}$$

$$\delta_{\text{model}} \in [E - U_{\text{val}}, E + U_{\text{val}}]. \tag{6.2}$$

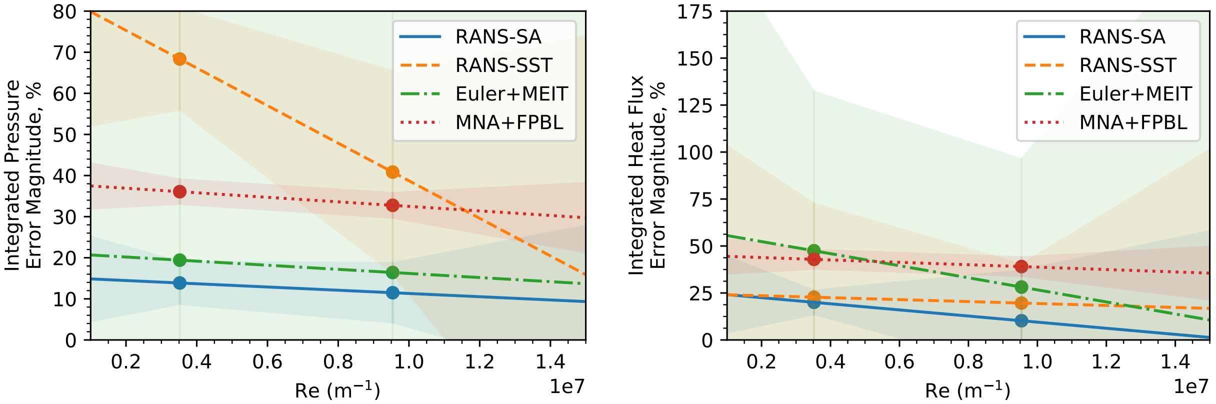

**(a)** Pressure error, $\alpha = 0°$.

**(b)** Heat flux error, $\alpha = 0°$.

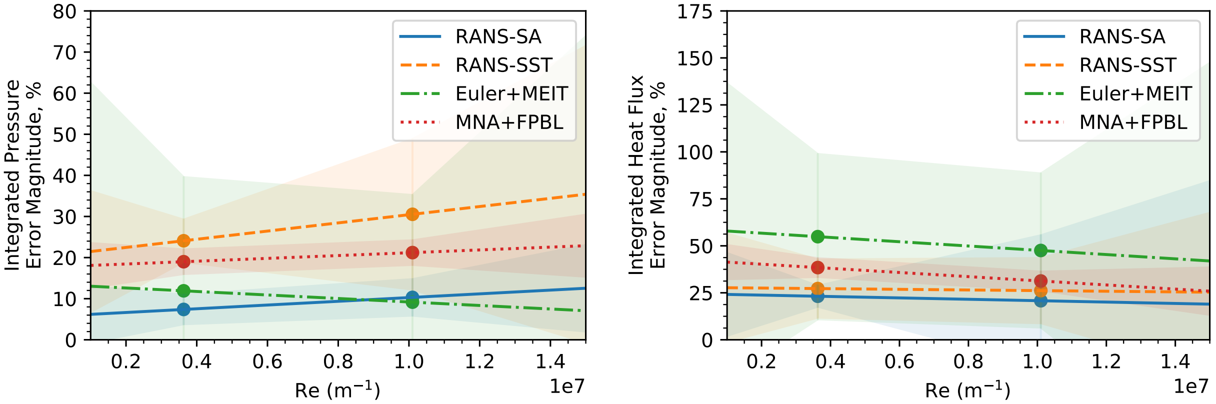

**(c)** Pressure error, $\alpha = 2°$.

**(d)** Heat flux error, $\alpha = 2°$.

**Figure 6-3.** Validation error extrapolation across Reynolds number, with validation uncertainty.

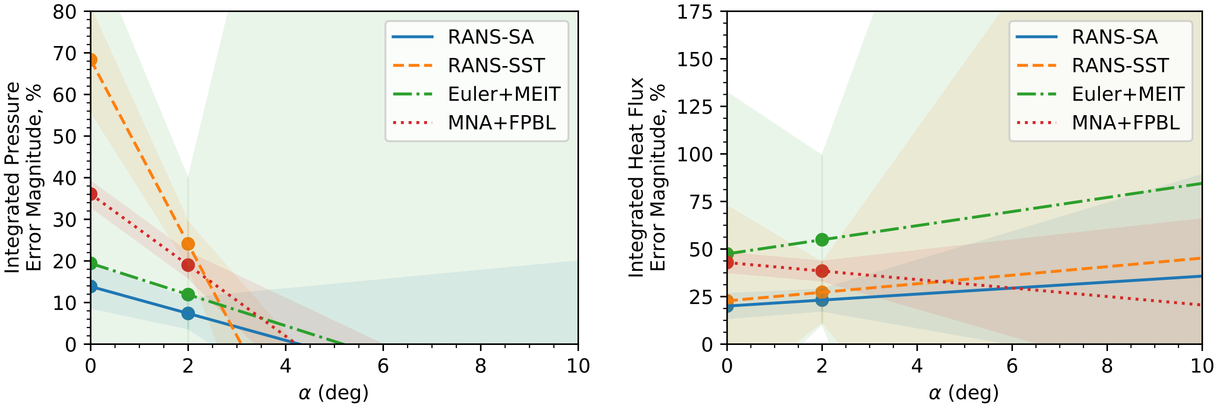

**(a)** Pressure error, Re $\approx 3.6 \times 10^6$ m$^{-1}$.

**(b)** Heat flux error, Re $\approx 3.6 \times 10^6$ m$^{-1}$.

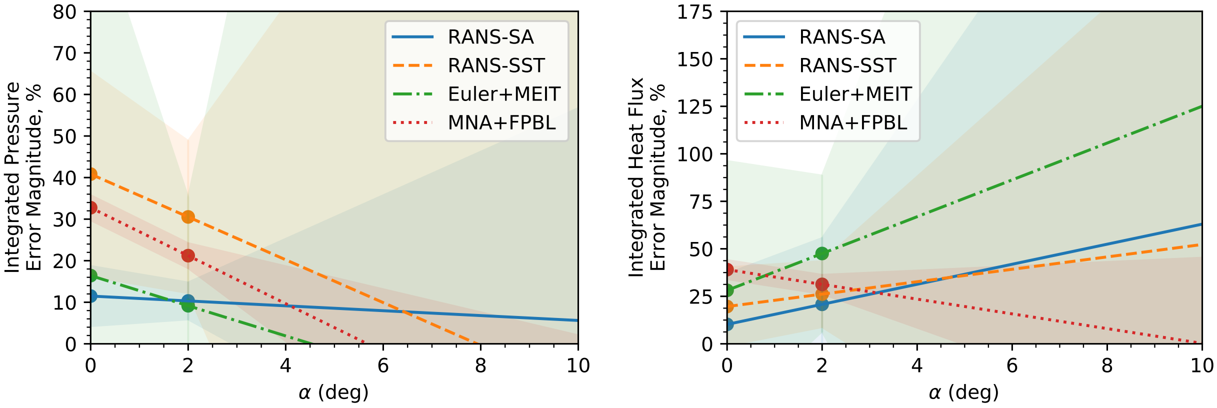

**(c)** Pressure error, Re $\approx 1 \times 10^7$ m$^{-1}$.

**(d)** Heat flux error, Re $\approx 1 \times 10^7$ m$^{-1}$.

**Figure 6-4.** Validation error extrapolation across angle of attack, with validation uncertainty.

## 6.3. Three-dimensional Results

Two-dimensional extrapolation as shown above can be useful in determining realistic validation error across a range of values of a single parameter. However, extrapolating over a two-dimensional parameter space can also be useful for examining error trends influenced by both parameters, overall high- or low- error regions of the parameter space, and a general global view on realistic error. To examine this for the runs analyzed in this study, the relative validation error magnitudes at all four "known" points (the same values as used in the previous section) are plotted in 3D plots against both Reynolds number and angle of attack. Error is interpolated between "known" points in each dimension, and extrapolated linearly outside of the "known" points. These lines are shown in Figure 6-5, and form the basis for an error surface which can be constructed using triangular sub-surfaces defined from vertices which originate from the lines. The four "known" points are vertices, as well as the intersections of extrapolation lines with the domain extents of the parameter space. These outer vertices are connected with grey lines to show the parameter space boundary. When lines cross each other, the average of the two values at the point in the parameter space where they intersect is taken as a vertex. All plots of this type in Figures 6-6–6-13 have the same elements. The error surface arising from the lines of Figure 6-6a is shown in Figure 6-6b, along with its projection onto the parameter space (zero-error plane). The green region indicates the part of the domain in which error is interpolated, and the orange region indicates the part in which it is extrapolated. Such error surfaces are shown in Figures 6-6–6-13 for all model/QoI combinations used in this study. Also shown in these figures are the 2D views of the error surfaces which give insight into error trends with each parameter individually. Due to the complex nature of the plots, uncertainty estimates are not added, as they would likely convolute the surfaces' features and make the plots difficult to read.

In Figure 6-6, the error surface plots for the MNA+FPBL model's pressure predictions are shown. The error changes strongly with angle of attack, decreasing with higher angles of attack. Because the prediction reaches zero quickly, a relatively small region of the parameter space is covered by the extrapolation prediction. The shaded region on the zero-error plane could be extended with a prediction of zero error outside of the predicted space, but as mentioned above, assuming zero error may not be the most robust solution in such circumstances. Thus, only the projection of the directly predicted error before its intersection with the boundaries is shown. In Figure 6-6c, the error surface is shown vs the Reynolds number. It appears to trend downwards as Reynolds number increases, but is not as sensitive to Reynolds number as it is to angle of attack. The error surface for the MNA+FPBL heat flux predictions (Figure 6-7) shows a more gradual change in error as angle of attack changes, which allows more of the parameter space to be covered by the extrapolation predictions. The error surface also shows a higher rate of change in error with Reynolds number.

Figures 6-8 and 6-9 show the error surfaces for the Euler+MEIT predictions. In Figure 6-8, the pressure error surface is shown. It has similar characteristics to the corresponding MNA+FPBL surface, with a sharp decrease in error predicted as angle of attack increases and a slower decrease in error predicted for increasing Reynolds number. The heat flux error surface (6-9) covers a similar region of the parameter space as the corresponding MNA+FPBL surface, but has more surface curvature. The error is predicted to increase in general as the angle of attack increases. However, the high level of surface curvature indicates that the error is predicted to vary strongly in a local sense across the parameter space. Thus, certain combinations of Reynolds number and angle of attack correspond to pockets of relatively low or high error. Ultimately, more "known" points would be useful to better characterize surfaces such as this.

Figures 6-10 and 6-11 show the error surfaces for the RANS-SA predictions. Once again, clear trends are seen for heat flux error vs angle of attack, but the pressure error surface is more spread out for moderate angles of attack. Indeed, the pressure error surface has significant local variation in both parameters. One important feature to note is the low maximum pressure error prediction relative to the RANS-SA heat flux error and the maximum pressure error predicted by the two lower fidelity models.

The RANS-SST pressure error surface (Figure 6-12) shows similar behavior to the corresponding RANS-SA error surface, but with higher errors. The RANS-SST heat flux error surface once again shows a clear trend vs angle of attack, with little variation in the Re-direction for a given angle-of-attack-value. The minimum error predicted is significantly higher than zero for this surface (Figure 6-13c).

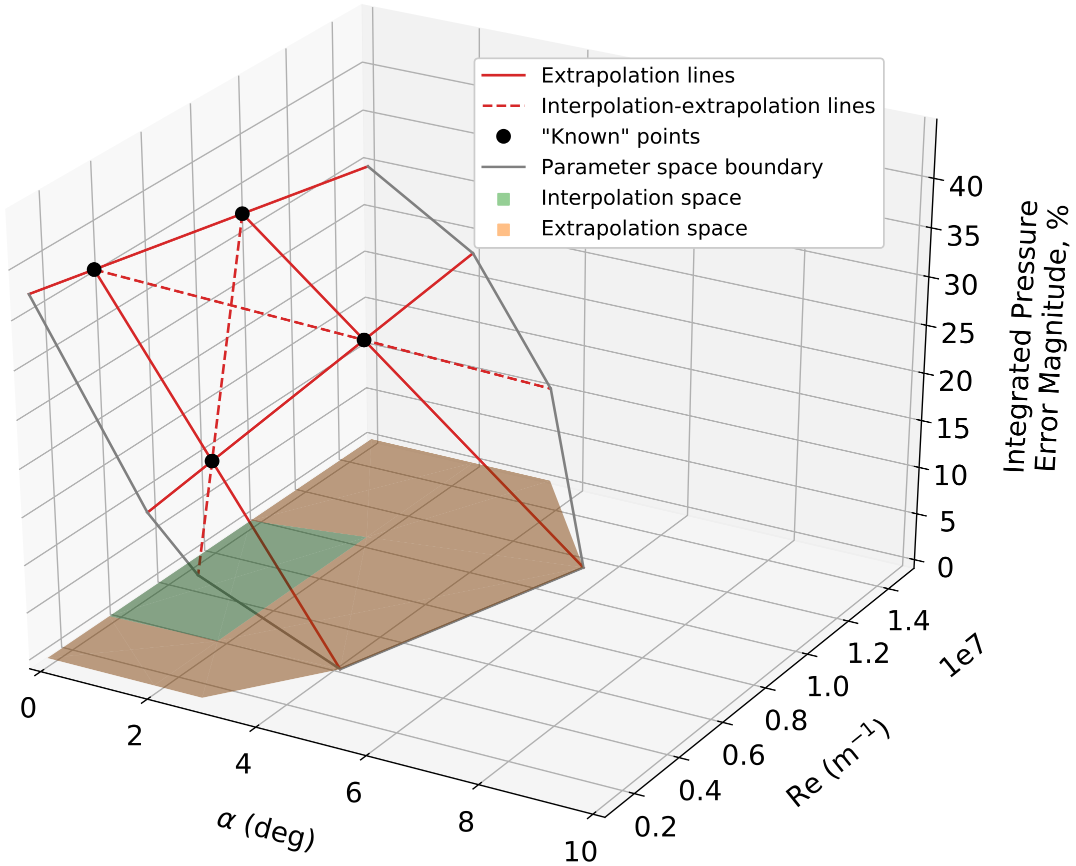

**Figure 6-5.** Validation error extrapolation surface elements.

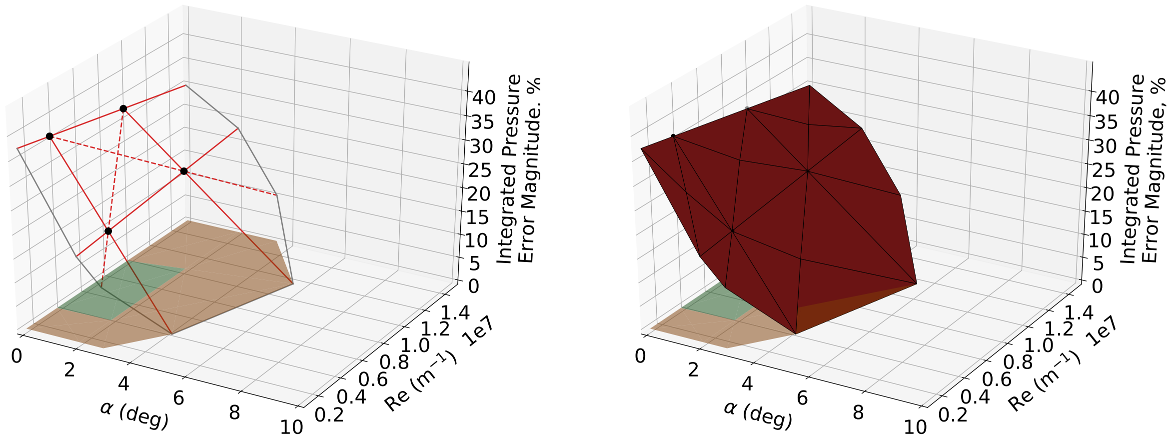

**(a)** Lines corresponding to error surface.

**(b)** Error surface, isometric view.

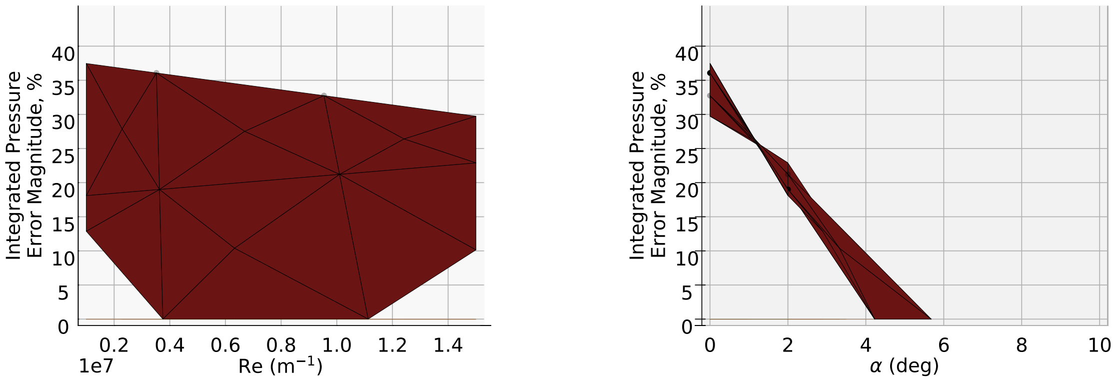

**(c)** Error surface, Re-error plane.

**(d)** Error surface, $\alpha$-error plane.

**Figure 6-6.** Validation error extrapolation surface for pressure prediction from MNA+FPBL model.

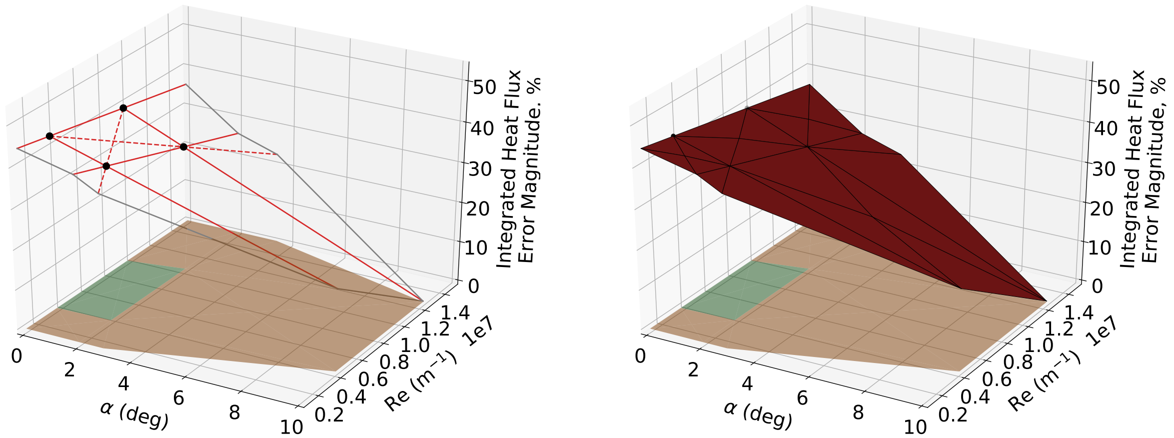

**(a)** Lines corresponding to error surface.

**(b)** Error surface, isometric view.

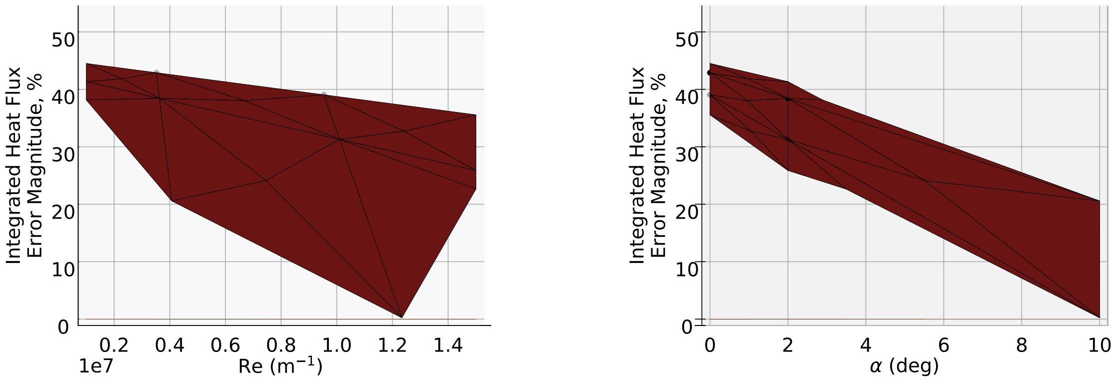

**(c)** Error surface, Re-error plane.

**(d)** Error surface, $\alpha$-error plane.

**Figure 6-7.** Validation error extrapolation surface for heat flux prediction from MNA+FPBL model.

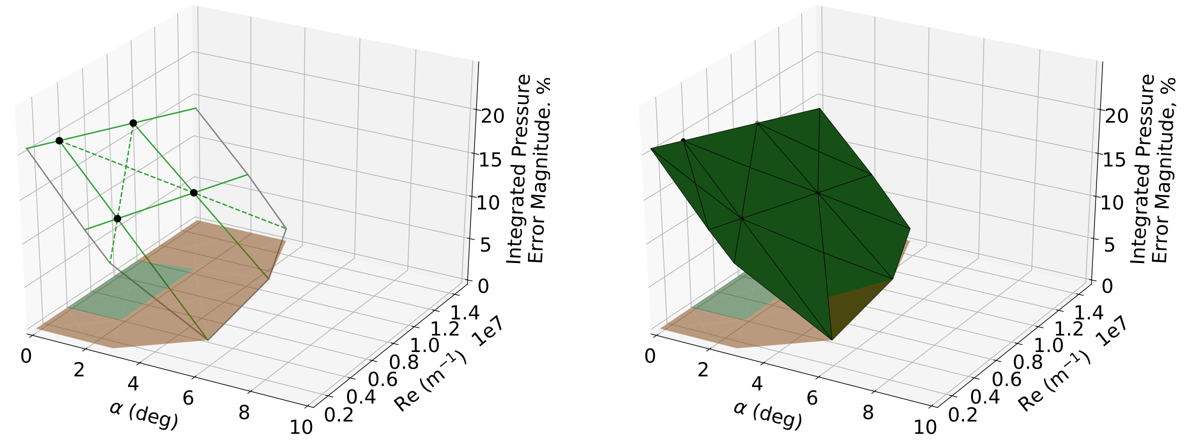

**(a)** Lines corresponding to error surface.

**(b)** Error surface, isometric view.

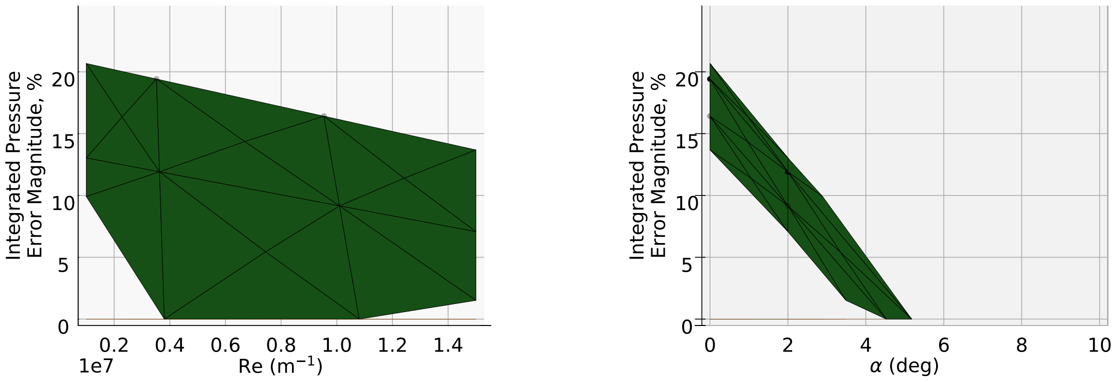

**(c)** Error surface, Re-error plane.

**(d)** Error surface, $\alpha$-error plane.

**Figure 6-8.** Validation error extrapolation surface for pressure prediction from Euler+MEIT model.

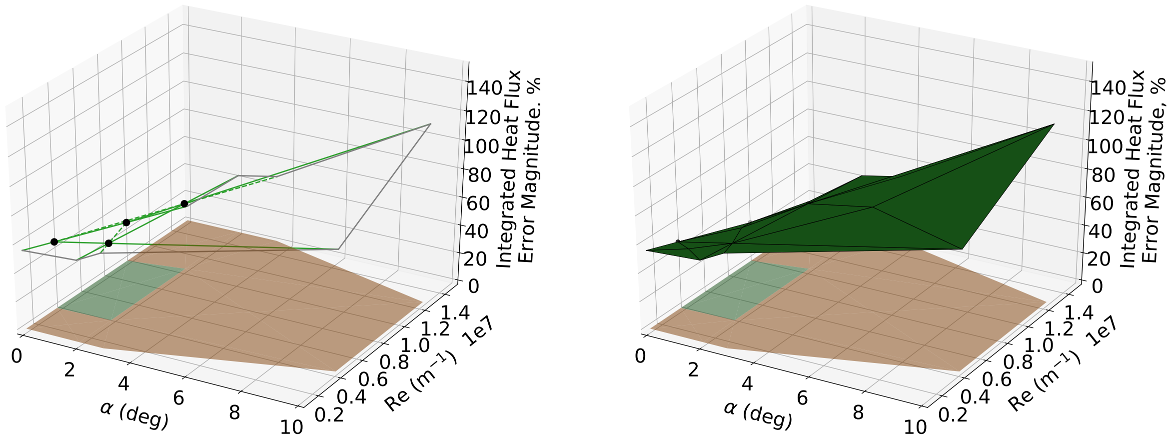

**(a)** Lines corresponding to error surface.

**(b)** Error surface, isometric view.

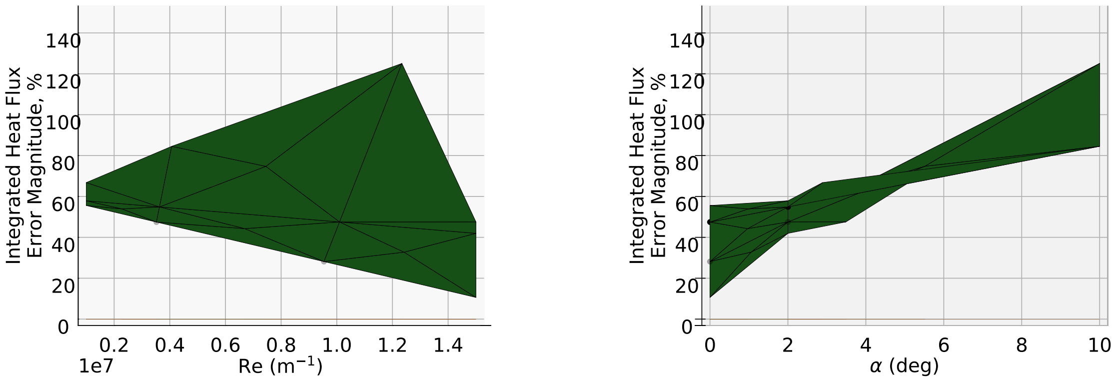

**(c)** Error surface, Re-error plane.

**(d)** Error surface, $\alpha$-error plane.

**Figure 6-9.** Validation error extrapolation surface for heat flux prediction from Euler+MEIT model.

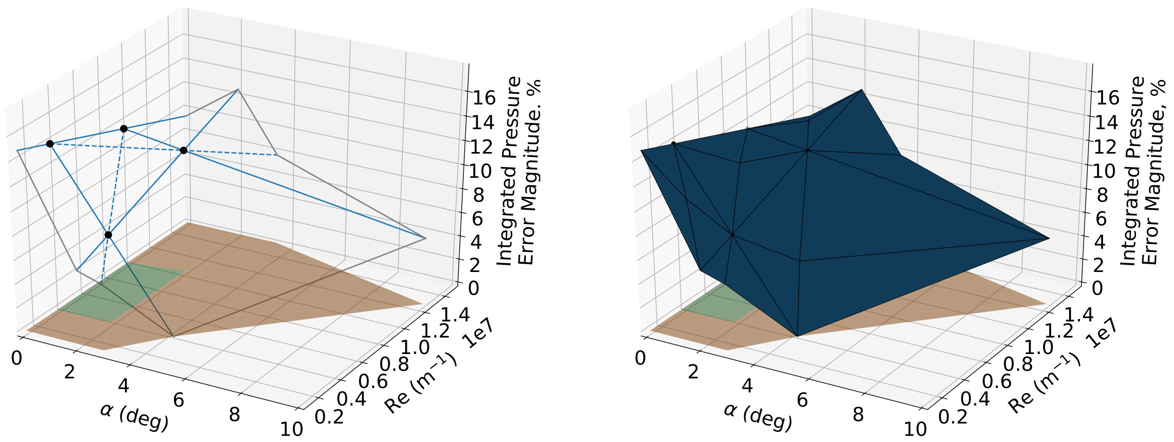

**(a)** Lines corresponding to error surface.

**(b)** Error surface, isometric view.

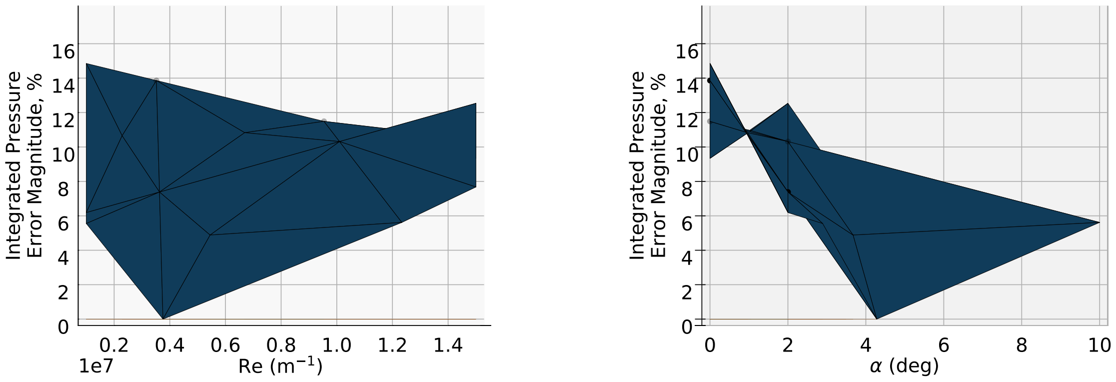

**(c)** Error surface, Re-error plane.

**(d)** Error surface, $\alpha$-error plane.

**Figure 6-10.** Validation error extrapolation surface for pressure prediction from RANS-SA model.

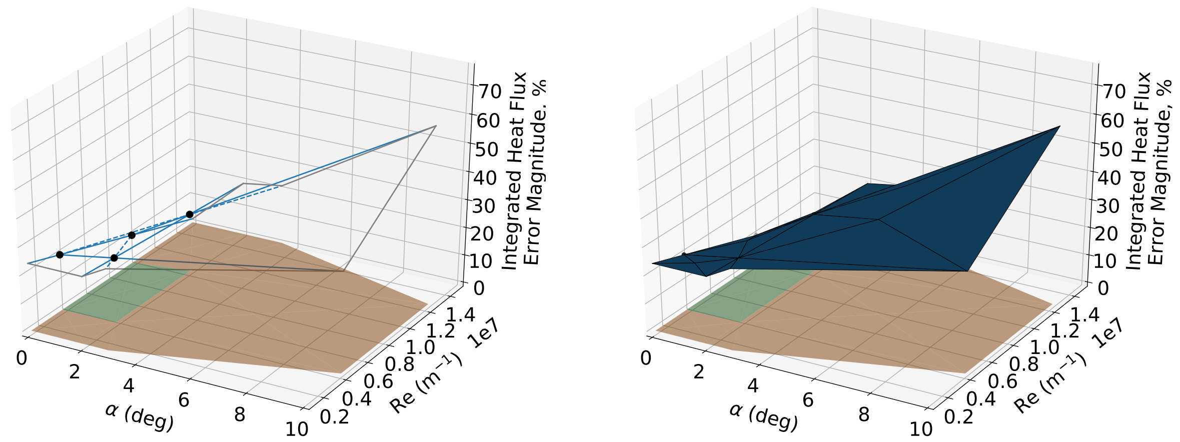

**(a)** Lines corresponding to error surface.

**(b)** Error surface, isometric view.

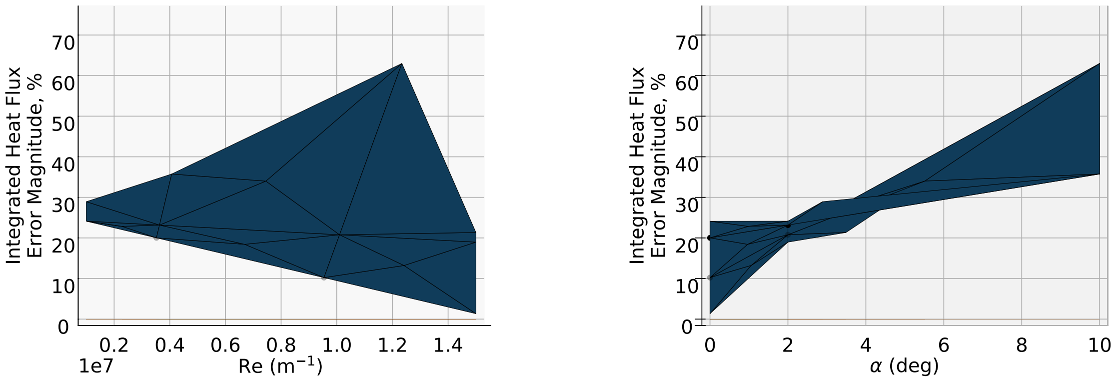

**(c)** Error surface, Re-error plane.

**(d)** Error surface, $\alpha$-error plane.

**Figure 6-11.** Validation error extrapolation surface for heat flux prediction from RANS-SA model.

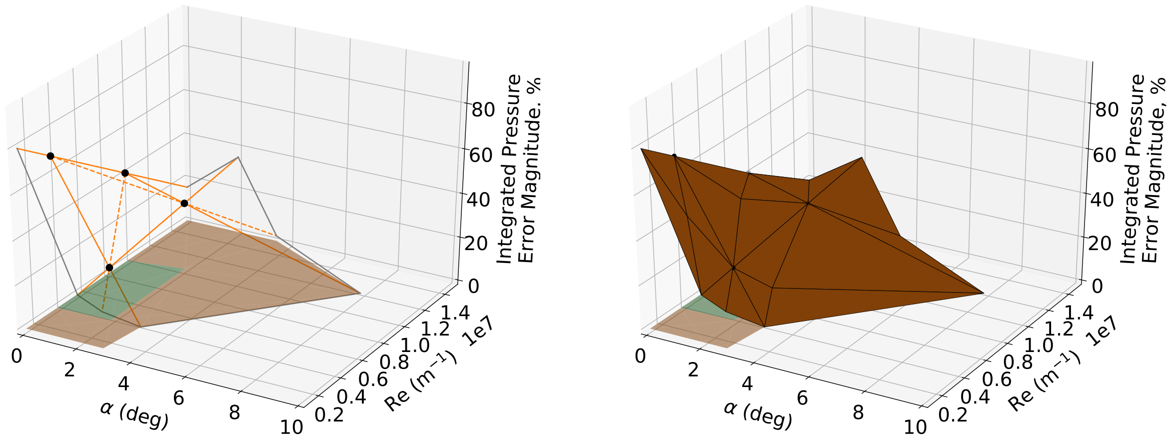

**(a)** Lines corresponding to error surface.

**(b)** Error surface, isometric view.

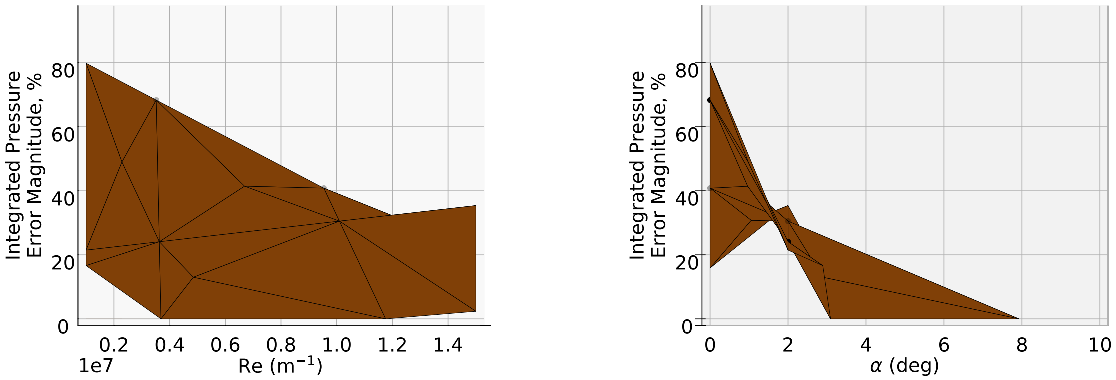

**(c)** Error surface, Re-error plane.

**(d)** Error surface, $\alpha$-error plane.

**Figure 6-12.** Validation error extrapolation surface for pressure prediction from RANS-SST model.

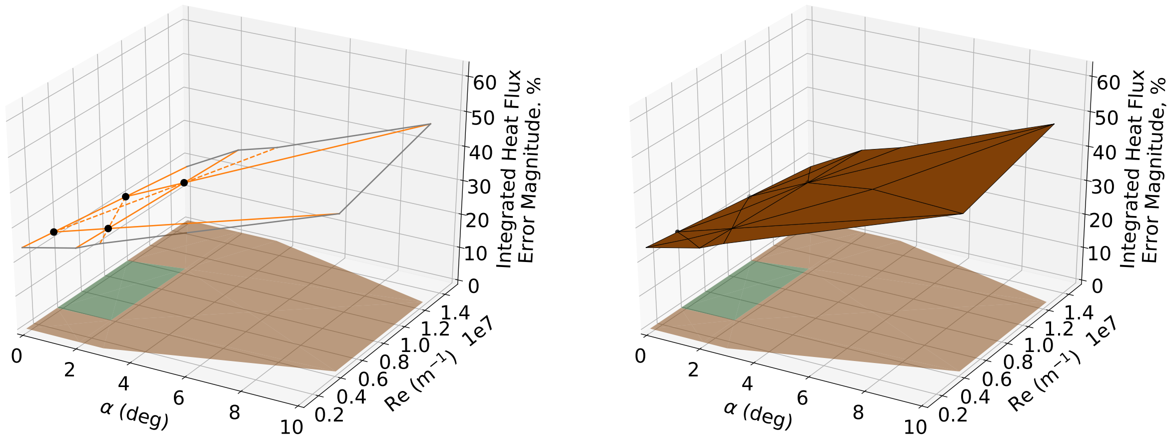

**(a)** Lines corresponding to error surface.

**(b)** Error surface, isometric view.

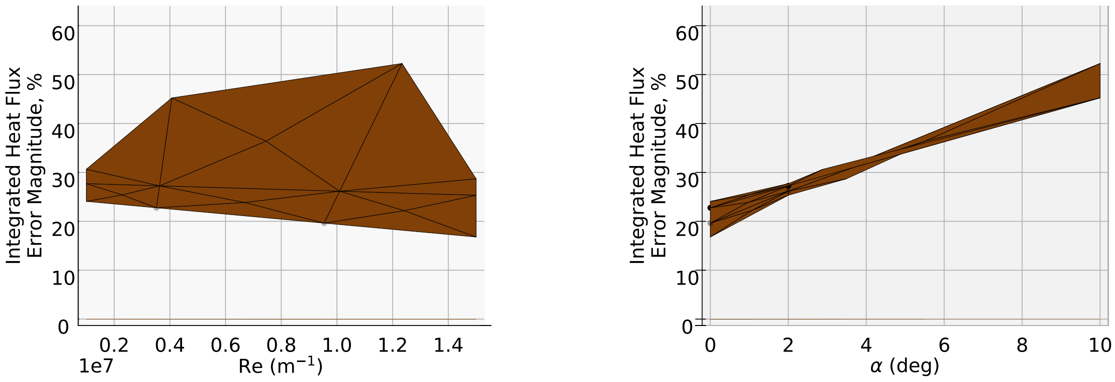

**(c)** Error surface, Re-error plane.

**(d)** Error surface, $\alpha$-error plane.

**Figure 6-13.** Validation error extrapolation surface for heat flux prediction from RANS-SST model.

## 6.4. Conclusions

Validation of simulation results is an important credibility activity, helping to increase confidence in those results. When computational simulation is performed in the absence of experimental data, validation cannot be directly performed on the simulation results. In such situations, validation error extrapolation from conditions at which experimental data is available may be the best option to obtain a reasonable validation error estimate. In this section, a simple linear extrapolation method is used in a two-dimensional (one-parameter) sense and a three-dimensional (two-parameter) sense. The resulting line and surface plots yield predictions of overall integrated relative error in QoIs at given points in the parameter space. Uncertainty should, in general be included, as in the two-dimensional plots, and can allow for higher confidence on the estimate. This exercise shows one way to obtain validation error estimates by extrapolation, but improvements/changes could be made. Extrapolation with more points could be useful in making validation error extrapolation more robust. This is especially true for extrapolation predictions which involve a high error slope and those which extrapolate a large distance into the parameter space. There are also other methods which have been examined for error extrapolation, and an analysis of multiple methods would likely be worthwhile.

# 7. TIMING STUDY

## 7.1. Importance of Cost and Accuracy in MFTK

The Multi-fidelity Toolkit, MFTK, has, at its core, competing values of computational cost and simulation accuracy [2]. The toolkit comprises the inexpensive, low-fidelity MNA+FPBL model, the more expensive mid-fidelity Euler+MEIT model, and the high-fidelity RANS models, which are generally the most expensive. Because trajectory generation for hypersonic vehicles requires an accurate assessment of aerodynamic performance and thermomechanical response, simulations are generally expensive and resulting datasets are large. However, running all simulations in a hypersonic trajectory generation study with the highest-fidelity models would require an exorbitant amount of time. Thus, the lower fidelity models play an important role in such a study by being used in lieu of the higher fidelity models when accuracy requirements allow, or in tandem with them, through the use of Hierarchical Kriging [2]. In this study, the computational cost and simulation accuracy as measured by validation comparison error are examined for the HIFiRE-1 dataset. Conclusions are made regarding the general cost and accuracy of each model for two representative runs, and the optimal number of processors to use for simulations of those runs is examined.

In this study, the same ramp-type CFL controller is used for all models and runs to provide consistency. The maximum number of iterations is set to 2,000 to avoid excessive computation times. Prior to doing this, behavior was checked on the Euler+MEIT simulation of Run 30 for consistency in the behavior of compute time versus number of processors. All simulations are also run on the same machine (Attaway) for consistency in architecture, which can affect performance. Attaway is the most recently installed institutional HPC cluster at Sandia, with good performance characteristics, and is thus optimal for use in this study. One benefit is that the results will be relevant for as long as possible.

## 7.2. Computational Cost of Each Model for Representative Cases

Using the mid-refinement mesh level (2L) for each model except Euler+MEIT, Run 30 and Run 34 are simulated using each model in MFTK. The number of cells per core is kept at roughly 30,000 with the exception of the MNA+FPBL runs, which can only use a single processor, and the RANS simulations of Run 30, which use closer to 22,000 cells per core. The mesh refinement level used for Euler+MEIT is the coarsest (3L), due to the fact that Euler+MEIT simulations are rarely run on grids which are as refined as RANS grids, and the 3L grid is thus more representative of a typical grid for these runs. The results are shown in Figure 7-1. The compute time for both runs is similar, while the computational cost as measured by time multiplied by the number of cores used is significantly higher for Run 34. This is due to the 3D meshes used for this non-axisymmetric run, which has many more cells than the corresponding 2D meshes for Run 30. Measured by either criteria, computational cost is higher for the higher fidelity models, with RANS-SST being the most expensive due to the fact that it is a two-equation model versus RANS-SA which is a one-equation model. More specifically, the RANS-SST model solves two transport equations, one for kinetic energy, and the other for the specific dissipation rate [16]. The RANS-SA model, on the other hand, solves a single transport equation for a variable related to turbulent eddy viscosity [17]. The additional transport equation increases solution time for the SST model significantly. Note that the RANS simulations took hundreds of minutes (upwards of 1 hr), which becomes extremely expensive for trajectory simulations, when dozens or hundreds of simulation times are required. The Euler+MEIT model is significantly less expensive than the RANS models, but it should be noted that appropriate mesh refinement plays an important role in this. The MNA+FPBL model is extremely inexpensive to run.

## 7.3. Cost versus Error

While the relative cost of each model from the simulations described above was expected, it is useful to examine whether simply decreasing model fidelity to achieve less expensive simulations is the best way to proceed in a given study. Similarly, if higher accuracy is needed, it is useful to examine whether simply increasing model fidelity will always improve accuracy, and if so, by how much. While these questions were answered to some extent by Chapter 5, they are further examined here, in the context of the two runs described above. To examine computational cost versus error, the simulation time is plotted versus the relative error, integrated over the axial coordinate and averaged over meridional angles for each run. Using time instead of time multiplied by number of cores is acceptable in this case because both measures showed similar trends (Figure 7-1). The resulting plots are shown in Figure 7-2. RANS-SA has the lowest or second-lowest error on both QoIs for both runs. However it does have the second-highest compute time for all run/QoI combinations. For these simulations, then, it can be concluded that when accuracy is a priority, RANS-SA is the best model choice. RANS-SST is surprisingly undesirable, having generally high simulation times and the worst error of all models for surface pressure. If simulation time is the priority, MNA+FPBL involves the shortest compute times, but has significant error for both QoIs and runs. Euler+MEIT has relatively low compute times, and has low error for surface pressure, but the highest or second-highest error for surface heat flux. Thus, which lower-fidelity model is chosen when time is a priority depends on the time constraints. Realistically, it also depends on the physical scenario being simulated, and the QoIs.

The same analysis is also performed for total integrated relative error, on the turbulent cone section of the vehicle. Similar to the corresponding section in the validation discussion, the errors on this section of the vehicle are examined separately because of the high relevance of conical geometry to hypersonic applications. The resulting plots are shown in Figure 7-3. For Run 34, these errors take into account all three unique meridional angles, when data are available, whereas for Run 30, with axisymmetric flow, the errors correspond to those computed at the 0° meridional angle. Generally, lower relative surface pressure errors are seen on the turbulent cone than for the entire vehicle. The RANS-SST model also appears to perform better on the turbulent cone than it does

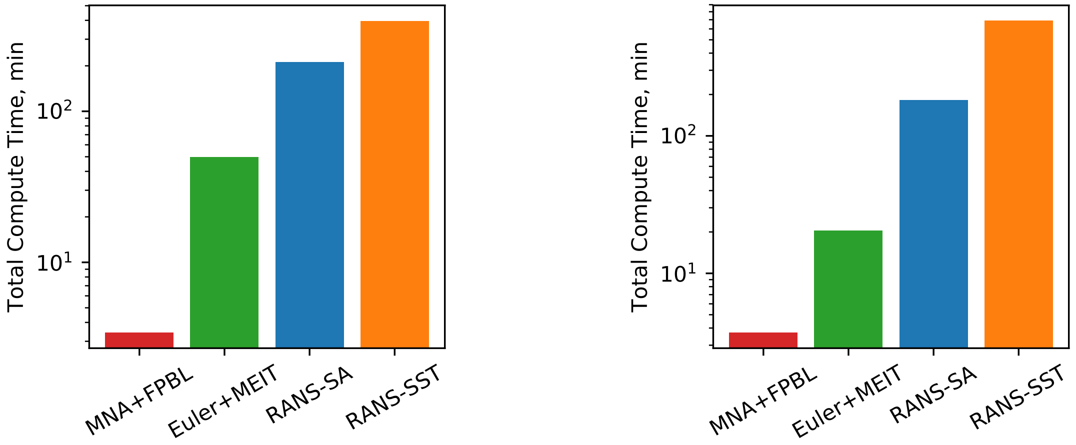

**(a)** Simulation time versus model, Run 30 **(b)** Simulation time versus model, Run 34

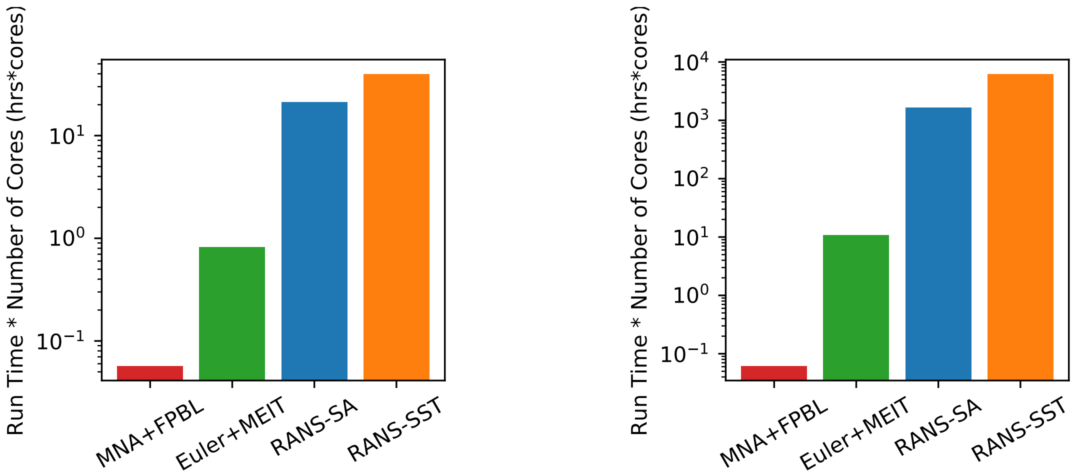

**(c)** Simulation cost versus model, Run 30 **(d)** Simulation time versus model, Run 34

**Figure 7-1.** Time and composite cost of representative simulations of Runs 30 and 34 for each MFTK model.

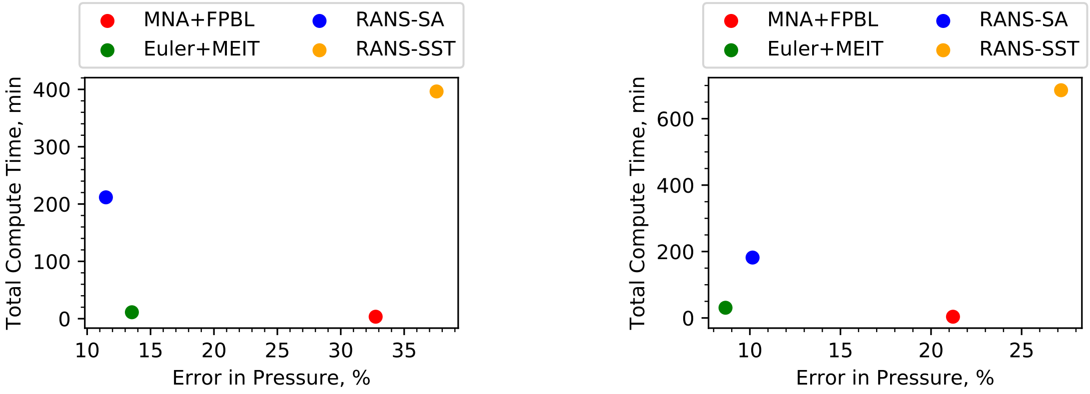

**(a)** Relative surface pressure error, Run 30

**(b)** Relative surface pressure error, Run 34

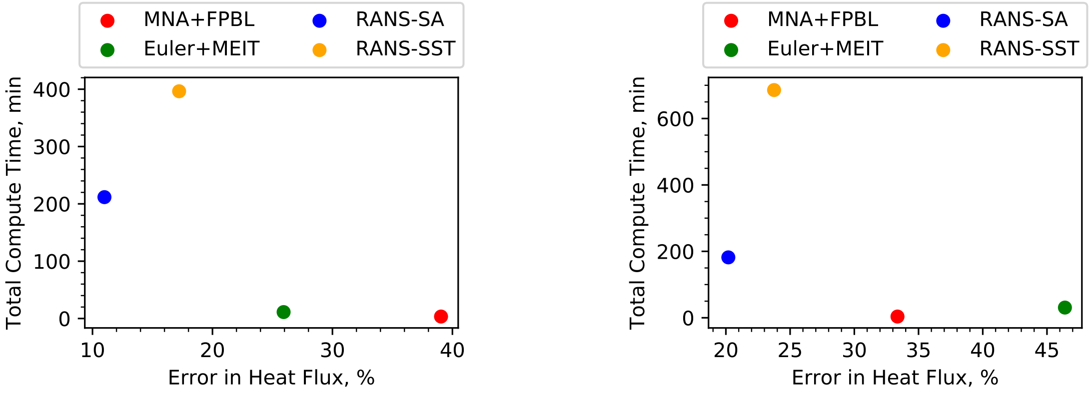

**(c)** Relative surface heat flux error, Run 30

**(d)** Relative surface heat flux error, Run 34

**Figure 7-2.** Simulation time versus overall error in surface pressure and heat flux.

overall. For Run 34, Euler+MEIT still stands out as a good choice. For surface heat flux, relative errors appear generally larger on the turbulent cone than overall. The plots appear more similar to the overall plots than the pressure plots do. RANS-SST has comparable relative error to RANS-SA for Run 30, but error which is nearly as high as that of MNA+FPBL for Run 34. Overall, the results indicate that RANS-SA appears to be the best choice, especially if accuracy is valued, and the lower fidelity models stand out in particular instances. Conclusions should be taken with some caution, as the number of sensors on this section was not high, especially for nonzero meridional angles.

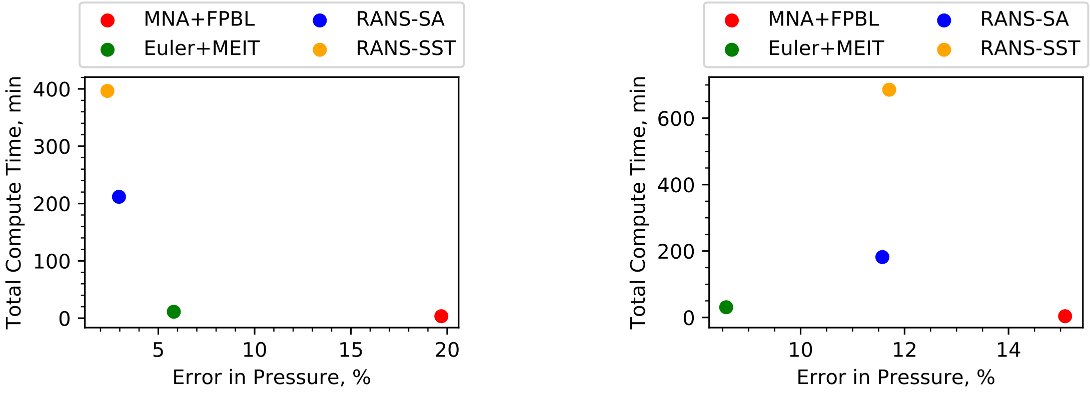

**(a)** Relative surface pressure error, Run 30

**(b)** Relative surface pressure error, Run 34

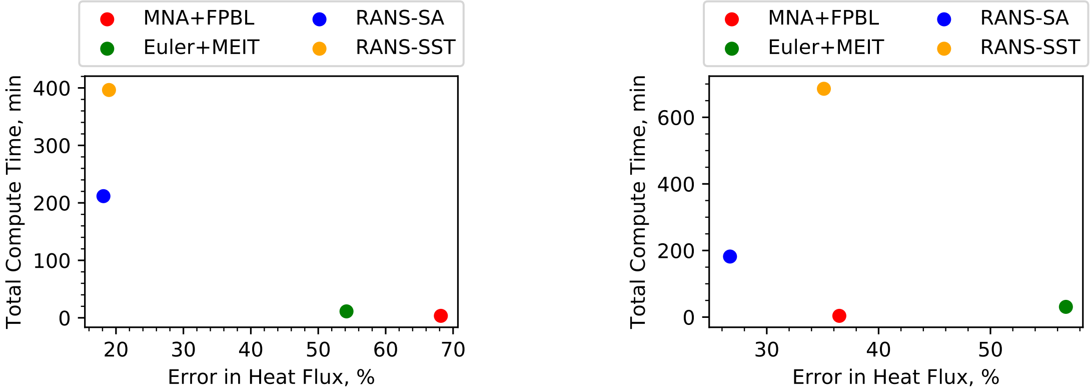

**(c)** Relative surface heat flux error, Run 30

**(d)** Relative surface heat flux error, Run 34

**Figure 7-3.** Simulation time versus overall error in surface pressure and heat flux, on turbulent cone.

## 7.4. Optimizing Number of Compute Cores

The number of compute cores used to perform a simulation is important for multiple reasons. Using more cores generally reduces simulation time, and is thus often desirable. However, using too many cores can cause mesh over-decomposition issues and long queue times in a high performance computing system. When the number of cores specified becomes too high, simulations times can pass an optimal point, or the simulations can fail. To address this issue, compute time is plotted versus the number of processors for the Euler+MEIT and both RANS models. The MNA+FPBL model is not studied, because it can only use a single core. The results are shown in Figures 7-4–7-6. For the Euler+MEIT (Fig. 7-4) simulation of Run 30, the compute time decreases monotonically with the number of processors used. Moving from 1 processor to 8 results in a significant reduction in compute time ($\sim 6\times$). While further reductions in time are possible with more processors, using 16 provides little decrease in compute time while increasing total cost significantly and potentially nearing a number of cells per core which would cause over-decomposition. Thus, 8 processors would be a reasonable number to choose. For the Euler+MEIT simulation of Run 34, there is a clear minimum compute time at 288 processors, which corresponds to roughly 30,000 cells per core. This fits with the rule of thumb sometimes used for RANS simulations, and would be a good choice for such a simulation. Note that total cost as measured by compute time multiplied by the number of cores used is also plotted to the right of the time versus number of processors plots. These plots serve to show the competing trend of increasing cost with that of compute time.

In Figure 7-5, compute time vs number of processor plots for the RANS-SA model are shown. As with Euler+MEIT, Run 30 shows a monotonic decrease in compute time with an increasing number of processors. Using a similar argument as for Euler+MEIT, 16 processors appears to be a good choice. It provides a large speedup as compared to using 2–8 processors, but avoids the increase in cost associated with increasing the number of processors further. It also avoids over-decomposition concerns by staying at 8,000 cells per core (∼1,000 cells per core sometimes produced such errors in the validation study). To stay even further from this region, 8 processors could be chosen. The Run 34 simulation also shows a clear minimum region similar to the Euler+MEIT results, and indicates that ∼576 processors, which corresponds to ∼30,000 cells per core, is optimal.

Finally, RANS-SST results are shown in Figure 7-6. 16 processors (8,000 cells per core) appears to be a reasonable choice for Run 30. For Run 34, ∼1,150 processors (∼14,000 cells per core) or ∼2,300 (∼7,000 cells per core) would make sense. It is interesting to note that RANS-SST did not show a clear minimum time for Run 34, unlike the RANS-SA and Euler+MEIT models. This behavior could be further examined and could be tied to the form of the model.

## 7.5. Future Work

In this study, compute times for the Euler+MEIT and RANS models of MFTK are examined for two HIFiRE-1 runs on representative meshes. It is seen that compute times follow the expected trend (increase with increasing model fidelity), but that there are competing measures of simulation performance which must be taken into account. For the parameters and geometry studied, these results provide a good basis for intuition regarding the choice of model and number of processors to use in a simulation. Future work could include a study on the use of the updated CFL controller used in SPARC, which can provide significant speedups. In addition, the behavior of the RANS-SST model on simulations involving 3D meshes could be further examined.

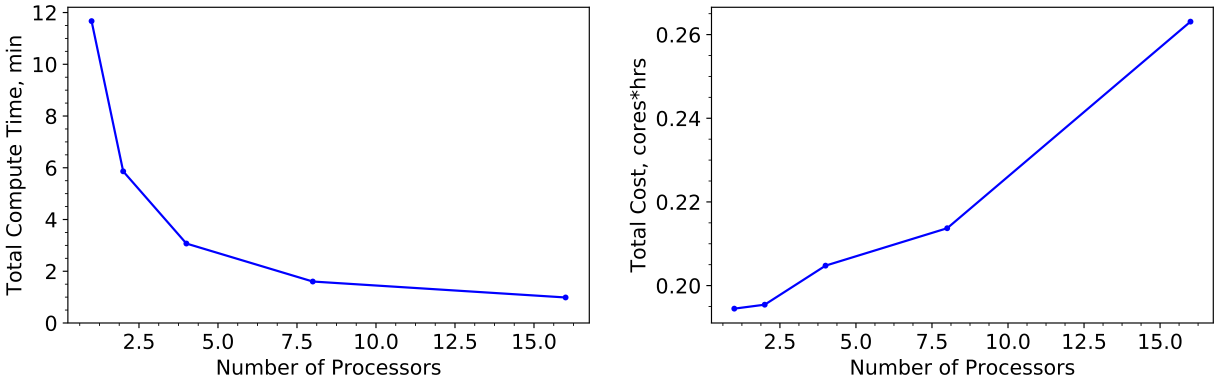

**(a)** Compute time versus number of processors, Run 30 **(b)** Simulation cost versus number of processors, Run 30

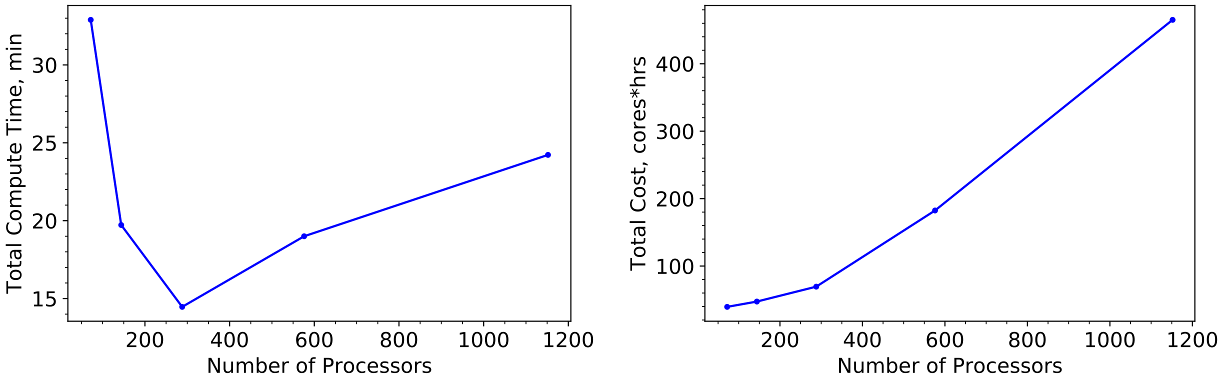

**(c)** Compute time versus number of processors, Run 34 **(d)** Simulation cost versus number of processors, Run 34

**Figure 7-4.** Simulation cost and compute times versus number of processors for Euler+MEIT model.

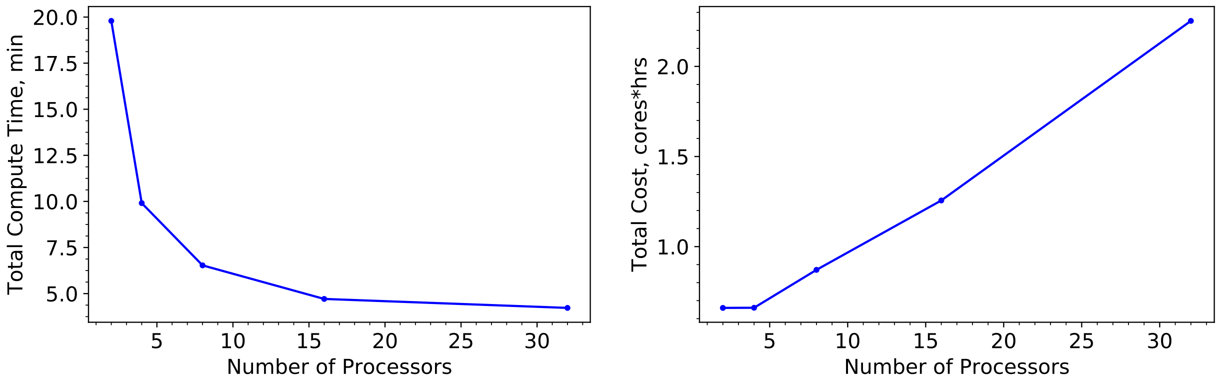

**(a)** Compute time versus number of processors, Run 30 **(b)** Simulation cost versus number of processors, Run 30

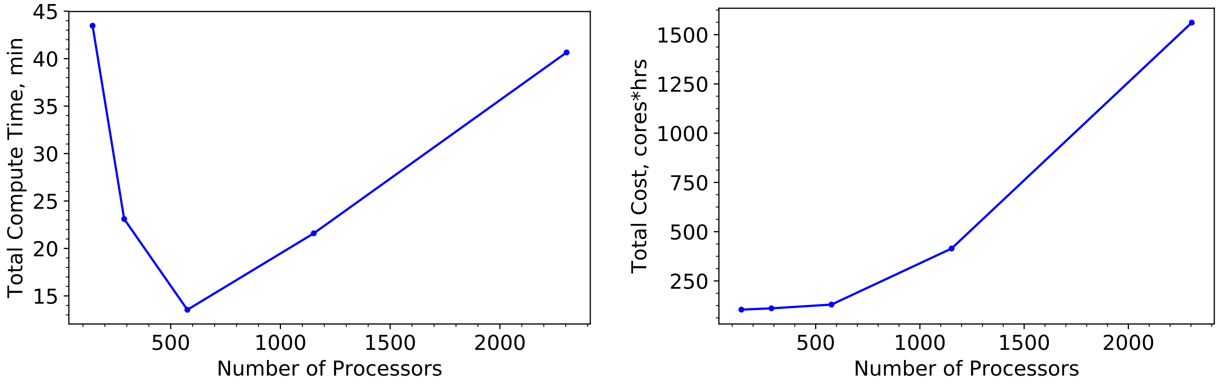

**(c)** Compute time versus number of processors, Run 34 **(d)** Simulation cost versus number of processors, Run 34

**Figure 7-5.** Simulation cost and compute times versus number of processors for RANS-SA model.

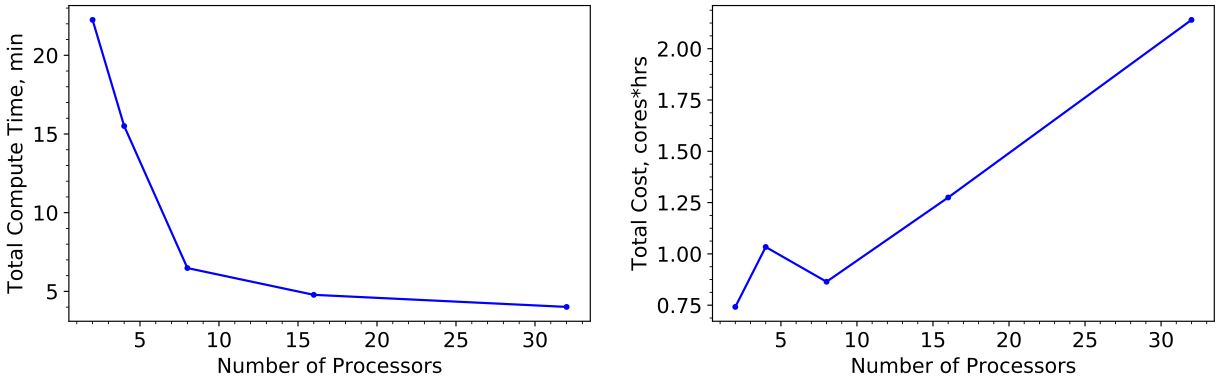

**(a)** Compute time versus number of processors, Run 30 **(b)** Simulation cost versus number of processors, Run 30

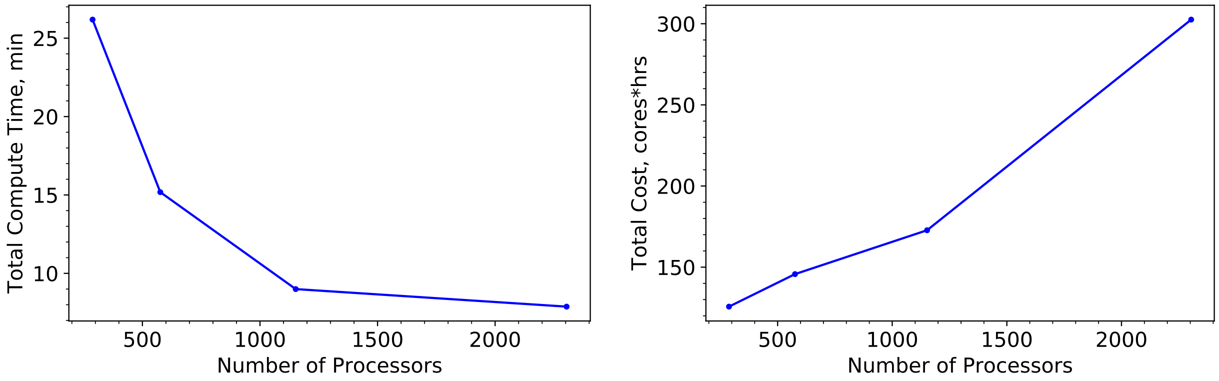

**(c)** Compute time versus number of processors, Run 34 **(d)** Simulation cost versus number of processors, Run 34

**Figure 7-6.** Simulation cost and compute times versus number of processors for RANS-SST model.

# 8. CONCLUSIONS

MFTK is a highly useful workflow for hypersonic aerothermal modeling and simulation. This study provides quantitative credibility evidence to aid analysts in understanding the accuracy and uncertainty associated with the use of MFTK in a challenging context. In this study, verification and validation activities are continued from the previous year and expanded.

For code verification, the MNA+FPBL work includes testing the viscous quantities of interest on the same two-dimensional test cases as before, but also extends to a three-dimensional problem. The SPARC MEIT mathematical model and code implementation are studied and described in a theory guide [9]. In addition, two tests have been completed on the MEIT code, with one testing the laminar flow model and the other the turbulent flow model.

The solution verification effort is expanded to cover simulations reproducing four HIFiRE-1 experimental runs. The finest mesh is taken as the nominal mesh, and the GCI is calculated using the two finest meshes (in the numerator). This results in lower numerical uncertainty in general as compared with results from the previous year. Numerical uncertainty associated with all models is relatively low over much of the vehicle. Euler+MEIT and RANS-SST models still show relatively high numerical uncertainties in challenging regions, and further investigation of this trend would be beneficial.

For validation, the study is also extended to the same four HIFiRE-1 runs as for solution verification, but additional work comparing these runs to each other is done. Detailed error trends along the vehicle, overall error, error by vehicle section, and average model error across runs are examined. Effects of parameter changes on overall simulation error are analyzed. Over much of the vehicle, the models show good accuracy, though relatively high errors are observed in several locations for multiple models. In particular, the Euler+MEIT and RANS-SST models have relatively high error in regions of complex flow. The RANS-SA model shows the lowest error in general, with the RANS-SST model being competitive on the cone for certain runs. Generally, the error and uncertainty results agree with the expected fidelity of each model. Exceptions to this trend include high error and uncertainty in the Euler+MEIT and RANS-SST results for complex flow (transition, separation, and SLBI) and competitive accuracy of the lower-fidelity models for simpler flow.

A timing study is completed which examines the computational cost of each model for representative 2D and 3D simulations. Cost versus error trends are examined in plots comparing the model fidelities in MFTK. Finally, the optimal number of processors for the Euler+MEIT and RANS models is examined.

# BIBLIOGRAPHY

[1] Lance, B. W., Krueger, A. M., Freno, B. A., and Wagnild, R. M., "Verification and Validation Activities for the Multi-Fidelity Toolkit," Sandia Report SAND2022-1479, Sandia National Laboratories, February 2022.

[2] Wagnild, R. M., Dinzl, D. J., Bopp, M. S., Dement, D. C., Robbins, B. A., Bruner, C. W. S., Grant, M. J., Murray, J., and Harper, J. M., "Development of a Multi-fidelity Toolkit for Rapid Aerothermal Model Development," Sandia Report SAND2019-13632, Sandia National Laboratories, Oct 2019.

[3] Oberkampf, W. L. and Roy, C. J., *Verification and Validation in Scientific Computing*, Cambridge University Press, 2010.

[4] AIAA, "Guide for the Verification and Validation of Computational Fluid Dynamics Simulations (AIAA G-077-1998 (2002))," 1998.

[5] ASME, "V&V 20-2009: Standard for Verification and Validation in Computational Fluid Dynamics and Heat Transfer," Tech. rep., American Society of Mechanical Engineers, 2009.

[6] Freno, B. A., Carnes, B. R., and Weirs, V. G., "Code-Verification Techniques for Hypersonic Reacting Flows in Thermochemical Nonequilibrium," *Journal of Computational Physics*, Vol. 425, 2021.

[7] Carnes, B. R., Weirs, V. G., and Smith, T., "Code Verification and Numerical Error Estimation for use in Model Validation of Laminar, Hypersonic Double-Cone Flows," *AIAA Scitech 2019 Forum*, American Institute of Aeronautics and Astronautics, 2019, p. 2175.

[8] Wadhams, T., Mundy, E., MacLean, M., and Holden, M., "Ground Test Studies of the HIFiRE-1 Transition Experiment Part 1: Experimental Results," *Journal of Spacecraft and Rockets*, Vol. 45, No. 6, 2008, pp. 1134–1148.

[9] Kirsch, J. R., Delgado, P. M., and Dechant, L. J., "Theory and Implementation Guide for Sandia National Laboratories' Momentum-Energy Integral Technique (MEIT) Boundary Layer Code," Sandia Report SAND2023-12517, Sandia National Laboratories, December 2022.

[10] MacLean, M., Wadhams, T., Holden, M., and Johnson, H., "Ground Test Studies of the HIFiRE-1 Transition Experiment Part 2: Computational Analysis," *Journal of Spacecraft and Rockets*, Vol. 45, No. 6, 2008, pp. 1149–1164.

[11] Salari, K. and Knupp, P., "Code Verification by the Method of Manufactured Solutions," Sandia Report SAND2000-1444, Sandia National Laboratories, June 2000.

[12] Polansky, G. F., "Hypersonic Integral Boundary Layer Analysis of Reentry Geometries (HIBLARG) Code Description and User's Manual Version 2.0," Sandia Report SAND89-0552, Sandia National Laboratories, March 1990.

[13] Kimmel, R. L., Adamczak, D., Paull, A., Paull, R., Shannon, J., Pietsch, R., Frost, M., and Alesi, H., "HIFiRE-1 Preliminary Aerothermodynamic Measurements," *AIAA paper*, Vol. 3413, 2011, pp. 2011.

[14] Trucano, T. G., Pilch, M., and Oberkampf, W. L., "General Concepts for Experimental Validation of ASCI Code Applications," Tech. Rep. SAND2002-0341, Sandia National Laboratories, Albuquerque, NM (US), 2002.

[15] Kieweg, S., Carnes, B., Freno, B., Phipps, E., Ridzal, D., Rider, W. J., Smith, T. M., Weirs, V. G., Dinzl, D., Howard, M., Wagnild, R., Fisher, T., Mussoni, E., Arienti, M., and Ray, J., "ASC ATDM FY18 Level 2 Milestone Report: Validation of Hypersonic Turbulence Physics in SPARC (Official Use Only-Export Controlled Information)," Tech. Rep. SAND2018-10261, Sandia National Laboratories, 2018.

[16] Menter, F. R., "Two-Equation Eddy-Viscosity Turbulence Models for Engineering Applications," *AIAA Journal*, Vol. 32, No. 8, 1994, pp. 1598–1605.

[17] Spalart, P. R. and Allmaras, S. R., "A One-Equation Turbulence Model for Aerodynamic Flows," *Recherche Aerospatiale*, , No. 1, 1994, pp. 5–21.

# DISTRIBUTION

## Email—Internal

| Name | Org. | Sandia Email Address |
|---|---|---|
| Gregory Weirs | 1446 | vgweirs@sandia.gov |
| Jeffrey Payne | 1510 | jlpayne@sandia.gov |
| Matthew Barone | 1515 | mbarone@sandia.gov |
| Paul Delgado | 1515 | pmdelga@sandia.gov |
| Derek Dinzl | 1515 | djdinzl@sandia.gov |
| Nathan Miller | 1515 | nmille1@sandia.gov |
| Bryan Morreale | 1515 | bjmorre@sandia.gov |
| Eric Robertson | 1515 | edrobe@sandia.gov |
| Justin Smith | 1515 | jussmit@sandia.gov |
| Ross Wagnild | 1515 | rmwagni@sandia.gov |
| Matthew Bopp | 1541 | msbopp@sandia.gov |
| Paul Crozier | 1541 | pscrozi@sandia.gov |
| Travis Fisher | 1541 | tcfishe@sandia.gov |
| Lauren Beghini | 1544 | llbeghi@sandia.gov |
| Brian Carnes | 1544 | bcarnes@sandia.gov |
| Kevin Dowding | 1544 | kjdowdi@sandia.gov |
| Brian Freno | 1544 | bafreno@sandia.gov |
| Sarah Kieweg | 1544 | skieweg@sandia.gov |
| Jared Kirsch | 1544 | jkirsch@sandia.gov |
| Aaron Krueger | 1544 | amkrueg@sandia.gov |
| Blake Lance | 1544 | blance@sandia.gov |
| William Rider | 1544 | wjrider@sandia.gov |
| Justin Winokur | 1544 | jgwinok@sandia.gov |
| Jonathan Murray | 5422 | jmurray@sandia.gov |
| Chisom Wilson | 5913 | cswilso@sandia.gov |
| Leah Tuttle | 5914 | lworrel@sandia.gov |
| Technical Library | 1911 | sanddocs@sandia.gov |

Sandia National Laboratories is a multimission laboratory managed and operated by National Technology & Engineering Solutions of Sandia LLC, a wholly owned subsidiary of Honeywell International Inc., for the U.S. Department of Energy's National Nuclear Security Administration under contract DE-NA0003525.